UNIVERSITÀ DEGLI STUDI DI ROMA "TOR VERGATA"

FACOLTA' DI INGEGNERIA

DOTTORATO DI RICERCA IN

GEOINFORMAZIONE

CICLO DEL CORSO DI DOTTORATO
XX

Titolo della tesi

Estimation of the velocity vector of moving targets from SAR images

Nome e Cognome del dottorando

Andrea Radius

Docente Guida/Tutor: Prof. Domenico Solimini

Coordinatore: Prof. Domenico Solimini

RIASSUNTO

Il SAR (Synthetic Aperture Radar) è un tipo di radar che acquisisce immagini per sintesi con alta risoluzione e indipendentemente dalle condizioni meteorologiche e di luminosità; per queste ragioni il SAR ricopre un ruolo fondamentale nel telerilevamento quando sono richieste alta risoluzione spaziale e continuità temporale.

Nel passato il SAR è stato utilizzato soprattutto per analizzare le caratteristiche del suolo terrestre, sfruttando l'interazione tra onde elettromagnetiche nella banda delle microonde e superficie terrestre. Rapidamente le capacità intrinseche di questo strumento di analizzare le caratteristiche dinamiche degli oggetti osservati hanno reso il SAR particolarmente adatto al monitoraggio di oggetti in movimento in contesti commerciali, strategici e di sorveglianza. Lo sviluppo di SAR multi-canale ne è la dimostrazione più evidente, consentendo lo sviluppo di tecniche sempre più sofisticate per la stima dei parametri di moto degli oggetti.

Questa tesi si inserisce in questo contesto, presentando un'analisi degli effetti del moto in immagini SAR e proponendo due metodologie per stimare il vettore velocità di oggetti in movimento. Il primo metodo consente di ottenere le informazioni sul moto da dati grezzi di un sistema SAR a due canali sfruttando tutto il contenuto informativo dei dati in ampiezza e fase, derivando le componenti di velocità dalla ricostruzione della funzione di fase relativa agli oggetti in movimento, dovuta alla variazione della distanza tra radar e superficie osservata all'interno dell'apertura sintetica; la seconda metodologia deriva i parametri di moto delle navi sfruttando esclusivamente l'informazione di ampiezza.

E' importante ricordare che gli algoritmi sviluppati operano senza la necessità di informazioni *a priori*.

ABSTRACT

The SAR (Synthetic Aperture Radar) is a radar which acquires synthesized images with high resolution independently from the weather conditions; for these reasons the SAR plays an important role in remote sensing, when high resolution and temporal continuity are required.

In the past, SAR systems main goals were the study of the interaction between electromagnetic waves and the Earth surface. Quickly the intrinsic capability of this instrument to analyze the dynamic characteristics of the observed objects and the changes of the requirements of the users made the SAR particularly fit for moving target detection in commercial, surveillance and strategic context.

The development of recent multi-channel SAR systems enables the development of sophisticated techniques for the surveillance of moving objects, making this field very active research area. .

This thesis addresses this particular problem by presenting an analysis of the effects of the moving targets in SAR images and by proposing two methodologies to estimate the velocity vector of objects in motion. The first methodology extracts the motion information from dual-channel SAR raw data using all the informative content of the data in amplitude and phase. It retrieves the velocity components by the reconstruction of the phase function of moving targets, due to the variability of the distance between radar and observed surface inside the synthetic aperture. The second methodology extracts the motion parameters of the ships in the sea environment using only the amplitude information. It is important note that the proposed algorithms work without *a priori* information.

The developed schemes, when compared with these proposed in recent literature, give encouraging results using a mixture of real and synthetic data.

RINGRAZIAMENTI

Sento profondamente il dovere e il piacere di ringraziare coloro che mi hanno sostenuto nel concludere questo periodo di specializzazione, necessario a proiettarmi nel mondo del lavoro.

Ringrazio innanzitutto il mio tutor Prof. Domenico Solimini, che mi ha indirizzato e sostenuto in questi anni, dandomi la possibilità di specializzarmi in un settore così elitario e di grande interesse.

Ringrazio inoltre:

- Paulo, per il suo prezioso aiuto e per l'attenzione che mi ha dedicato nel periodo in cui sono stato a Lisbona;
- Johnny, per avermi dato consigli utilissimi durante questo periodo;
- Tutti i miei amici che mi hanno sostenuto in questi anni.

Un ringraziamento particolare va ai miei genitori e a tutta la mia famiglia, che mi è stata di supporto in ogni momento; e a Carol che mi è stata così vicina e che mi ha dato una forza grandissima per affrontare tutte le difficoltà, e che ha reso la mia vita completa e pienamente equilibrata.

CONTENTS

MATHEMATICAL SYMBOLS

a_{az}	Azimuth acceleration of a moving target
a_{rg}	Ground range acceleration of the moving target
B	Transmitted signal band
B_{ATI}	Spatial baseline of the two antennas in along track mode
B_D	Processed Doppler bandwidth
B_{Di}	Processed Doppler bandwidth of the i^{th} sub-aperture
c	Light velocity
f_c	Carrier frequency of the transmitted signal
f_{Dc}	Doppler Centroid
f_{Dci}	Doppler centroid of the i^{th} look
f_R	Doppler Rate
f_s	Sampling frequency of the received signal
$\hat{g}$	Range compressed data
h	Impulse Response Function (IRF) of the SAR response
h^{-1}	Reference signal for SAR compression
h_{az}^{-1}	Azimuth reference signal
H	Satellite altitude
K	Chirp slope
L_a	Physical length of the antenna
N_{chirp}	Range samples number for a pointform scatterer
N_{sa}	Azimuth sample number of the synthetic aperture
PRF	Pulse repetition frequency
PRT	Pulse repetition time
R	Radial distance between antenna and observed object (slant range)
R_c	Slant range at the center of synthetic aperture
R_{ci}	Slant range at the center of the i^{th} sub-aperture
R_{mov}	Slant range of the moving target
R_0	Slant range at the zero Doppler

$\underline{R}_{sat}$	Satellite position vector
$\underline{R}_{\mathrm{target}}$	Target position vector
s	Azimuth time (slow time) at Doppler centroid
s_c	Azimuth time at the center of the synthetic aperture (phase center)
s_{ci}	Azimuth time at the center of the i^{th} sub-aperture (look phase center)
s_0	Azimuth time at the zero Doppler
S	Integration time
S_i	Integration time of the i^{th} sub-aperture
t	Range time (fast time)
v_{az}	Azimuth velocity of a moving target
v_B	Beam velocity on ground
v_r	Received voltage phasor from the SAR
$\hat{v}_r$	Base-band signal of the received data
v_{rg}	Ground range velocity of the moving target
v_{sr}	Slant range velocity of the moving target
V_R	Radial velocity
V_{sat}	Satellite velocity
V_{st}	Relative velocity between satellite and target
W_a	Azimuth antenna pattern
Δsr	Slant range resolution
Δaz	Azimuth resolution
ζ	Backscattering amplitude function
η	Azimuth time at zero Doppler
η_{ap}	Fraction global aperture used to synthesize the looks
η_{shift}	Azimuth temporal shift of the moving target
ϑ	Local elevation angle
θ_{az}	Width to -3dB of the azimuth antenna pattern
λ	Wavelenght of the transmitted signal
τ	Trasmitted pulse time
Φ	Two-way received signal phase

INTRODUCTION

The SAR (Synthetic Aperture Radar) was developed in the ’50 years after the observation of Carl Wiley (Goodyear Aircraft Corporation). He noted that a Doppler spectrum processing of the received signal from a coherent radar system can achieve a high spatial resolution along the motion direction.

The capability of the SAR to produce high resolution images for a continuative and global monitoring attracted the interest of the scientific community, particularly with the advent of the satellites.

In 1978 the first SAR system on board of satellite platform was launched (SEASAT). Afterwards a lot of spatial SAR mission were launched. In the ´90 years there was a big development in this sector, with the planning of numerous SAR mission for civil and military applications.

The launched satellites until now were in 1991 ERS-1 (ESA, European Spatial Agency), in 1992 JERS-1 (NASDA, National Space Development Agency of Japan), in 1995 ERS-2 (ESA) and RADARSAT-1 (CSA, Canadian Space Agency), in 2002 Envisat (ESA), in 2006 ALOS (NASDA), and finally in 2007 the TerraSAR-X (DLR, Deutschen Zentrum für Luft- und Raumfahrt and EADS Astrium), two satellites of Cosmo Skymed (ASI and Alenia Space) and RADARSAT-2.

Particularly, 2007 was an exceptional year; never so many SAR satellites were launched in a so short time. Particularly, these satellites are dedicated to monitoring of moving targets. In fact, the intrinsic capability of this instrument to analyze the dynamic characteristics of the observed objects and the changes of the requirements of the users made the SAR particularly fit for moving target detection in commercial, surveillance and strategic context.

So, in recent years many efforts have been devoted to enhancing the content and quality of space borne SAR products and several methods of data processing have been developed and implemented for monitoring of moving targets on the surface.

This work’s main topic is moving target processing. The thesis is organized as follows.

Chapter 1 introduces the theory of SAR processing and illustrates the effects of the moving target on the focused image, with particular attention to the mathematical and graphical point of view.

Chapter 2 illustrates the SAR simulator that was developed for generating simulated raw data of moving targets on a static background: the simulated data is used to validate the velocity estimation algorithm, presented in chapter 3, which is tested for the data of a two channel SAR system.

Chapter 4 proposes a sub-aperture processing technique and analyzes the information about the radial velocity of a target obtained from two channel synthesized by splitting the synthetic aperture of a single channel SAR.

Chapter 5 proposes the second velocity estimation algorithm developed, that works on amplitude data.

CHAPTER 1
SAR PROCESSING AND EFFECTS OF MOVING TARGET

1.1. INTRODUCTION

This chapter introduces the SAR processing from the raw data received by the antenna to the backscattering value in Strip-Map SAR configuration, obtained after a complex processing chain.

The content is important for understanding of the SAR processor working and of the role of the Doppler parameters for estimating the velocity of a target.

The final section explicates the effects of a moving target on a SAR scene, showing the changes introduced on the phase.

1.2 THE STRIP-MAP SAR

The SAR acquisition geometry is shown in fig.1.1, where $\underline{R}_{sat}$, $\underline{R}_{\text{target}}$ and V_{sat} are respectively the satellite position, the satellite velocity and the observed surface position.

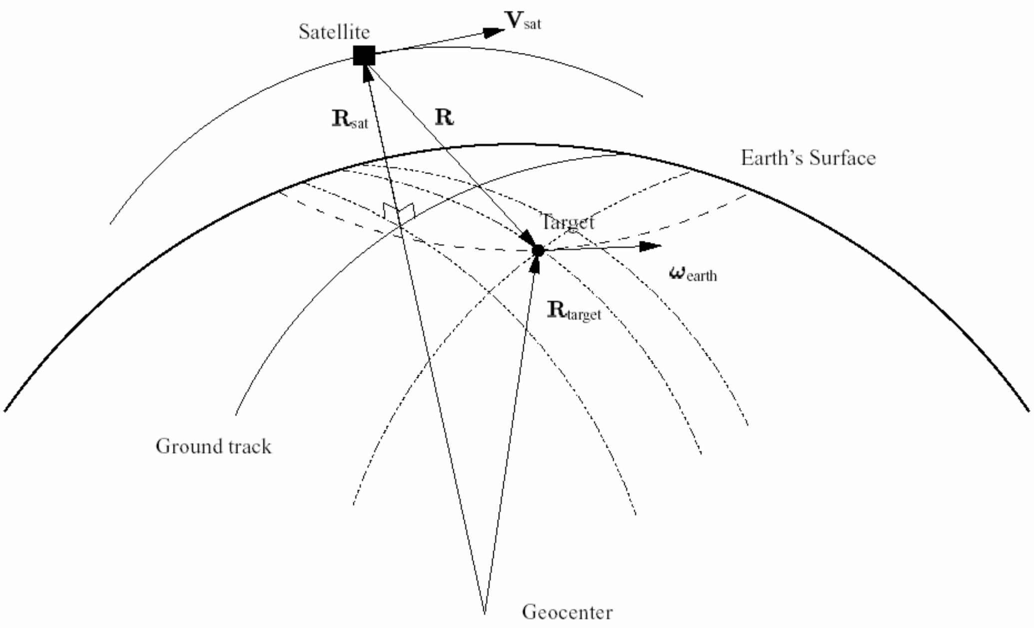

Fig.1.1 SAR acquisition real geometry

It is necessary to consider the Earth rotation and the satellite orbit ellipticity; but it is possible to consider an equivalent geometry, in that the satellite moves with velocity relative between satellite and target V_{st}, and the motion is on a flat surface (fig.1.2).

We define *azimuth* the direction parallel to V_{st} and *range* the direction orthogonal to V_{sat}.

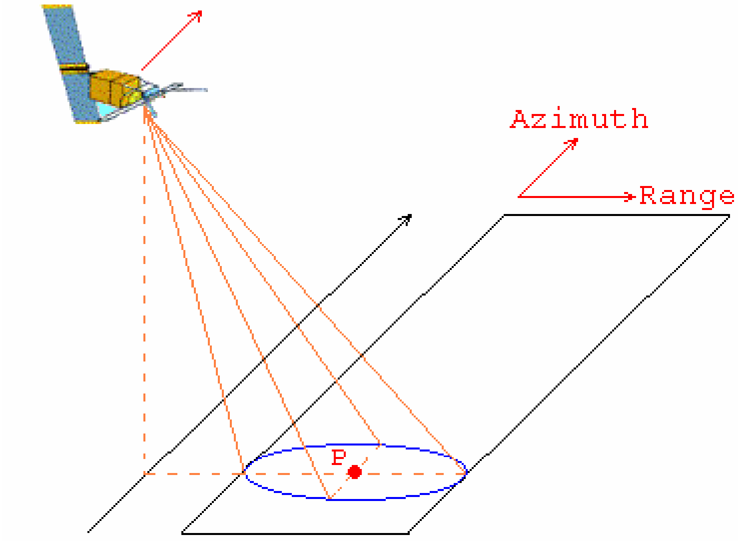

Fig.1.2 SAR acquisition equivalent geometry

In the *strip-map* acquisition mode the antenna beam has a fixed pointing direction respect to the platform; the beam direction forms an angle with the vertical passing by the satellite, defined elevation angle.

The foot-print is represented as an ellipse, in that the axis are proportional to the main-lobe width on the azimuth and range plan.

The integration time (time in that the pixel remains inside of the azimuth footprint) is related to the azimuth main lobe widht, so to the azimuth physical antenna lenght.

1.3 BIDIMENSIONAL CORRELATION PROCESSING

In this chapter we show the function that relates the backscattering amplitude function ζ with the received voltage of the SAR [1].

The received voltage phasor is obtained from the convolution between the system impulse function and the backscattering amplitude function:

$$v_r(\underline{R}) = \int_{-\infty}^{+\infty} h(\underline{R} \mid \underline{R}')\zeta(\underline{R}')d\underline{R}' \qquad (1.1)$$

To focus a surface element we need to know the radial distance from the satellite and the time in that it is at the center of azimuth antenna pattern.

The impulse response function of an surface element at a distance R from the satellite is scattered in a bidimensional space, with a spatial extension in range of cτ/2 (where τ is the pulse time) and in azimuth of $\theta_{az} R$ (where θ_{az} is the width to -3dB of the azimuth antenna pattern).

The SAR processing is a compression process that focuses the impulse response function around a point: it is operated applying a bi-dimensional correlation on the received signal with a bi-dimensional reference signal $h^{-1}(R_o \mid R)$:

$$\zeta(R_0) = \int_{-\infty}^{+\infty} h^{-1}(R_o|R) v_r(R) dR \,. \tag{1.2}$$

In the following chapters we will analyze the processing steps to obtain the image from the raw data.

1.4 SAR PROCESSING

The raw data must be hardly processed to give the desired informative content on the backscattered energy.

The SAR processing algorithms can be divided in 3 classes:

1. Algorithms based on the matched filtering;
2. Algorithms based on the spectral analysis;
3. Algorithms in the wavelength domain.

In this thesis we consider the first class; particularly, the algorithm that works in the time domain is analyzing, so-called Time Domain Correlation (TDC).

This algorithm compresses the SAR raw data operating two separated correlation in range and in azimuth in the time domain.

The algorithm is divided into 3 major steps:

1) Range compression;
2) Range migration compensation;
3) Azimuth compression for every pixel in the time domain.

In the following we start from the base-band signal expression and analyze every step to obtain the focused data.

1.4.1 IMPULSE RESPONSE FOR A STRIP-MAP SAR AND BASE-BAND SIGNAL

The signal transmitted from a SAR is moduled linearly in frequency (linear chirp):

$$s(t) = \cos\left[2\pi\left(f_c t + K\frac{t^2}{2}\right)\right] \qquad -\frac{\tau}{2} \le t \le \frac{\tau}{2}, \tag{1.3}$$

where K is the chirp slope, f_c the carrier frequency and τ the pulse time.

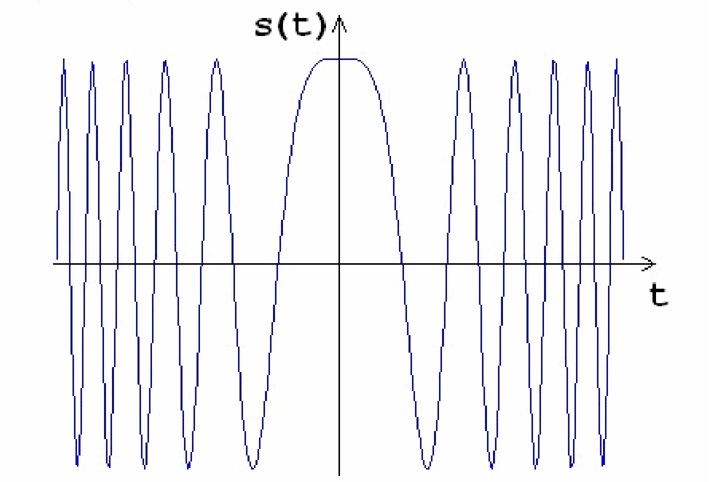

Fig.1.3 Linear chirp signal

The time and the frequency are related from the following:

$$(f - f_c) = K(t - t_c), \tag{1.4}$$

as shown in Fig. 1.4.

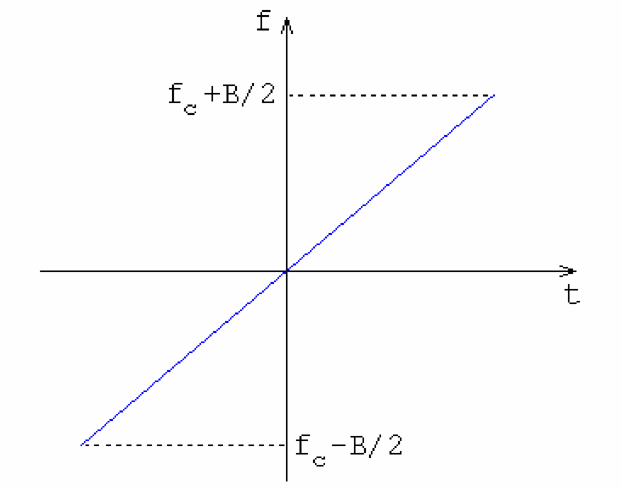

Fig.1.4 Time-frequency relation of a chirp signal

For a linear-chirp signal, the IRF (Impulse Response Function) of the SAR is a bi-dimensional function depending on the slow time (or azimuth time s) and fast time (or slant range time t):

$$h(s,t \mid s_c, R_c) = \cos\left\{2\pi\left[f_c\left(t-2\frac{R(s)}{c}\right)+\frac{K}{2}\left(t-2\frac{R(s)}{c}\right)^2\right]\right\}, \qquad (1.\ 5)$$

with $\left|t-2\frac{R(s)}{c}\right| \le \frac{\tau}{2}$, $\left|s-s_c\right| \le \frac{S}{2}$,

where s_c is the time at which the target is at the center of the synthetic aperture with a radial distance R_c and τ the pulse time.

S is the integration time, within which the target remains in the synthetic aperture radar:

$$S = \frac{\lambda \cdot R_c}{V_{st} \cdot L_a}, \qquad (1.6)$$

where L_a is the physical length of the antenna and V_{st} is the satellite velocity.

Note that for the duality between time and frequency, the corresponding of the integration time in the frequency domain is the Doppler bandwidth B_D.

The base-band signal of the received data results:

$$\hat{v}_r(s,t) = 0{,}5\exp\left[-j4\pi\frac{R(s)}{\lambda}\right]\cdot\exp\left\{j\pi K\left[t-2\frac{R(s)}{c}\right]^2\right\}, \qquad (1.7)$$

with $\left|t-2\frac{R(s)}{c}\right| \le \frac{\tau}{2}$.

1.4.2 RANGE COMPRESSION

Considering that the banda-base transmitted signal is

$$s(t) = 0.5\exp(j\pi K t^2), \qquad |t| \le \tau/2. \qquad (1.8)$$

The range compression is calculated from the correlation:

$$g(s,t) = \int_{t-\frac{\tau}{2}}^{t+\frac{\tau}{2}} \hat{v}_r(s,t')s^*(t'-t)dt'. \qquad (1.9)$$

From a computational point of view, it is better to operate the correlation in the frequency domain. The transfer function of the range filter is H(f)=1/S(f), and the signal spectrum at the filter output is:

$$G(s,f)=\hat{V}_r(s,f)\cdot H(f)=\exp\left(-j4\pi\frac{R(s)}{\lambda}\right)\cdot\exp\left(-j4\pi f\frac{R(s)}{c}\right), \qquad (1.10)$$

with $|f|\le B/2$.

Returning in the time domain, the range compressed echoes of a surface element that is at the time s_c is at the center of the radiation pattern with a radial distance R_c are:

$$\hat{g}(s,t)=B\exp\left(-j4\pi\frac{R(s)}{\lambda}\right)\cdot\operatorname{sinc}\left\{\pi B\left[t-2\frac{R(s)}{c}\right]\right\}, \qquad (1.11)$$

with $s = s_n$, n=1,2,….,N.

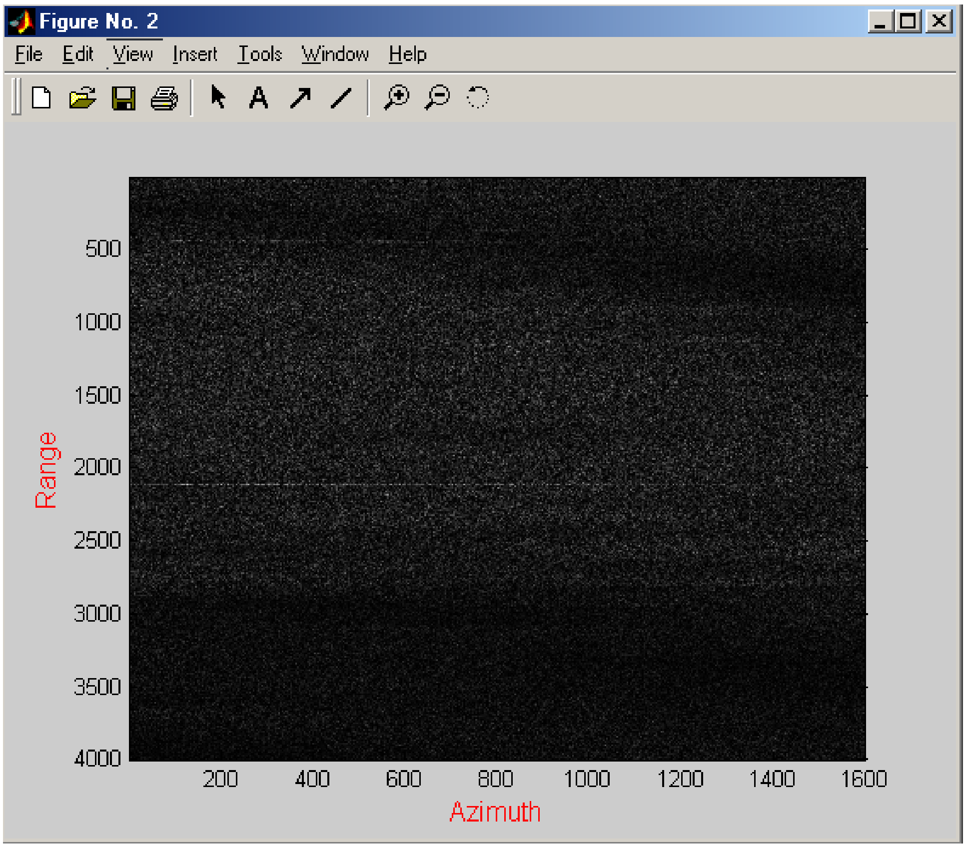

Fig.1.5 Amplitude image of range compressed data

1.4.3 RANGE MIGRATION COMPENSATION

In the SAR processing the range varies with the azimuth time, and *R(s)* is defined by the called range equation [2]. To obtain a fine azimuth resolution is necessary to take in account this variation, which causes a phase modulation from pulse to pulse.

R(s) has a hyperbolic form, but can be approximated as parabolic function for low squint angles, as shown in the following.

For the digital nature of the SAR data, the range compressed data (1.11) are available only in the points of the grid (s_m, R_n).

The range migration compensation has the aim to generate for every pixel a mono-dimensional vector along the parabolic trajectory.

To obtain the range compressed data for every radial distance at all the azimuth samples, we reconstruct the range signal sampled with f_s frequency for all the value of *R(s)*, using the time domain interpolation.

At this aim we use the *Whittaker interpolation* [1].

f(t) is a complex signal in base-band, for that $|F(j\omega)| = 0$, $|f| > \frac{B}{2}$.

If the sampling is operated with a frequency $f_s \geq B$, the signal can be reconstructed for the Nyquist Theorem.

The interpolation allows to recontruct the signal with the following convolution:

$$f(t) = \sum_{n=-\infty}^{\infty} f\left(\frac{n}{f_s}\right) \mathrm{h}\left(t - \frac{n}{f_s}\right) \tag{1.12}$$

where $\mathrm{h}\left(t - \frac{n}{f_s}\right)$ is the interpolation Kernel.

The Whittaker interpolation uses a sinc-kernel:

$$f(t) = \sum_{n=-\infty}^{\infty} f\left(\frac{n}{f_s}\right) \mathrm{sinc}\left[\pi \cdot f_s \left(t - \frac{n}{f_s}\right)\right]. \tag{1.13}$$

The problem is that a band-limited signal is infinite in the time domain; because in the reality the signal is not stringently band limited, the interpolation can be operated on a finite number of points N_0.

So we consider $f\left(\frac{n}{f_s}\right) = 0$ for $|n| > N_0$.

For the digital nature of the data, the range compressed data are stored in corrispondence of the nodes (m,n):

$$\hat{g}(s_m, R_n) = \exp\left[-\frac{j4\pi R(s_m)}{\lambda}\right] \mathrm{sinc}\left\{\frac{2\pi B_\mathrm{R}}{c}\left[R_n - R(s_m)\right]\right\}, \tag{1.14}$$

where m is the pulse number corresponding to the time s_m, R_n is the range bin and B_R is the range signal band.

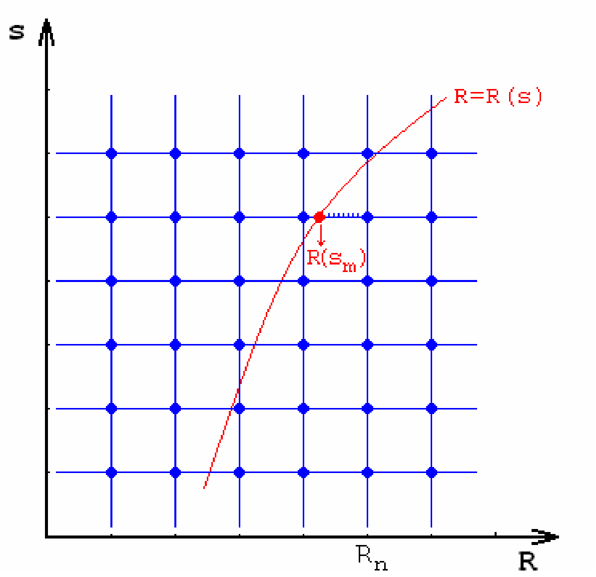

Fig.1.6 Range migration on the grid

The range migration on the greed results $\Delta R(s_m) = R(s_m) - R_c$.

Considering t_0 the time relative to the near slant range, the slant range time of the n^th sample is $t_{sr} = t_0 + \dfrac{(n-1)}{f_s}$.

Note that the relation between time and space is the following: $t_{srk} = \dfrac{2R(s_k)}{c}$.

To focus the pixel corresponding to the pulse s_m, the adjacent range sample are interpolated. So the range sample corresponding to the time t_{srk} results:

$$\hat{g}(s_k, R(s_k)) = \sum_{i=-a}^{+b} \hat{g}\left(s_k, R_i\right) \operatorname{sinc}\left[\pi f_s \left(\frac{2\cdot\left(R(s_k)-R_c\right)}{c} - \frac{i}{f_s}\right)\right], \tag{1.15}$$

where $\dfrac{i}{f_s}$ are the sampling instants; the origin is at the time $t_0 = \dfrac{2R_c}{c}$.

The parameters (a,b) represent the number N_0 of range samples, used in the interpolation.

Because the kernel is made with a finite number of points, it is necessary to operate a normalization phase, with the intent of unify the interpolator gain.

If we have a signal with constant amplitude, the normalizad interpolated value is:

$$\hat{g}^{'}(s_k, R(s_k)) = \frac{\hat{g}(s_k, R(s_k))}{S}, \tag{1.16}$$

where S is the sum of the kernel weights:

$$\mathrm{S}=\sum_i \operatorname{sinc}\left[\pi \cdot f_s \cdot \left(\frac{2\cdot\left(R(s_k)-R_c\right)}{c}-\frac{i}{f_s}\right)\right]. \tag{1.17}$$

If the signal has constant power, the normalization constant results:

$$\mathrm{S}_2=\sqrt{\sum_i \operatorname{sinc}^2\left[\pi \cdot f_s \cdot \left(\frac{2\cdot\left(R(s_k)-R_c\right)}{c}-\frac{i}{f_s}\right)\right]}. \tag{1.18}$$

Finally, to avoid the Gibbs phenomenon, we weigh the sinc kernel with a Hamming windows:

$$w(t)=\alpha+(1-\alpha)\cdot\cos\left(\frac{2\pi\cdot s}{S}\right). \tag{1.19}$$

1.4.4 AZIMUTH COMPRESSION

Starting from (1.11), for every pixel of the image with coordinates (R_c, s_c) the azimuth compression is calculated from the correlation:

$$\zeta(s_c', s_c, R_c)=\int_{s_c-S/2}^{s_c+S/2} \hat{g}(s\,|\,s_c, R_c)\,h_{az}^{-1}(s-s_c'\,|\,s_c, R_c)\,ds, \tag{1.20}$$

where the impulse response of the azimuth filter is the following:

$$h_{az}^{-1}\left(s\,\middle|\,s_c, R_c\right)=\exp\left\{j\frac{4\pi}{\lambda}\left[R(s)-R_c\right]\right\}. \tag{1.21}$$

The backscattering function results:

$$\zeta(s_c', R_c, s_c)=S\cdot\operatorname{sinc}\left[\pi\frac{2V_{st}^2}{\lambda R_c}S(s_c'-s_c)\right]. \tag{1.22}$$

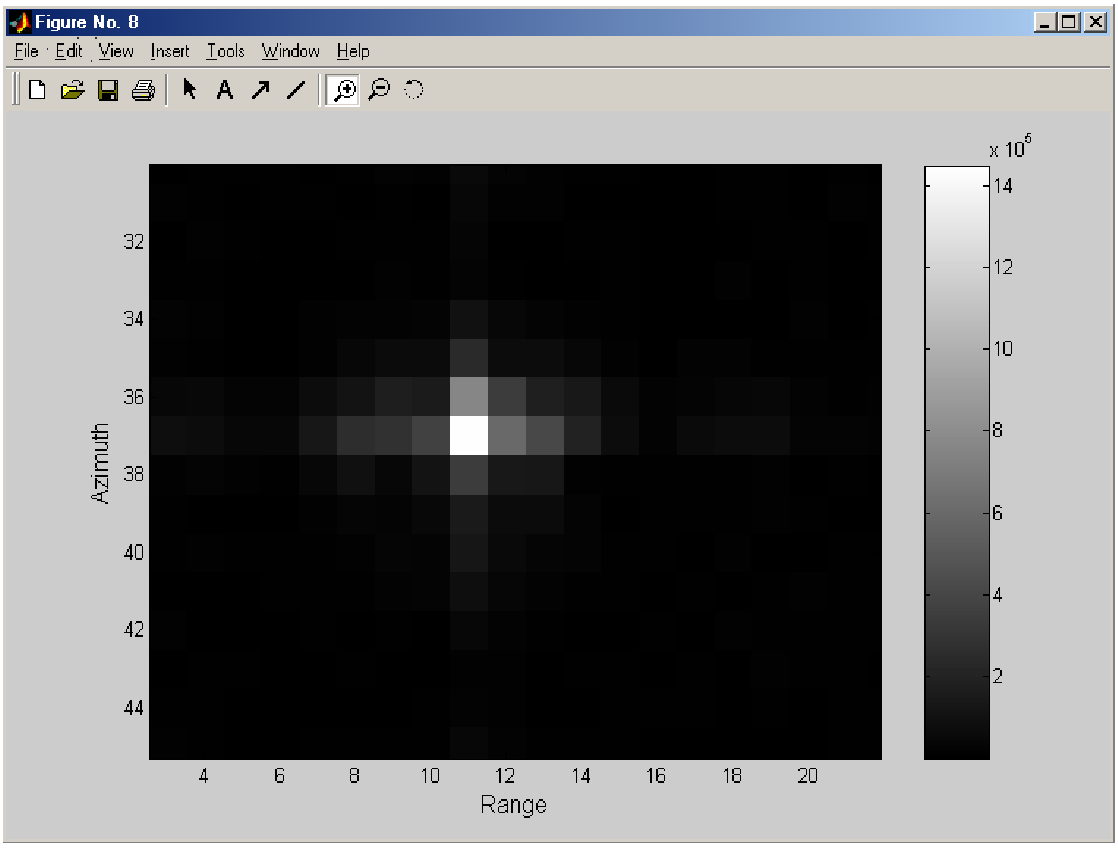

Fig.1.7 Amplitude image of focused data after azimuth compression

1.4.5 PHASE SIGNAL APPROXIMATION

The fundamental key of the azimuth compression is the knowledge of the phase of the Doppler signal $\Phi = -\frac{4\pi R(s)}{\lambda}$, generated by the relative motion between satellite and target; *R(s)* is so the the slant range in function of the azimuth time during the integration time.

If *S* is small enough, *R(s)* can be developed in Taylor series around s_c [1]:

$$R(s) \approx R_c + \dot{R}_c(s - s_c) + \ddot{R}_c \frac{(s - s_c)^2}{2} + \ldots \qquad (1.23)$$

In the standard SAR processing (for stationary scene focalization) the terms with degree higher than the second can be ignored; so the Doppler signal phase, the Doppler frequency and its temporal derivative result respectively:

$$\Phi = -\frac{4\pi R(s)}{\lambda} \qquad (1.24)$$

$$f_D = \frac{\dot{\Phi}}{2\pi} = -\frac{2\dot{R}(s)}{\lambda} \tag{1.25}$$

$$f_R = \frac{\ddot{\Phi}}{2\pi} = -\frac{2\ddot{R}(s)}{\lambda} \tag{1.26}$$

The terms $\dot{R}_c$ and $\ddot{R}_c$ are proportional to the Doppler parameters f_{Dc} e f_R defined at the time $s = s_c$:

$$\begin{cases} \dot{R}_c = -\dfrac{\lambda \cdot f_{Dc}}{2} \\ \ddot{R}_c = -\dfrac{\lambda \cdot f_R}{2} \end{cases} \tag{1.27}$$

The slant range can be so represented from the following parabolic expression:

$$R(s) = R_c - \lambda \frac{f_{Dc}}{2}(s - s_c) - \lambda \frac{f_R}{2}\frac{(s - s_c)^2}{2}, \qquad |s - s_c| \le \frac{S}{2} \tag{1.28}$$

The phenomenon of variation of the distance between satellite and target during the azimuth time $R(s) - R_c$, called *range migration*, is an effect of the SAR acquisition mode.

1.5 SAR PROCESSING AT DOPPLER CENTROID AND AT ZERO DOPPLER

There are two methods to process the data: we can focus the pixel at the center of the synthetic aperture (Doppler Centroid) or the pixel that is at Doppler frequency null (Zero Doppler).

Let s_0 the time in that the Doppler frequency is null. We consider $\eta = s - s_0$, and $\eta_c = s_c - s_0$. Remembering the time-frequency relation for a chirp signal $f - f_0 = K(t - t_0)$, it results:

$$s - s_c = \frac{1}{f_R}(f - f_{Dc}). \tag{1.29}$$

We can derive

$$\eta_c = s_c - s_0 = \frac{1}{f_R}(f_{Dc} - 0) = \frac{f_{Dc}}{f_R}. \tag{1.30}$$

The slant range in the Doppler Centroid processing is represented from (1.28); in the Zero Doppler processing it becomes:

$$R(\eta) = R_0 - \lambda \frac{f_R}{4}\eta^2 , \tag{1.31}$$

where $R_0 = R(s_0)$.

Fig.1.8 shows the relation between range migration and Doppler frequency.

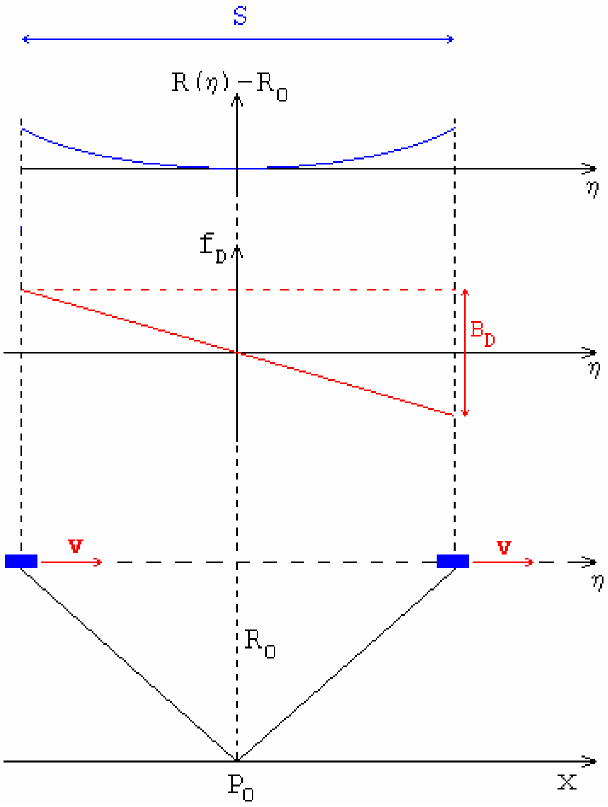

Fig.1.8 Relation between range migration and Doppler frequency

1.6 EFFECTS OF THE MOTION ON THE SIGNAL PHASE

In the SAR image the moving target is characterized by a signal phase different from the static background. An analysis of the moving target signal and of the resulting effects is proposed in the following.

In the following we take in account the model proposed by [3], considering the zero Doppler processing: this model starts from the geometric characteristics of the scene.

We suppose that the object moves in the plane azimuth-range. Considering a moving scatterer along the range and azimuth direction, the velocity vector is (v_{rg}, v_{az}) and the acceleration (a_{rg}, a_{az}), H the satellite height, ϑ the local elevation angle and y_0 the range coordinate of the target at the time η_c ($y_0 = R_0 \cdot \sin\vartheta$).

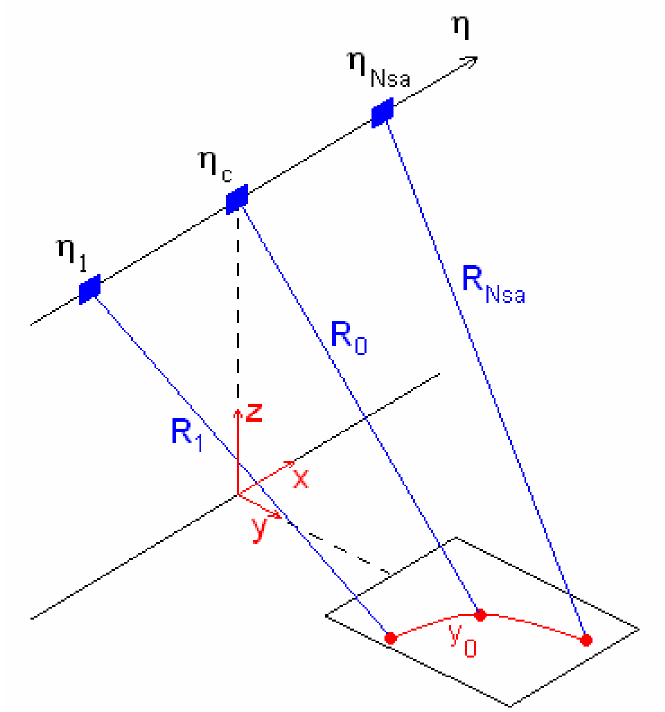

Fig.1.9 SAR geometry for a moving target

The slant range in function of the azimuth time is represented from the following:

$$R(\eta) = \sqrt{\left(v_{az}\eta + \frac{a_{az}}{2}\eta^2 - V_{sat}\eta\right)^2 + \left(y_0 + v_{rg}\eta + \frac{a_{rg}}{2}\eta^2\right)^2 + H^2} \,. \tag{1.32}$$

Considering that $v_{rg}^2 \ll R_0^2$ and $v_{rg}\left(v_{az} - V_{sat}\right)^2 \ll R_0^2$, the function can be expanded in Taylor series around to $\eta - \eta_c$:

$$R(\eta) \approx R(0) + \frac{1}{1!}\dot{R}(\eta)\Big|_{\eta=0}\eta + \frac{1}{2!}\ddot{R}(\eta)\Big|_{\eta=0}\eta^2 + \frac{1}{3!}\dddot{R}(\eta)\Big|_{\eta=0}\eta^3 + \ldots\ldots \tag{1.33}$$

Function $R(\eta)$ becomes:

$$\begin{aligned} R(\eta) \approx{}& R_0 + \frac{y_0 v_{rg}}{R_0}\eta + \frac{1}{2R_0}\left[\left(v_{az} - V_{sat}\right)^2 + v_{rg}^2\left(1 - \frac{y_0^2}{R_0^2} + y_0 a_{rg}\right)\right]\eta^2 + \\ &+ \frac{1}{2R_0}\left[v_{rg}a_{rg}\left(1 - \frac{y_0^2}{R_0^2}\right) + a_{az}\left(v_{az} - V_{sat}\right)\right]\eta^3 \end{aligned} \,. \tag{1.34}$$

Supposing that the scatterer moves with constant velocity, the expansion stops to the second order:

$$R(\eta) \approx R_0 + \frac{y_0 v_{rg}}{R_0}\eta + \frac{1}{2R_0}\left[\left(v_{az} - V_{sat}\right)^2 + v_{rg}^2\left(1 - \frac{y_0^2}{R_0^2}\right)\right]\eta^2 . \tag{1.35}$$

The phase of the signal results

$$\Phi = 4\pi\frac{R(\eta)}{\lambda} = \frac{4\pi}{\lambda}\left\{R_0 + \frac{y_0 v_{rg}}{R_0}\eta + \frac{1}{2R_0}\left[\left(v_{az} - V_{sat}\right)^2 + v_{rg}^2\left(1 - \frac{y_0^2}{R_0^2}\right)\right]\eta^2\right\}. \tag{1.36}$$

In the following paragraphs we propose a separated analysis of range and azimuth velocity.

1.6.1 EFFECTS OF THE RANGE VELOCITY

We suppose that the target moves with range velocity v_{rg}; the slant range velocity results $v_{sr} = v_{rg} \cdot sen(\vartheta)$.

The principal effect of the range velocity of a moving target is the variation of the linear term of the phase; this variation changes the Doppler centroid of the moving target and introduces an additional phase term:

$$\hat{g}(\eta \mid \eta_c, R_c) = B\exp\left(-j\frac{4\pi R(\eta)}{\lambda}\right)\cdot\left(-j\frac{4\pi}{\lambda}v_{sr}\cdot\eta\right). \tag{1.37}$$

This term causes a shift of the Doppler spectrum.

Considering the relation time-frequency, the shift in the frequency domain becomes an azimuth shift in the time domain [4]:

$$\eta_{shift} = \frac{2v_{sr}}{\lambda \cdot f_R}. \tag{1.38}$$

So in the SAR image focused with a stationary matched filter the moving target is focused with a spatial displacement from the real position

$$\Delta_{azimuth} = -R\frac{v_{sr}}{V_{sat}} = v_B \cdot \eta_{shift}, \tag{1.39}$$

where v_B is the beam velocity on ground.

The second effect of the range velocity is a little variation of the quadratic term; in fact, from (1.35) the additional term $v_{rg}^2\left(1 - \frac{y_0^2}{R_0^2}\right)$ appears in the phase expression.

When a stationary matched filter is used to focus the SAR image, this additional term causes a mismatching of the quadratic part of the phase, and this causes a light azimuth and range defocusing and amplitude decreasing.

The effects of the range velocity are shown in Fig.1.10 and 1.11: in the first graphic we can observe the difference between the slant range of a static and moving target, in the second we can note the azimuth shift of the moving object and the amplitude decreasing, when a stationary filter is used.

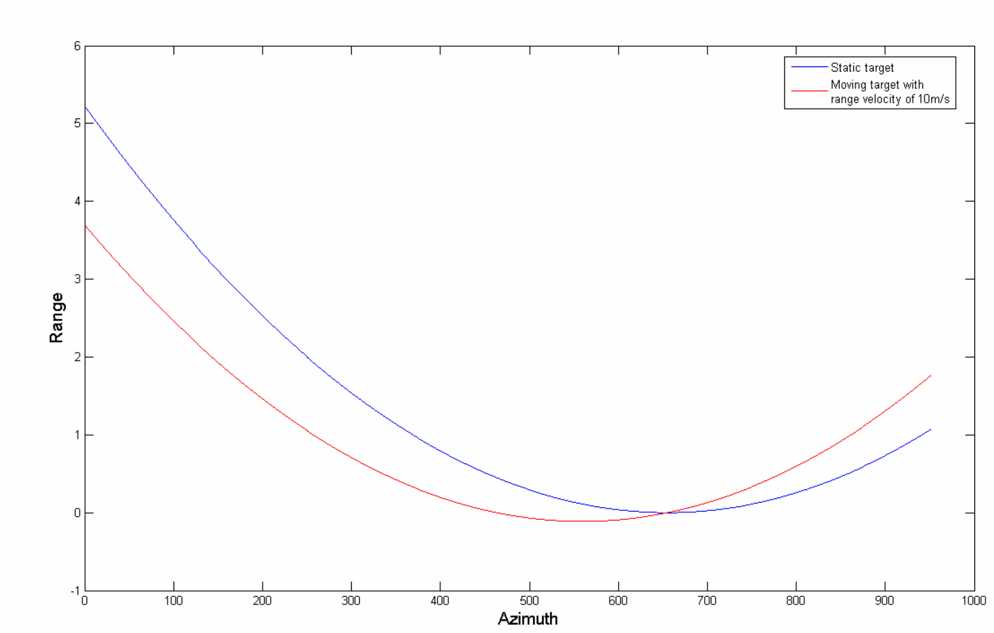

Fig.1.10 Comparison of the slant range of a stationary and range moving target

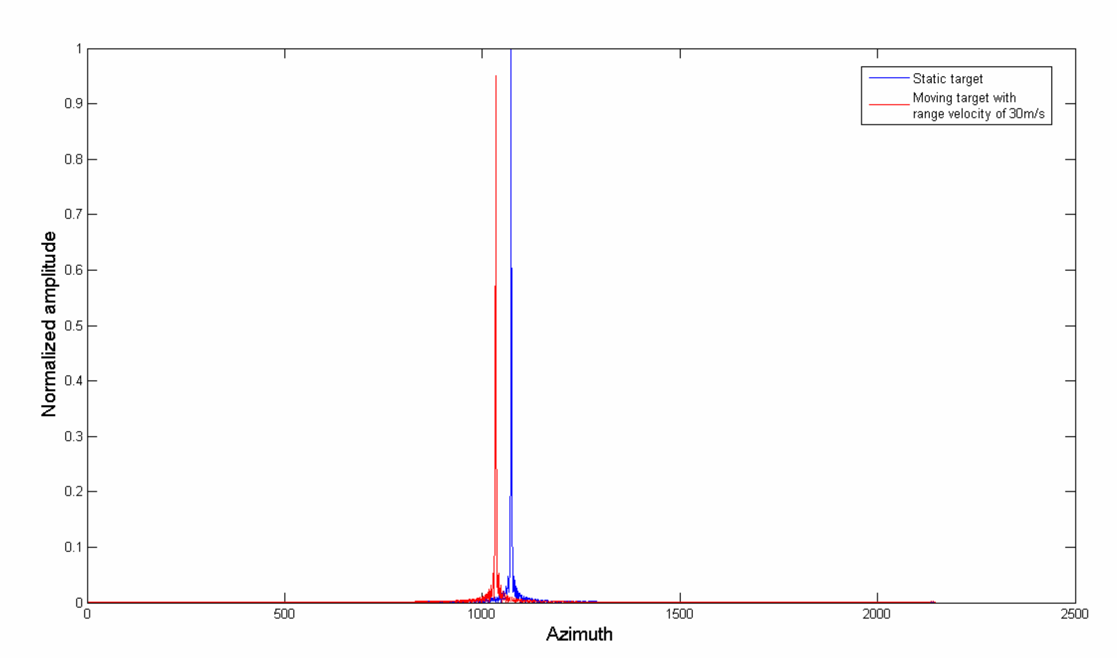

Fig.1.11 Effects caused from range velocity using a stationary matched filter

1.6.2 EFFECTS OF THE AZIMUTH VELOCITY

If the moving target moves with constant azimuth velocity v_{az}, it causes a variation of the quadratic term of the phase, as it is possible to observe in (1.36), Using a stationary matched filter to focus the data, the azimuth velocity generates a mismatching of the quadratic term of the phase, that corresponds to a variation of the Doppler Rate [4]:

$$f_R^{'} = f_R \cdot \left(1 - \frac{v_{az}}{v_B}\right)$$

This mismatching generates a spread in azimuth of the energy returned by the target, so the image of the moving target is smeared. The effects are azimuth defocusing and decrease in amplitude, as is shown in Fig.1.11.

The effects of the azimuth velocity are shown in Fig.1.12 and 1.13: in the first graphic the difference between the slant range of a static and moving target is represented, in the second the azimuth defocusing and the decrease in amplitude are stressed.

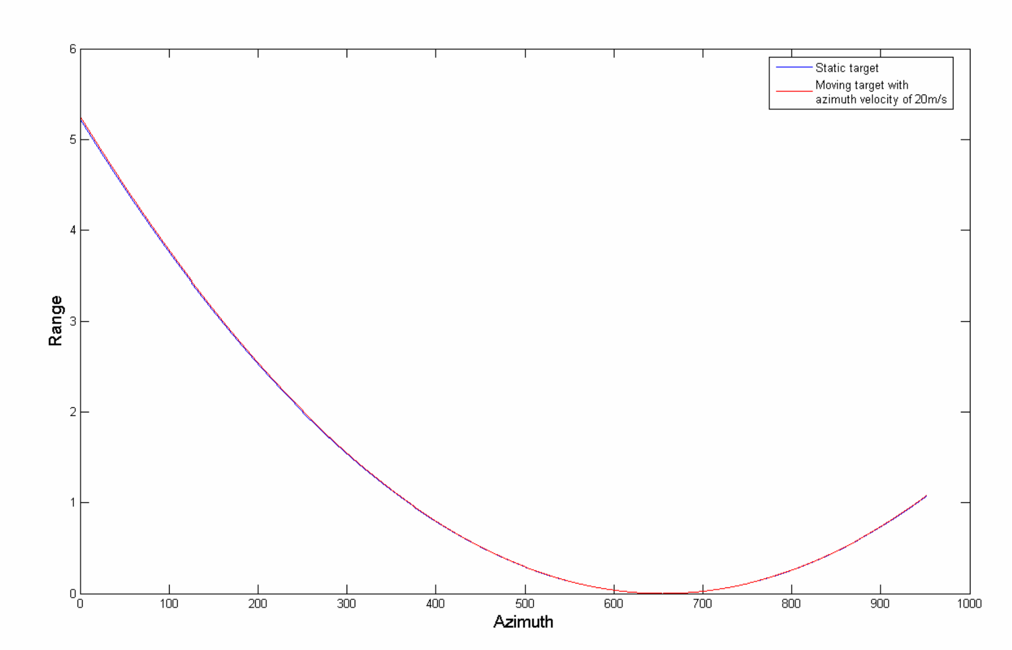

Fig.1.12 Comparison of the slant range of a stationary and azimuth moving target

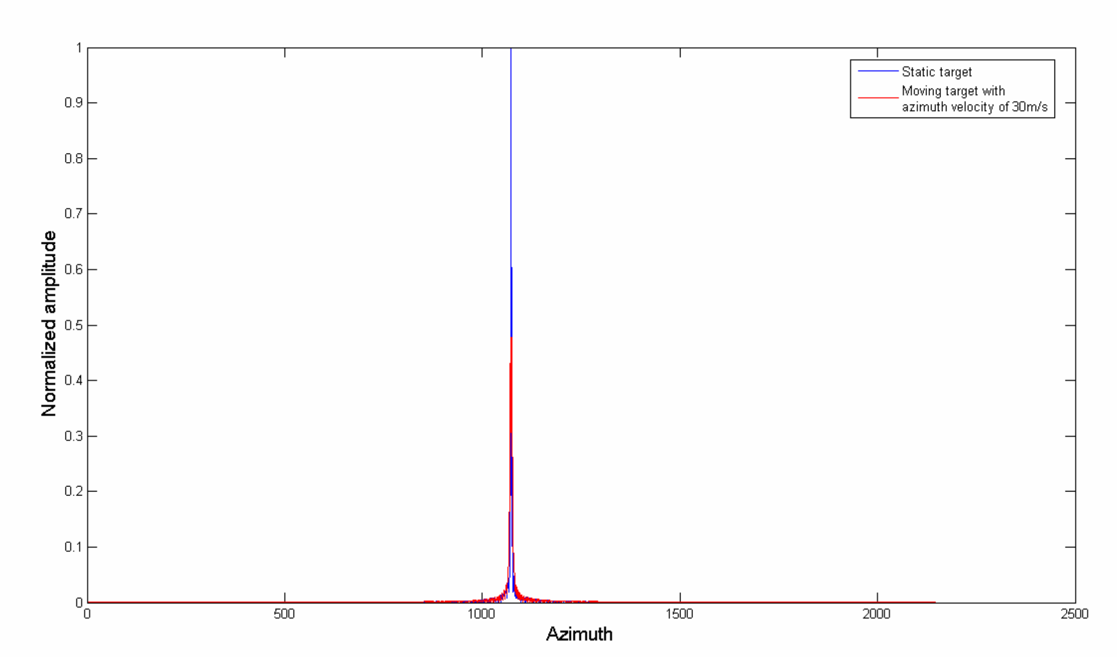

Fig.1.13 Effects caused from azimuth velocity using a stationary matched filter

Fig.1.14 proposes a zoom of the Fig.1.11, so it is easier to observe the decreasing of the spatial resolution.

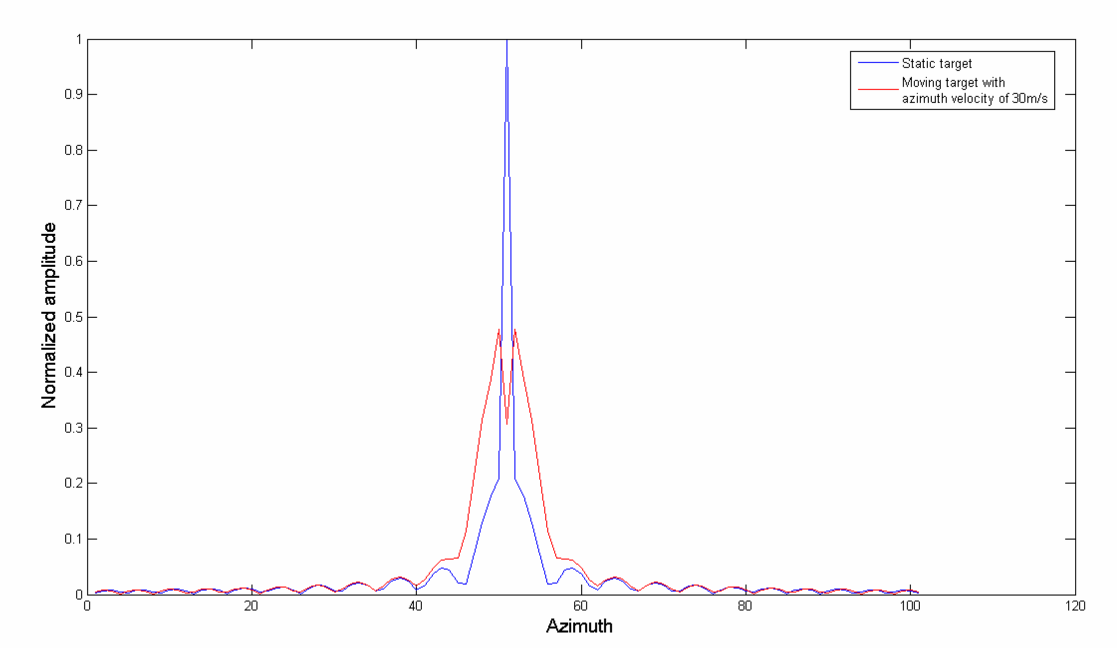

Fig.1.14 Zoom of the effects caused from azimuth velocity

REFERENCES

[1] J.C. Curlander, R. McDonough, ”Synthetic Aperture Radar, Systems and Signal Processing”, Wiley 1991.

[2] I.G. Cumming, F.H. Wong, ” Digital Signal Processing of Synthetic Aperture Radar Data: Algorithms and Implementation”, Artech House January 2005.

[3] J.J.Sharma, C.H.Gierull, M.J.Collins, “The influence of Target Acceleration on Velocity Estimation in Dual-Channel SAR-GMTI”, IEEE Transactions on Geoscience and Remote Sensing, Vol. 44 , N. 1, pp. 134–147, Jan 2006.

[4] S.Hinz, F.Meyer, A.Laika, R.Bamler, “Spaceborne traffic monitoring with Dual Channel Synthetic Aperture Radar – Theory and Experiments”, Proceedings of the IEEE, Computer Society Conference on, CVPR 2005, Vol.3, Pag.7-7, 20-26 June 2005.

CHAPTER 2

SAR RAW DATA SIMULATOR OF MOVING TARGETS

2.1. INTRODUCTION

Working on GMTI (Ground Moving Target Indication) techniques, the most difficulty is find the raw data fit for this aim; in fact this application field is typically considered military domain, and the raw data are hardly made available to the civil users.

The best solution is to use a SAR raw data simulator, which simulates the raw data generation starting from the mathematics theory of SAR processing.

This requires certainly the a priori understanding of the electromagnetic interaction between transmitted signal and target, as shown in chapter 1.

The SAR raw data simulator here implemented generates the raw data of a static background with moving target, using the theory introduced in Chapter 1.

The key of the simulator that allows to simulate the motion of a target is the knowledge of the uncompressed impulse response function of the SAR, that takes in account the geometry of the scene and the dynamic characteristics of the single target.

The data are generated for each pixel and summed, according to the overlap principle: the simulator produces the voltage levels from the scene in the raw domain for every scatterer.

2.2 RAW DATA GENERATION PROCESS

For a linear chirp the IRF results [1]:

$$h(s,t \mid s_c, R_c) = \cos\left\{2\pi\left[f_c\left(t-2\frac{R(s)}{c}\right)+\frac{K}{2}\left(t-2\frac{R(s)}{c}\right)^2\right]\right\}, \tag{2.1}$$

with $\left|t-2\frac{R(s)}{c}\right| \le \frac{\tau}{2}$ and $\left|s-s_c\right| \le \frac{S}{2}$,

where the range and azimuth variables are couplet, as shown in the mathematical expression.

The received signal in base-band has the following expression:

$$\hat{v}_r(s,t) = 0{,}5\exp\left[-j4\pi\frac{R(s)}{\lambda}\right]\cdot\exp\left\{j\pi K\left[t-2\frac{R(s)}{c}\right]^2\right\}. \tag{2.2}$$

Considering the zero Doppler azimuth time η and that the informative contents is given by phase differential quantity $R(\eta)-R_0$, we can model the received signal:

$$\hat{v}_r(\eta,t) = 0{,}5\exp\left[-j4\pi\frac{R(\eta)}{\lambda}\right]\exp\left\{j\pi K\left[t-2\frac{R(\eta)-R_0}{c}\right]^2\right\}. \tag{2.3}$$

The used slant range model is given by (1.35).

Fig.2.1 and 2.2 show the amplitude and the phase of the simulated raw data of a pointform scatterer.

We can observe in Fig.2.2 the hyperbolic phase contours, caused by the hyperbolic form of the range equation. Note that the phase contours are aliased, because the phase represents only part of the information in the complex signal, so plotting phase alone is equivalent to representing a complex signal by a real signal, and aliasing can result [2].

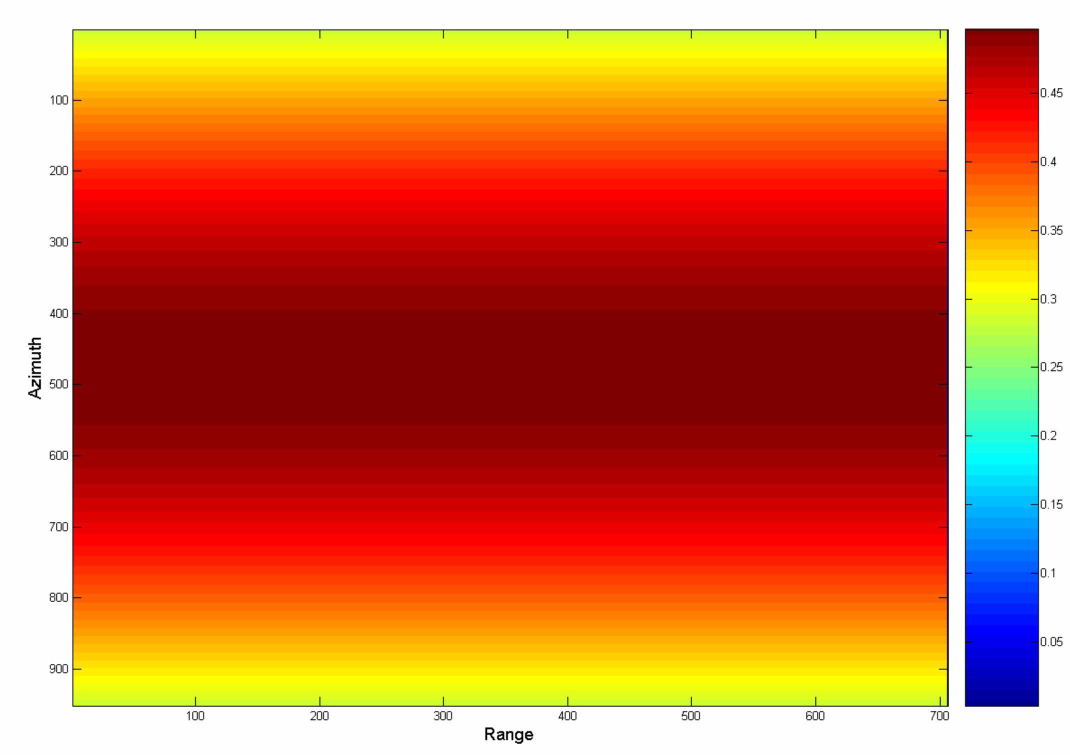

Fig.2.1 Raw data amplitude of a simulated pointform scatterer

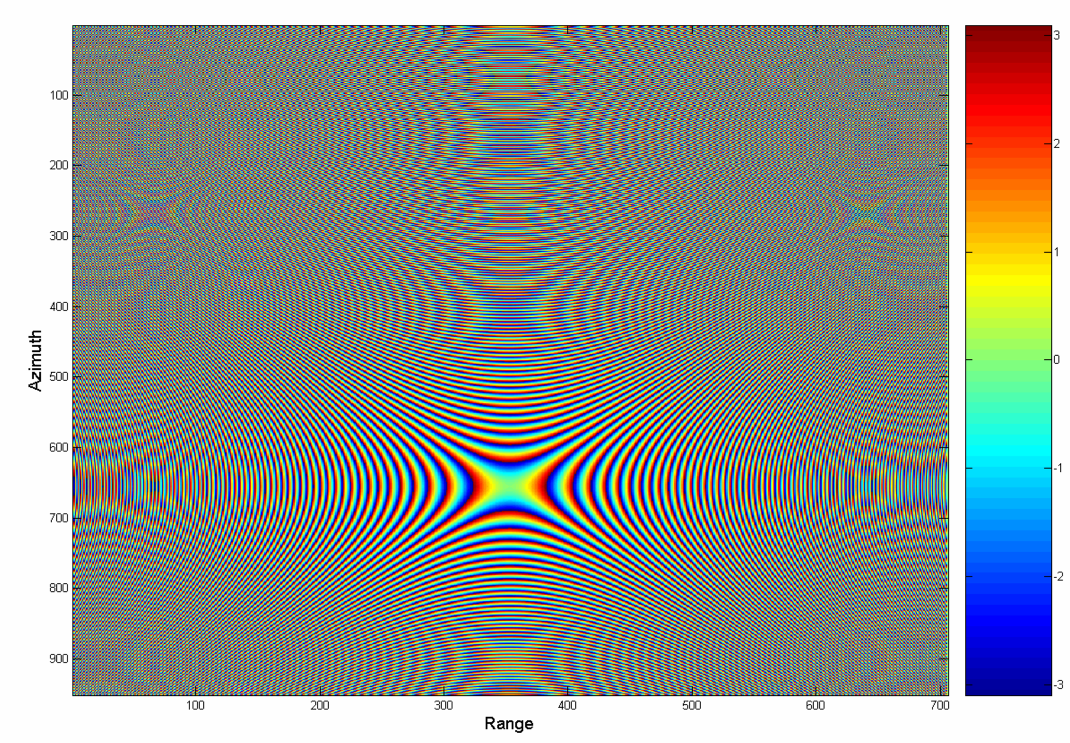

Fig.2.2 Raw data phase of a simulated pointform scatterer

2.3 ANTENNA PATTERN

Important information that we must take in account to characterize the SAR system is the azimuth antenna pattern, which considers the different spatial distribution of the transmitted energy.

The transmitted mode amplitude pattern of a planar radar antenna in the azimuth time is a sinc function that depends only on the physical size of the antenna [3].

Considering the zero Doppler time, represented from η $(\eta = s - s_{zd})$, θ is the angle between the slant range of the synthetic aperture and the slant rang at the zero Doppler time s_{zd}, as is shown in Fig.2.3.

The antenna pattern results [1]:

$$W_a = \mathrm{sinc}^2\left[\frac{\mathrm{L_a}}{\lambda}\cdot\sin\theta\right] \tag{2.4}$$

Because θ is very small, we approssimate the expression:

$\sin\theta \simeq \theta$.

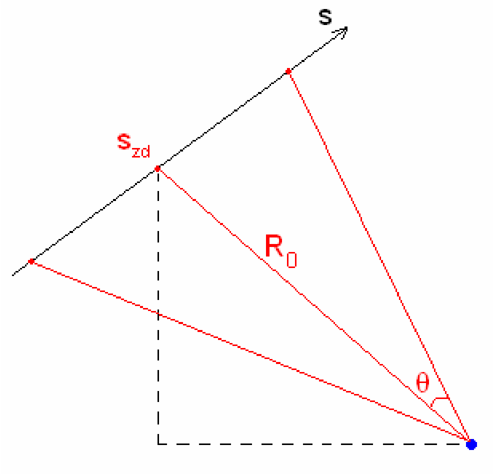

Fig.2.3 SAR geometry

Looking Fig.2.3, we can note that θ can be represented by the following:

$$\theta = tg^{-1}\left(\frac{\eta-\eta_c}{R_0}\right). \tag{2. 5}$$

It results finally:

$$W_a(\eta) = \mathrm{sinc}^2\left[\frac{\mathrm{L_a}}{\lambda}\cdot tg^{-1}\left(\frac{\eta-\eta_c}{R_0}\right)\right]. \tag{2.6}$$

Fig.2.4 shows the azimuth antenna pattern used to weigh the received pulses, in function of the azimuth time $(\eta-\eta_c)$.

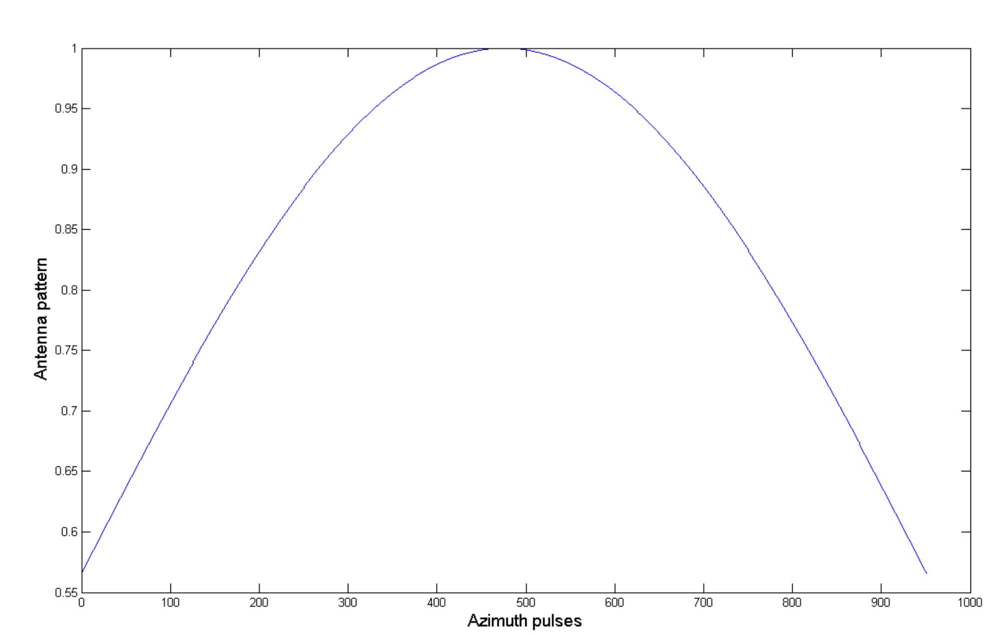

Fig.2.4 Azimuth antenna pattern

2.4 IMPLEMENTATION OF RAW DATA SIMULATOR ON MATLAB PLATFORM

For each scatterer the SAR impulse reference function is generated, with the aim to scatter the compress energy of the target in the bi-dimensional space in the raw domain. The function used is the following, in according with the expression (1.7):

$$h(\eta,t)=0,5\exp\left\{j\pi K\left[t-2\frac{R(\eta)-R_0}{c}\right]^2\right\}\cdot\exp\left[-j4\pi\frac{R(\eta)}{\lambda}\right]. \qquad (2.7)$$

Considering a pointform scatterer, in the raw domain we define N_{chirp} the sample number of the range direction, N_{sa} the sample number of the synthetic aperture lenght and $N_{centre}={}^{N_{sa}}\!/_{2}$ the center of the aperture.

The range and azimuth time are defined respectively:

$$t=\frac{n}{f_s}\text{, with }-\frac{N_{chirp}}{2}\le n\le+\frac{N_{chirp}}{2}.$$

where f_s is the sampling frequency.

$$\eta_n=s(n)-s_0=\frac{n-(N_{centre}-\eta_c)}{PRF},\qquad n=1,\ldots,N_{sa}. \qquad (2.8)$$

The scattering bidimensional function is obtain in form of matrix, taking in account the antenna pattern to weigh the impulse response function in azimuth.

The resulting matrix results:

$$hsar(\eta,t)=\begin{bmatrix} W_a(\eta_1)\cdot h(t_1,\eta_1) & \cdots & W_a(\eta_{N_{sa}})\cdot h(t_1,\eta_{N_{sa}}) \\ \vdots & \ddots & \vdots \\ W_a(\eta_1)\cdot h(t_{N_{chirp}},\eta_1) & \cdots & W_a(\eta_{N_{sa}})\cdot h(t_{N_{chirp}},\eta_{N_{sa}}) \end{bmatrix}. \qquad (2.9)$$

Now the results of the simulator are presented.

In Fig.2.5 the raw data of a pointform scatterer is shown; the raw data are zero padded.

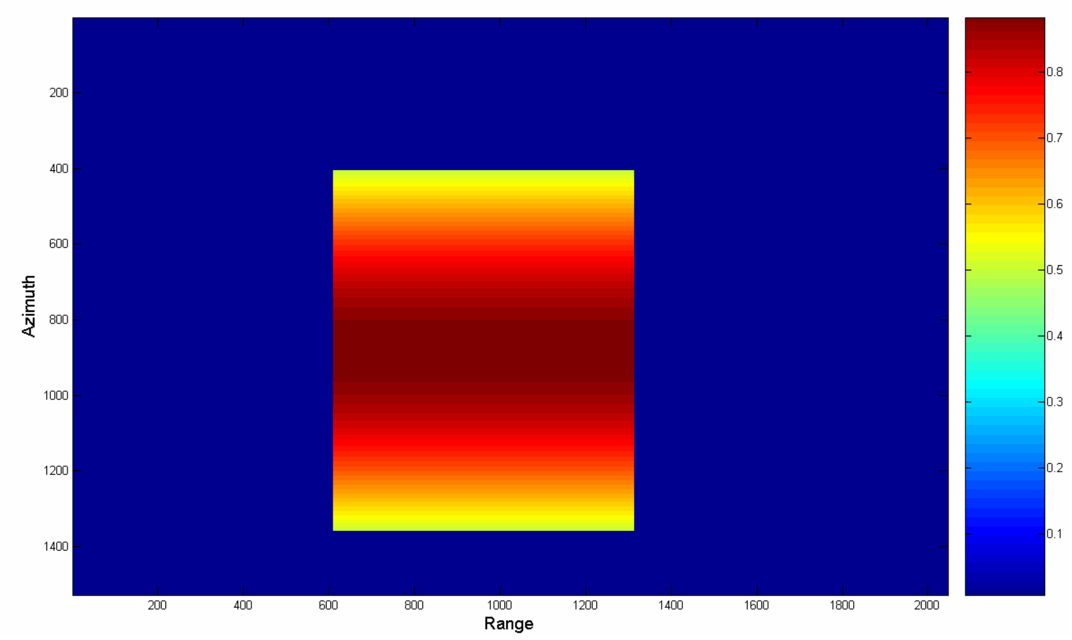

Fig.2.5 Raw data of a simulated pointform scatterer on an extended scene

To show the compression processing, we use the SAR processor in the time domain to focus the scatterer.

The results of the range compression are shown in Fig.2.6: to stress the range curvature for the range migration Fig.2.7 proposes a zoom of the target data.

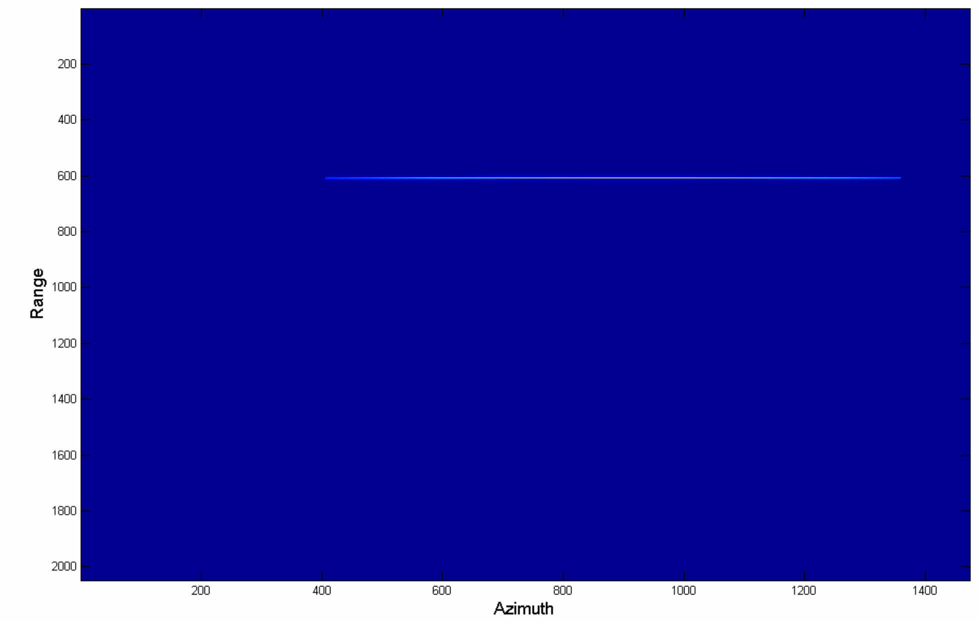

Fig.2.6 Range compressed data of the scatterer

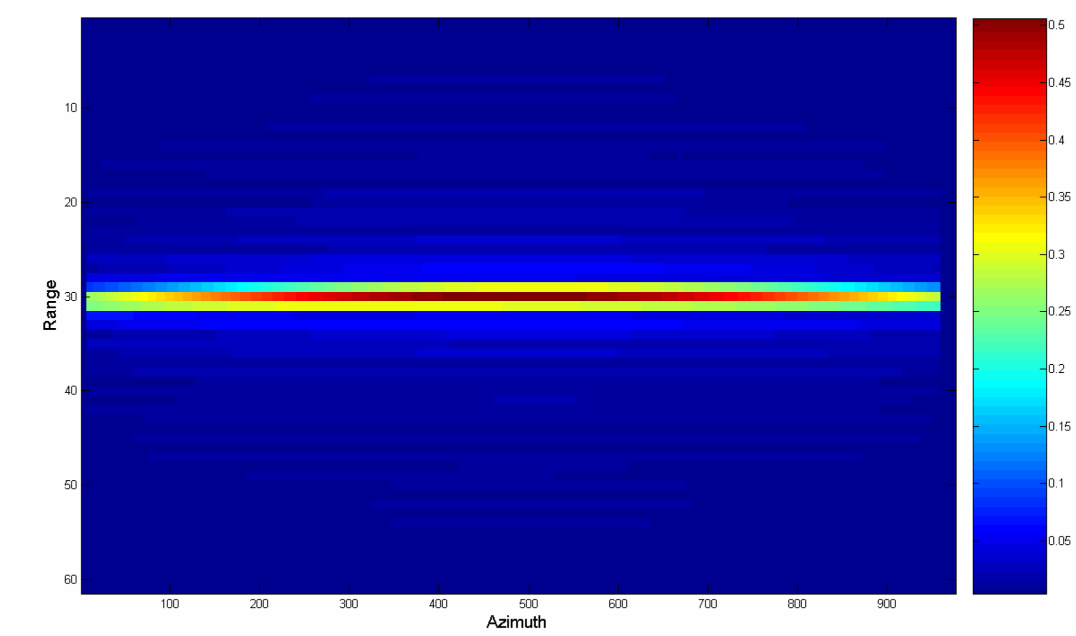

Fig.2.7 Zoom of range compressed data of the scatterer

Fig. 2.8 shows the results obtained from the azimuth compression; the compressed signal is the typical bi-dimensional sinc function which characterizes the compressed SAR response.

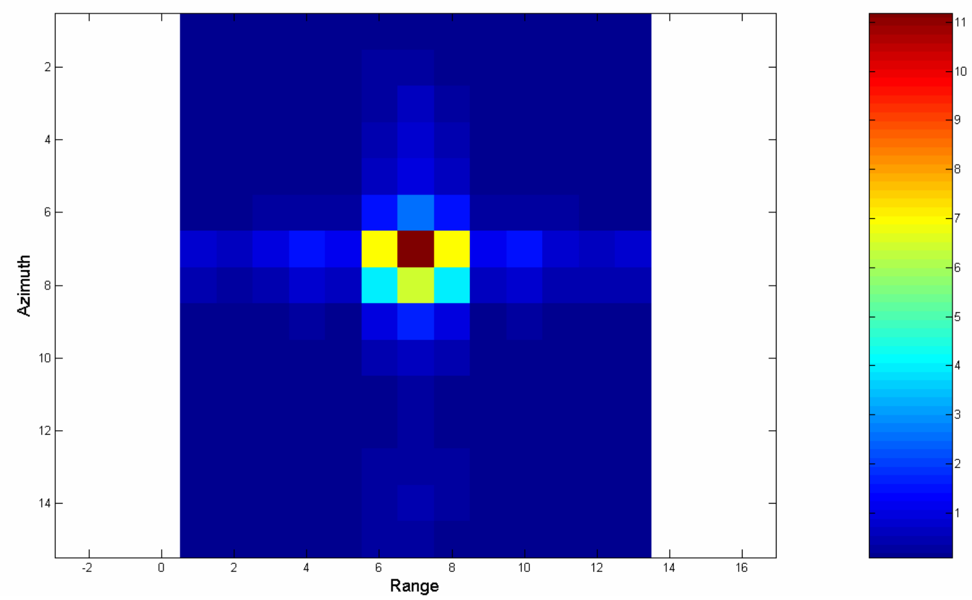

Fig.2.8 Focused scatterer after the azimuth compression

2.5 GENERATION OF RAW DATA OF A MOVING TARGET ON A STATIONARY BACKGROUND

The raw data simulator is used to generate a stationary scene in which is inserted a moving target.

The amplitude of the background is modelled with different distribution, depending on the simulated background type. The phase of each pixel depends on the acquisition geometric modality of the SAR and on the impressed velocity vector of the pixel.

Fig.2.9 and 2.10 shows the amplitude and phase of the raw data of a scene composed by a stationary background with some strong scatterers and a moving target.

Especially for the phase image, we can observe that every pixel influences the phase of the other pixel; in fact, Fig. 2.10 and 2.11 (which represents a zoom of the scatterer phase) stresses this effect, observing the distortion of the iso-phase curves.

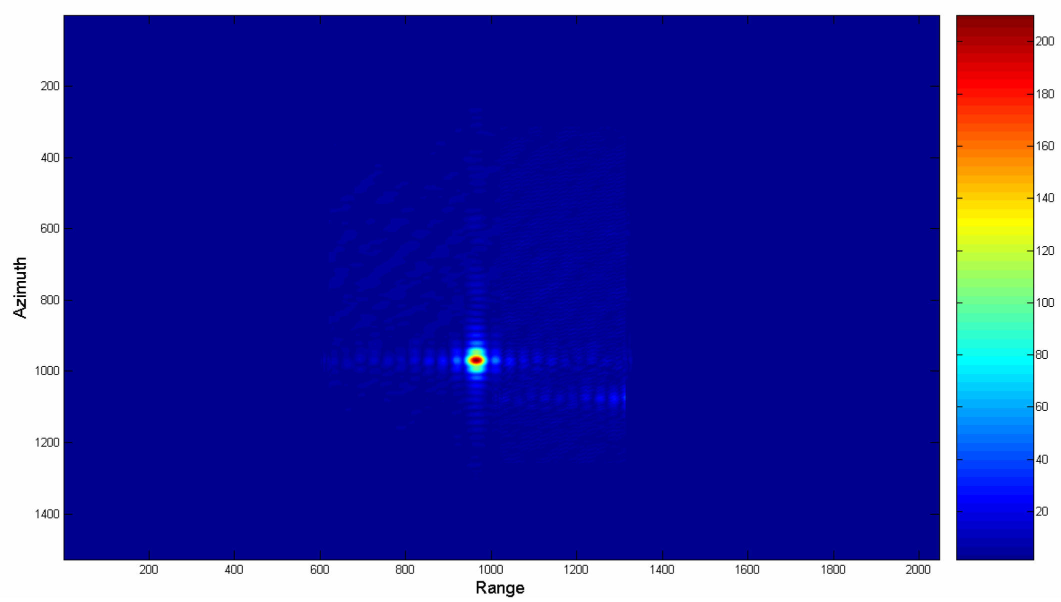

Fig.2.9 Raw data amplitude of a simulated complex scene

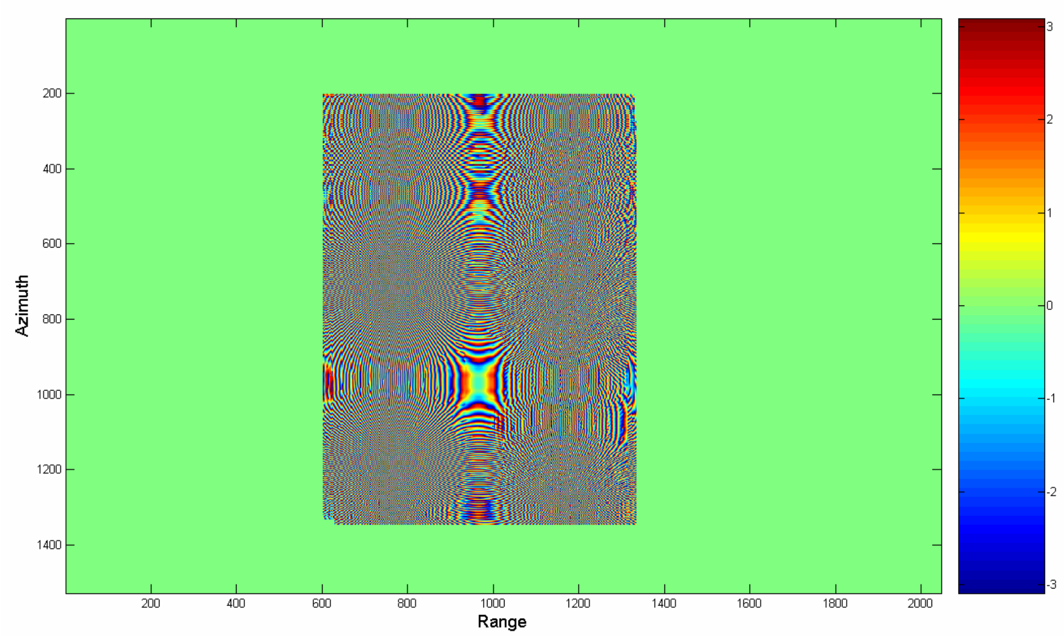

Fig.2.10 Raw data phase of a simulated complex scene

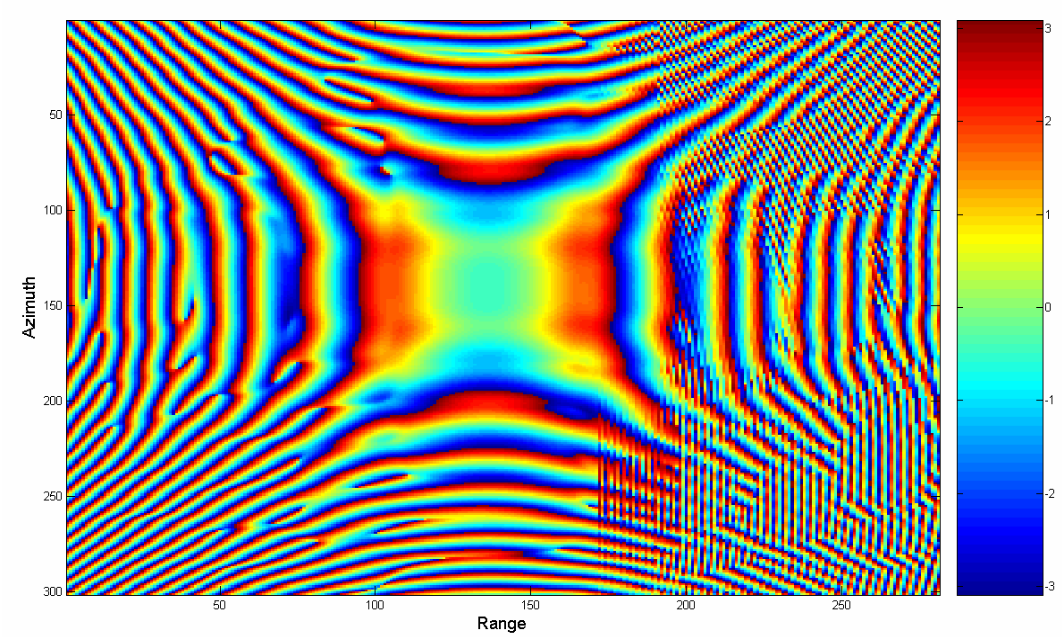

Fig.2.11 Zoom of the raw data phase of a strong pointform scatterer in the simulated complex scene

For illustration purposes only we propose a comparison with the raw data of a real scene of an ERS-2 acquisition, with orbit 16466 and frame 2763: the interesting area is centered on Anzio (Italy).

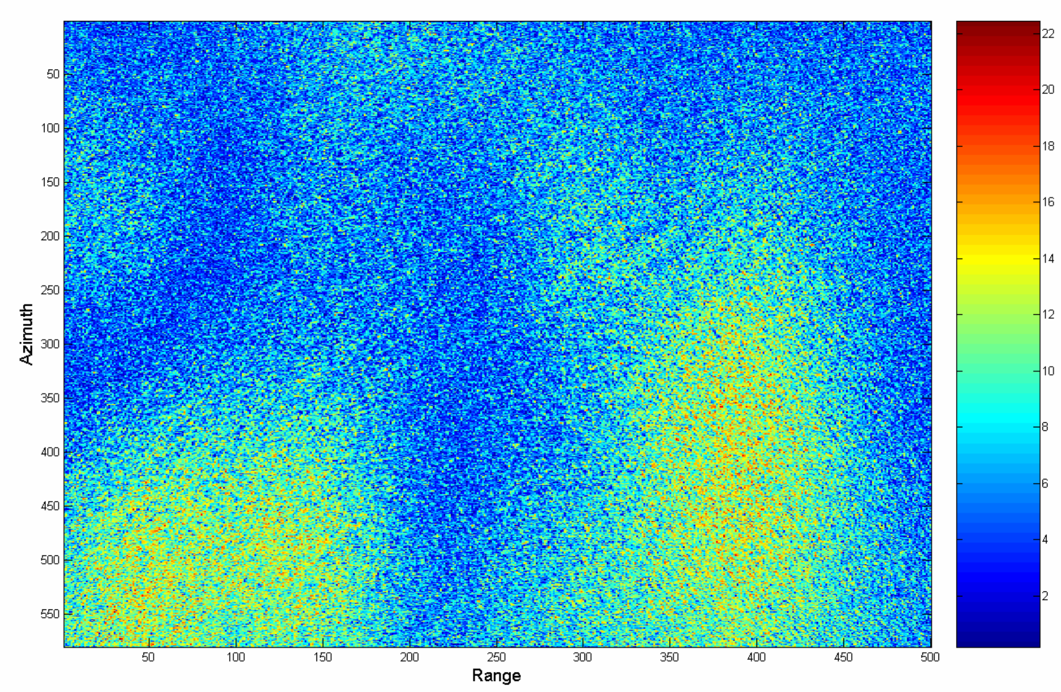

Fig.2.12 Raw data amplitude of a pointform scatterer on an extended scene

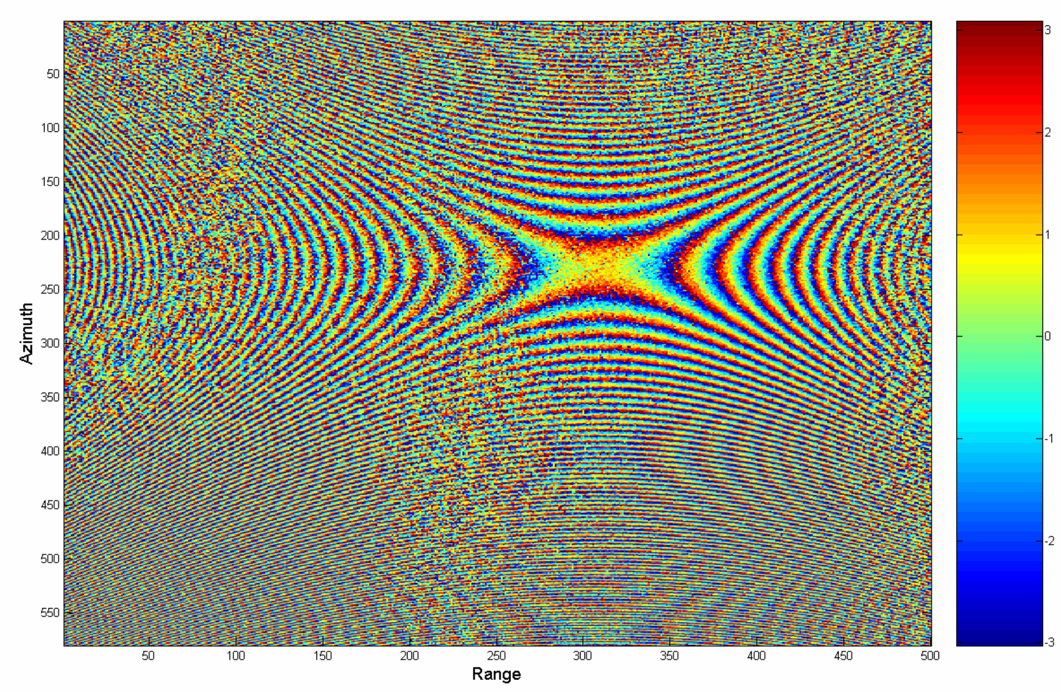

Fig.2.13 Raw data phase of a pointform scatterer on an extended scene

REFERENCES

[1] J.C. Curlander, R. McDonough, ”Synthetic Aperture Radar, Systems and Signal Processing”, Wiley 1991.

[2] I.G. Cumming, F.H. Wong, ” Digital Signal Processing of Synthetic Aperture Radar Data: Algorithms and Implementation”, Artech House January 2005.

[3] Mehrdad Soumekh, ” Synthetic Aperture Radar Signal Processing with MATLAB Algorithms”, Hardcover, April 1999.

CHAPTER 3

A VELOCITY VECTOR ESTIMATION ALGORITHM FROM DUAL-CHANNEL SAR RAW DATA

3.1. INTRODUCTION

In recent years many efforts have been devoted to enhancing the content and quality of space borne SAR products and several methods of data processing have been developed and implemented. One of the SAR applications that has raised considerable interest is the monitoring of moving targets on the surface, so that the design of some forthcoming space missions also takes into account the capability of characterizing the dynamics of moving objects against a still background.

The advantages to have multi-channel SAR systems for Ground Moving Target Indication (GMTI) techniques for surveillance aim has motivated some space agencies to design many space missions; even if the multi-channel SAR systems require very high cost of the hardware and produce a big data rates, recently many multi-channel SAR mission, such as some dedicated airplane missions [1] and the satellite missions TerraSAR-X and RADARSAT 2, was planned and realized, as [2], [3], [4]. Particularly, TerraSAR-X and Radarsat 2 have the possibility to split the antenna in two antennas to allow the dual-channel use.

The increasing interest to monitor the moving targets on the ground has permitted the development of many Moving Target Indication (MTI) techniques, such as Along Track Interferometry (ATI) and Displaced Phase Centre Antenna (DPCA); different techniques are considered to estimate the single components of the velocity vector.

When the target moves in the radial or in the along-track direction, the estimate of its velocity can be straightforwardly carried out by one of the developed methods. However, for a generic velocity vector, the independent estimate of each component is not optimal, since the value retrieved for one component affects the estimate of the other [5].

Hence, a retrieval scheme which recursively estimates the two components of the velocity vector can yield more accurate results.

In this chapter is proposed a velocity retrieval algorithm that estimates the full velocity vector without *a-priori* information by coupled processing of range and azimuth responses towards improved accuracy.

In the final section the algorithm is validated using the SAR raw data simulator.

3.2 TYPICAL VELOCITY ESTIMATION TECHNIQUES

Some recently published techniques try to estimate the linear and quadratic part of the phase signal by choosing the motion parameters that fit well the phase of the target and approximate this estimation to the range and azimuth component, assuming that they are independent, which is not a correct assumption [6].

The proposed solutions to estimate the motion parameters can be separated into two classes: multi-channel and single channel.

For the azimuth velocity estimation in a multi-channel SAR system Doppler rate filters select the velocity that better focuses the target [7]; for the range velocity estimation typical techniques are based on the Doppler shift induced by the moving targets, and the Along Track Interferometry [8], that exploits the phase information of the hermitian product between the two channels. Another popular type of estimation algorithm is called Space Time Adaptive Processing algorithms (STAP) [9], which requires an array of antennas.

For a single channel the situation is more complicated. The proposed algorithms are few, due to the technical difficulties that result for the detection and velocity estimation of moving objects.

For the azimuth velocity estimation a recently proposed technique uses matching criteria on the displacement vector obtained from the spatial shift of the moving target from sub-apertures [10]. An another solution is to use a bank of matched filter to select the wrong velocity ([6],[7]).

For the range velocity estimation a recently proposed technique uses sub-apertures images, applying a maximum-likelihood criterion to estimate the linear range migration correction to the looks spectrum of the range compressed data [11]. Other recently proposed techniques use a maximum-likelihood criterion to estimate the motion parameters of the target in the spatial frequency domain [12], or computing the skew of the bi-dimensional spectral signature of the moving object [13]; some works are oriented for a time-frequency analysis, that represents the signal data in terms of time and frequency and gives information about the phase of the targets [14].

3.3 USED VELOCITY ESTIMATION TECHNIQUES

In this work we use two techniques to estimate the velocity components.
To estimate the azimuth velocity v_{az} an azimuth velocity filter bank is used. Each filter focuses all the objects that move with the velocity selected by the filter, maximizing the moving target response.
To estimate the range velocity v_{rg} the ATI (Along Track Interferometry) is considered, using the data of a dual-channel SAR.

3.3.1 AZIMUTH VELOCITY FILTER BANK

To estimate the azimuth velocity, the raw data are focused using the bank of azimuth filters; the velocity is selected choosing the filter that best matches the correct speed.
To decide a selection criterion, we must extract the parameters sensitive to the azimuth velocity that characterize the IRF.
The typical parameters that characterize the IRF are the mainlobe amplitude and the spatial resolution.
We consider a target that has an azimuth velocity of 7 m/s; every velocity filter compresses in azimuth the data of the target with a phase function of the selected velocity. The scanned interval of the azimuth velocity is [0, 10 m/s], with a filter separation of 1 m/s.
The velocity is estimated maximizating the peak amplitude and the azimuth resolution; the results are shown in Fig.3.1 and 3.2 for the two parameters.

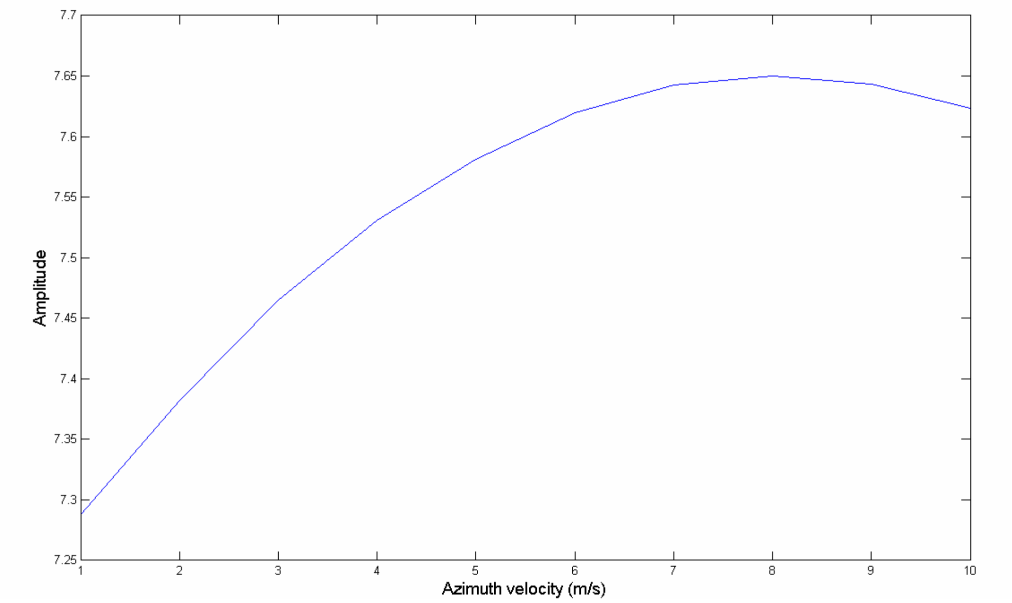

Fig.3.1 Output of the velocity filters: amplitude peak variation

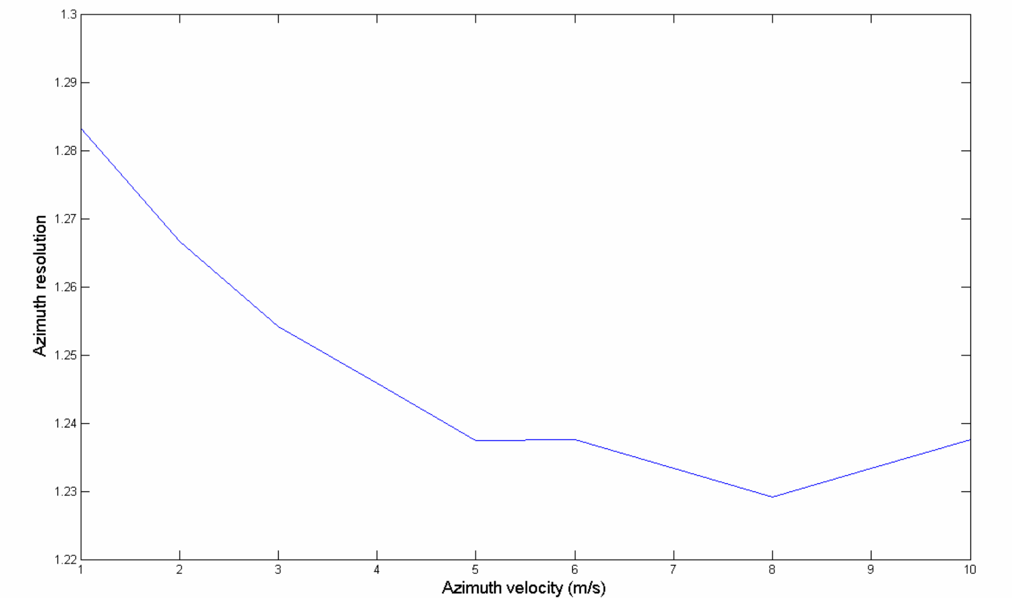

Fig.3.2 Output of the velocity filters: azimuth resolution variation

To improve the sensitivity to the velocity and to optimize all the informative content use all the available information, we consider the ratio between azimuth resolution and peak amplitude. The velocity selection criterion is based on the minimization of the ratio parameter.

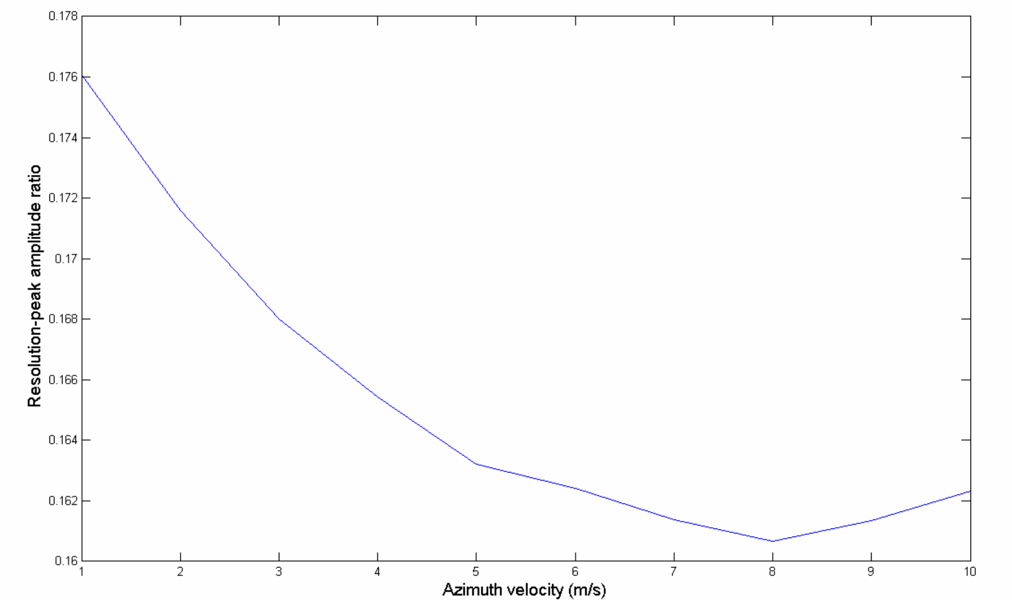

Fig.3.3 Output of the velocity filters: resolution-peak amplitude ratio variation

Another selection criterion is considered.

The IRF profile is compared with the IRF profile of a reference stationary target; the parameter used in the estimation is the correlation between the two IRF.

The selection criterion chooses the filter that maximizes the correlation coefficient between the IRF of the moving target and the IRF of reference.

Fig.3.4 shows a comparison between the azimuth profiles of the reference IRF and the target IRF in the stationary case; Fig. 3.5 shows the effects of the azimuth velocity.

In the two case the correlation coefficient si respectively of 0.9999 and 0.7798.

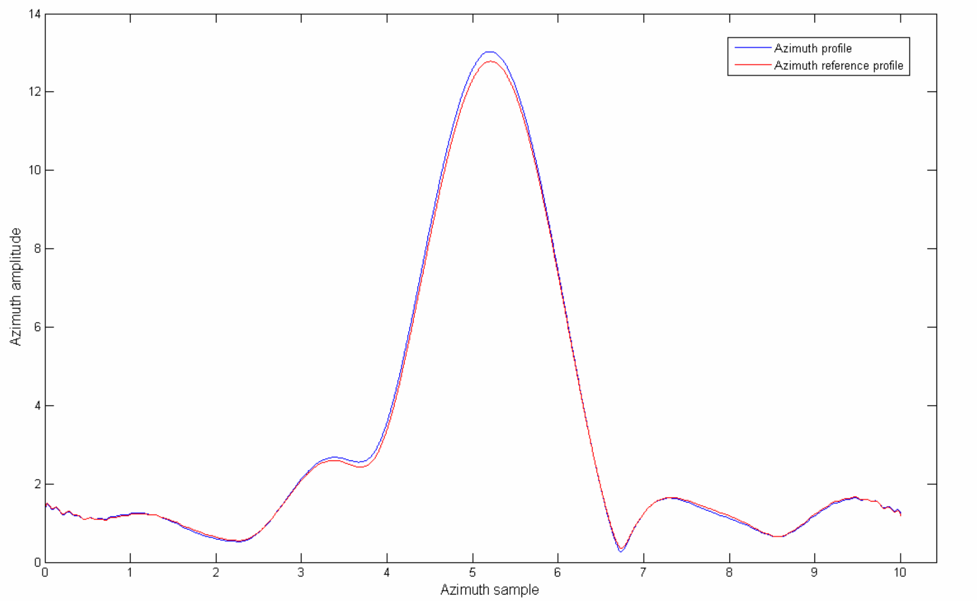

Fig.3.4 Comparison between the reference IRF and the IRF of a stationary target

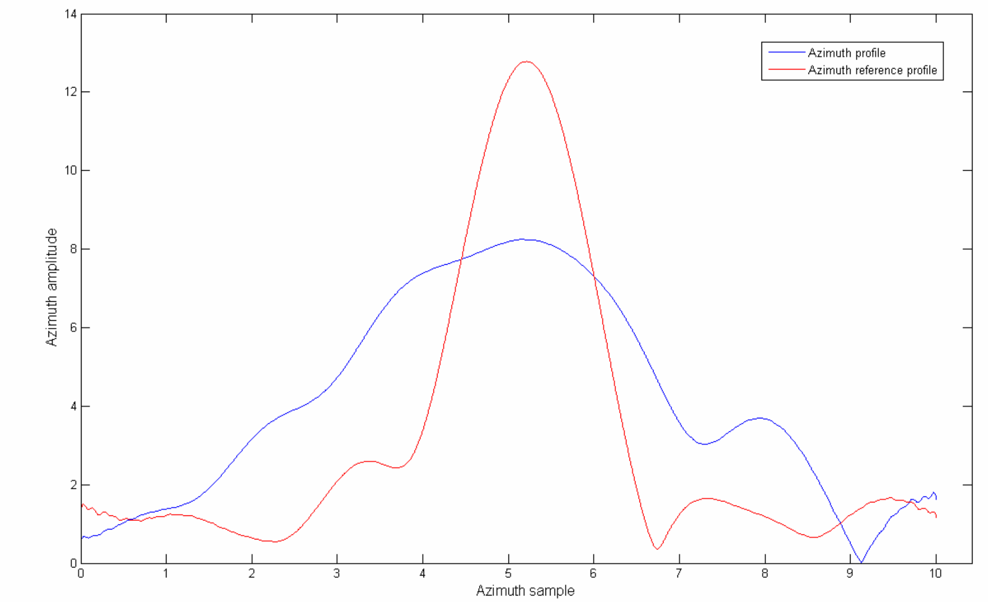

Fig. 3.5 Comparison between the reference IRF and the IRF of a target with azimuth velocity of 20 m/s

If the target is in a complex background, the problem is the difficulty of the wrong reconstruction of the signal. So the azimuth profile of the signal of the moving target is rounded as a Gaussian profile.

To surpass the problem, we propose the following solutions.

1) The azimuth profile is rounded to the Gaussian function that is better correlated with the reference signal reconstruction; the criterion chooses the filter that maximizes the correlation coefficient between the IRF of the moving target and the reference IRF.
2) The azimuth profile is rounded to a quadratic polynomial that fit better the signal reconstruction; the selection criterion chooses the filter that maximizes the correlation coefficient between the IRF of the moving target and the IRF of reference.

3.3.2 ALONG TRACK INTERFEROMETRY

To estimate the range velocity, the ATI (Along Track Interferometry) technique is used. The ATI is an emerging technique, which is using in many different applications to generate velocity map of the object on ground.

The ATI-SAR systems are based on two antennas along the track direction, separated from a spatial baseline $2 \cdot B_{ATI}$, as shown in Fig.3.6.

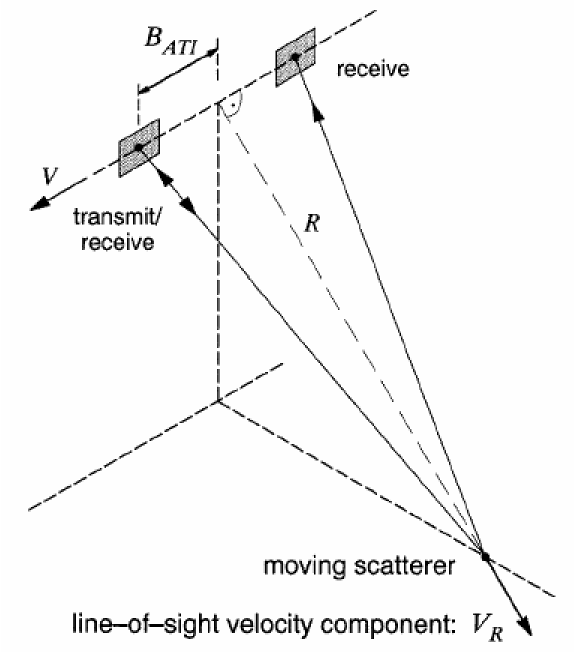

Fig.3.6 ATI-SAR system

In the ATI system two images are acquired in identical geometric conditions. The acquisitions are separated from a temporal baseline $\Delta\eta = \frac{B_{ATI}}{V_{sat}}$.

The ATI signal is computed by multiplying the signal from one channel by the complex conjugate of the second channel; the interferometric phase difference is processed to measure the radial velocity of the observed surface [15].

Given two co-registered signals $s_1(\eta,t)$ and $s_2(\eta,t)$, depending on the azimuth time η and range time *t*, the ATI signal results:

$$ATI = s_1(\eta,t)s_2^*(\eta,t) = |s_1(\eta,t)||s_2(\eta,t)| \cdot \exp\left(j\left[\varphi_1(\eta,t) - \varphi_2(\eta,t)\right]\right). \qquad (3.1)$$

The ATI phase depends linearly on the slant range velocity of the scatterer v_{sr} [16]:

$$\Phi(\eta,t) = \varphi_1(\eta,t) - \varphi_2(\eta,t) =$$

$$\frac{4\pi}{\lambda}\frac{B_{ATI}v_{sr}}{V_{sat}} + \frac{2\pi}{\lambda}B_{ATI}\left(\frac{1}{V_{sat}} + \frac{v_{az}-V_{sat}}{V_{st}^2}\right)\Delta v_{sr} - \frac{2\pi}{\lambda}\frac{v_{az}B_{ATI}}{R_0}\eta_c \qquad (3.2)$$

Where Δv_{sr} is the mismatching of the linear term of range equation.

The first term is the useful informative content, depending linearly to the slant range velocity. The second term is negligible, because $\left. v_{az} - V_{sat} \middle/ V_{st}^2 \right. \approx -\left. 1 \middle/ V_{sat} \right.$. The third term is the error of ATI estimation, depending on frequency carrier, v_{az}, η_c and R_0.

The estimation errors on the ATI phase are caused by an un-symmetrical target trajectory around the broadside time, by non-symmetries caused by the RCS variation during the integration time (i.e.: for the changing of aspect angle) and by a not compensation of the azimuth velocity.

3.4 VELOCITY ESTIMATION ALGORITHM

As one can see from the slant range model, the azimuth velocity of the target appears only in the quadratic term of the formula, while the range velocity is present in the linear and in the quadratic term:

$$R_{mov}(\eta) \approx a + b\left(v_{rg}\right)\eta + c\left(v_{rg}, v_{az}\right)\eta^2 . \tag{3.3}$$

We remember that a mismatching in the linear term causes an azimuth displacement, a range defocusing and a range decreasing amplitude; a mismatching in the quadratic term causes a spreading of the signal energy in azimuth, so the moving target is smeared: the effects are the azimuth defocusing and a big azimuth decreasing amplitude.

Because the presented techniques estimate the linear and the quadratic terms separately, the quadratic term c of (3.3) is function of the two velocity components.

It is necessary to develop an retrieval algorithm for the velocity vector extraction.

The proposed algorithm requires a dual-channel antenna in ATI mode [6].

The algorithm is divided in 3 steep.

1° STEEP

The azimuth velocity $v_{az}^{'}$ is estimated with a bank of azimuth matched filters centered on the zero, analyzing the Impulse Response Function (IRF) of the moving target, in order that all the space of the velocity is covered. So we used different filters to compress in azimuth, every of these focuses only the target with the velocity selected from the filter: the velocity is selected from the filter that maximizes the ratio between the azimuth resolution and the mainlobe amplitude of the IRF.

To process the range compressed data we used the filter bank centered on the stationary matched filter:

$$h_{az}^{-1}\left(\eta,\Delta v_{az}\left|\eta_c,R_0\right.\right)=\exp\left\{j\frac{4\pi}{\lambda}\cdot\frac{\left(\Delta v_{az}-V_{sat}\right)^2}{2R_0}\eta^2\right\}, \tag{3.4}$$

where Δv_{az} varies between the interval $\Delta v_{az}\in\left[-v_{az}^{\max},+v_{az}^{\max}\right]$.

This first method allows only an indicative estimation.

2° STEEP

Taking in account $v_{az}^{'}$, the two images generated by the dual-channel SAR are processed to obtain the along track interferometric phase; the ATI technique is used to estimate the range velocity $v_{rg}^{'}$.

Note that the ATI phase is not applicable without compensate partially the azimuth velocity, because the ATI phase is very sensitive to the SCR (Signal to Clutter Ratio); if the energy is smeared, the ATI signal can be under the noise threshold [17].

To process the range compressed data we used the matched filter

$$h_{az}^{-1}\left(\eta,v_{az}^{'}\left|\eta_c,R_0\right.\right)=\exp\left\{j\frac{4\pi}{\lambda}\cdot\frac{\left(v_{az}^{'}-V_{sat}\right)^2}{2R_0}\eta^2\right\}. \tag{3.5}$$

We improve the estimation using a bank of azimuth filters, that take in account the estimated azimuth velocity and the range velocity, so to obtain the velocity v_{rg}; the bank of matching filters is centered around to $v_{rg}^{'}$ and scans the space to have higher precision.

The used matched filter is:

$$h_{az}^{-1}\left(\eta,v_{rg}^{'},v_{az}\left|\eta_c,R_0\right.\right)=\exp\left\{j\frac{4\pi}{\lambda}\left[\frac{y_0v_{rg}^{'}}{R_0}\eta+\frac{1}{2R_0}\left(\left(v_{az}^{'}-V_{sat}\right)^2+v_{rg}^{'\,2}\left(1-\frac{y_0^2}{R_0^2}\right)\right)\eta^2\right]\right\}. \tag{3.6}$$

The azimuth velocity v_{az} is estimated again with a bank of filters centred around the estimated range and azimuth velocity v_{rg} and $v_{az}^{'}$, where the filters select more close velocity.

The used matched filter is the following.

$$\begin{aligned}&h_{az}^{-1}\left(\eta,v_{rg},v_{az}\left|\eta_c,R_0\right.\right)=\\&=\exp\left\{j\frac{4\pi}{\lambda}\left[\frac{y_0v_{rg}}{R_0}\eta+\frac{1}{2R_0}\left(\left(\Delta v_{az}+v_{az}^{'}-V_{sat}\right)^2+v_{rg}^2\left(1-\frac{y_0^2}{R_0^2}\right)\right)\eta^2\right]\right\}\cdot\end{aligned} \tag{3.7}$$

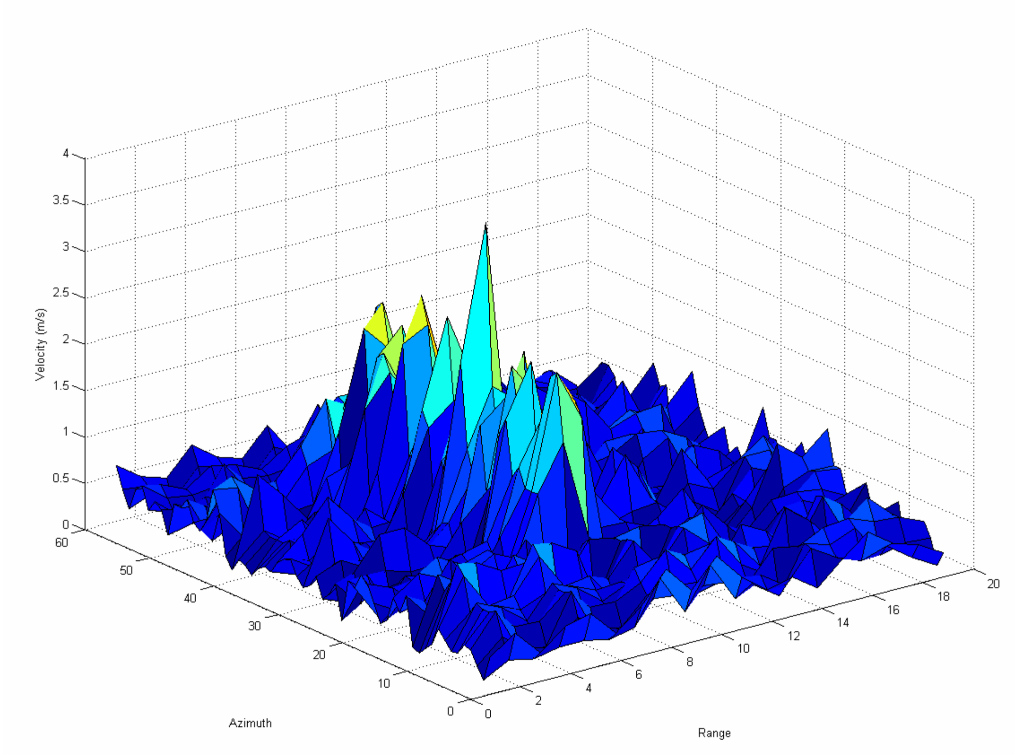

Fig.3.7 Example of moving target ATI phase

3° STEEP

For the azimuth velocity estimation at the third steep we used the correlation method with the reference profile. In fact the correlation method results more sensitive to little velocity variation: so it resulted better to select the right velocity for a little separation of the filters.

Finally the algorithm chooses the filter that maximizes the correlation coefficient between the azimuth profile of the moving target IRF, rounded to the Gaussian function, and the reference profile.

3.5 ALGORITHM VALIDATION WITH SIMULATOR

To validate the estimation algorithm, a dual-channel split-antenna SAR raw data simulator is implemented.

Generally, the principal difficulty of the velocity estimation methods are related to the noise, because often the targets are in a complex background that can cover the signal;

so, to assess the validity of the estimation algorithm different backgrounds are generated to simulate some possible application scenarios.

To obtain a significant statistics and to verify the stability of the estimation we chose four velocity vectors, varied the range and azimuth velocities within a small interval and calculated the mean value of the estimation error and the standard deviation of the single velocity component, by varying the other.

3.5.1 PARAMETER SETTING

The simulator generates raw data with characteristics of the SAR on board of ERS satellites.

Given the general availability of ERS SAR images, for the time being the simulator has been designed to generate the raw data provided by this instrument. The values of the relevant system parameters and corresponding symbols that we used are listed in Tab 3.1. Table 3.2 reports the ranges of velocities spanned by the bank of filters and their separation in each of the 3 steps mentioned above. In steps 2) and 3), the filter separation is a fraction of the estimated velocity.

TAB. 3.1

Used parameters values and symbols

Parameter	**Symbol**	**Value**
Frequency rate of linear FM waveform	K	0.418 MHz/μs
Frequency carrier	f_c	5,3 GHz
Pulse time	τ	37,12μs
Pulse bandwith	B	15,55 MHz
Pulse Repetition Frequency	PRF	1679.9Hz
Satellite velocity	V_{sat}	7500 m/s
Satellite height	H	790 km
Slant range at the broadside	R_0	827 Km
Elevation angle	θ	23°
Baseline	D	10 m
Processed Doppler bandwith	B_D	1378 Hz
Doppler centroid	f_{Dc}	260 Hz
Doppler rate	f_R	-2434 Hz/s
Slant range resolution	Δsr	10 m
Azimuth resolution	Δaz	5 m

TAB. 3.2

STEEP	**INTERVAL SCANNED**	**SEPARATION OF FILTER**
1° steep	[-38.5m/s,38.5m/s]	5.5 m/s
2° steep	$[-0{,}25\cdot v_{rg},+0{,}25\cdot v_{rg}]$	$0{,}05\cdot v_{rg}$
3°steep	$[-0{,}24\cdot v_{az}^{'},+0{,}24\cdot v_{az}^{'}]$	$0{,}04\cdot v_{az}^{'}$

Summarizing the steeps of the algorithm:

1° steep: The azimuth velocity selected from the interval [-38.5 m/s, +38.5 m/s], the matched filters are separate from 5.5 m/s.

2° steep: After the estimation with ATI, the filters scan the interval of [-24%, +24%] of the estimation around the range velocity estimated with ATI; the matched filters are separate from 8% of the velocity estimation.

3° steep: The filters scan the interval of [-25%, +25%] of the estimation around the azimuth velocity estimated with ATI, the matched filters are separate from 5% of the estimation.

3.5.2 BACKGROUND STATISTICS

To simulate different scenarios, it is necessary to characterize every environment from the statistic point of view.

As simple case, the first generated reference background has constant backscattering intensity, assuming a Signal-to-Clutter Ratio (SCR) of 30 dB.

The second generated background simulates a sea environment, intended for an application to ship traffic monitoring. To select a plausible scenario, we consider the sea scenario with wind of 5 m/s: in this case, the background is characterized by a mean backscattering coefficient of -18 dB [18], with the 88% of values in the interval [-2 dB, +2 dB].

For the target, we consider a constant value of 0 dB, even if the contras between ship and sea varies with the wind speed, the incidence angle, the wave conditions and the presence of ocean features: so the mean SCR is 18 dB.

To model the sea background statistics, we chosen the lognormal and gamma distribution ([19],[20]).

Fig. 3.8 and 3.9 show the amplitude image of the simulated sea scene in two and three dimensions respectively, with a lognormal distribution.

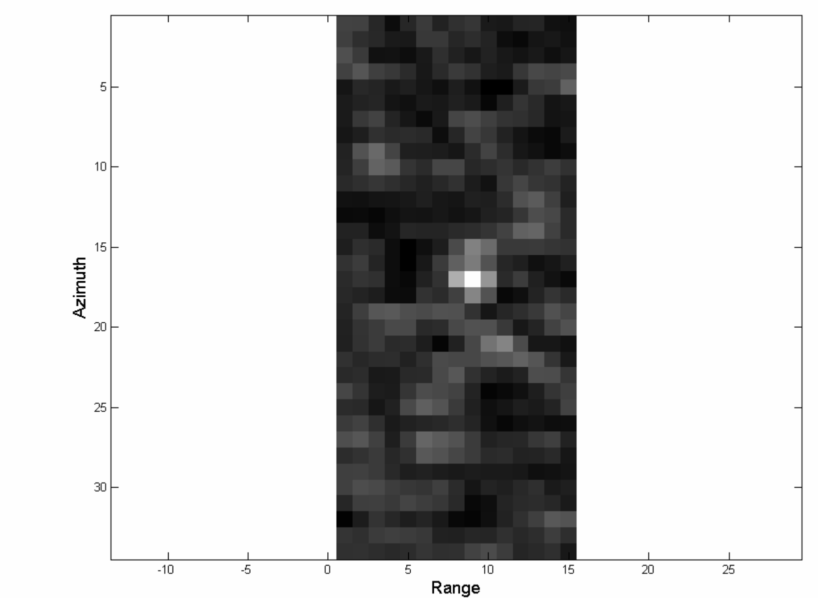

Fig.3.8 2D amplitude image of the simulated sea scene

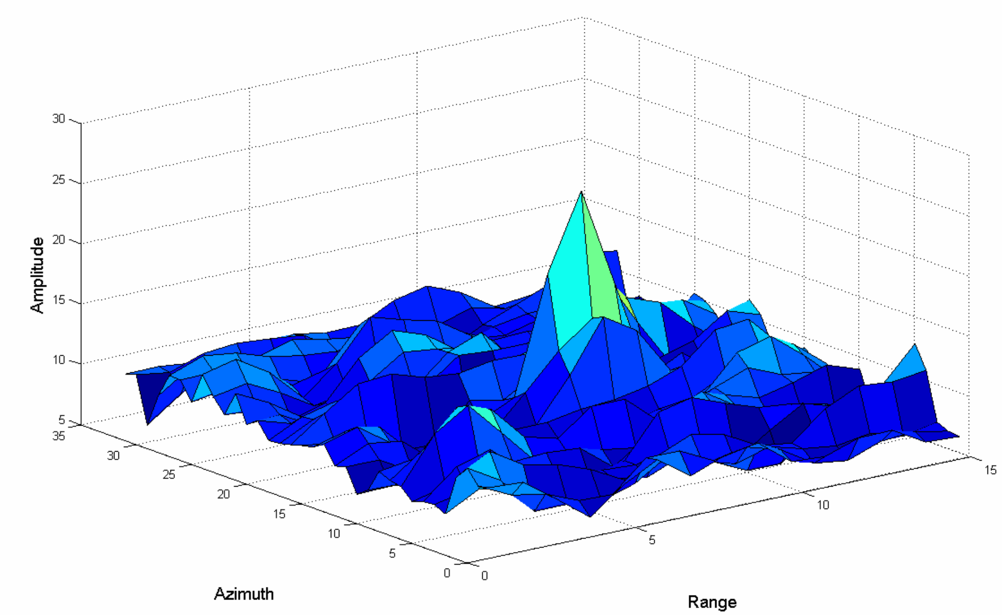

Fig.3.9 3D amplitude image of the simulated sea scene

Finally, a land vehicle in shrubs is simulated to study the behaviour of the algorithm in vehicle traffic monitoring. To model the shrubs background statistic, we have chosen the Rayleigh distributions, with a mean backscattering coefficient of -8.4 dB and a standard deviation of 3.1 dB [21].

The backscattering of the target depends strongly on the polarization of the transmitted wave, the frequency, the car type and the aspect angle: for a SAR system in C band in VV polarization the RCS varies between 15dB and -20 dB. We selected a mean SCR of 9 dB [21].

Fig. 3.10 and 3.11 show the amplitude image of the simulated shrubs scene in 2 and 3 dimension respectively with a Rayleigh distribution.

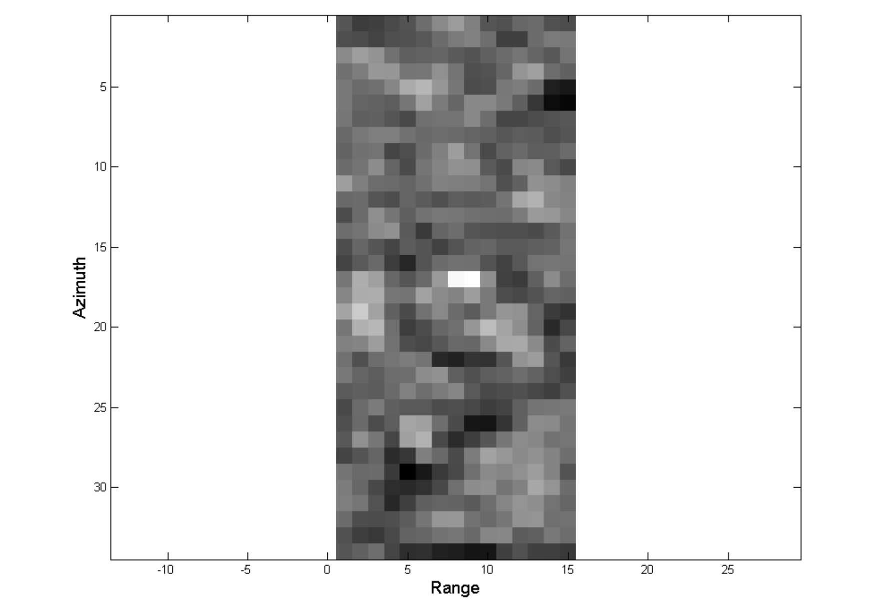

Fig.3.10 2D amplitude image of the simulated shrubs scene

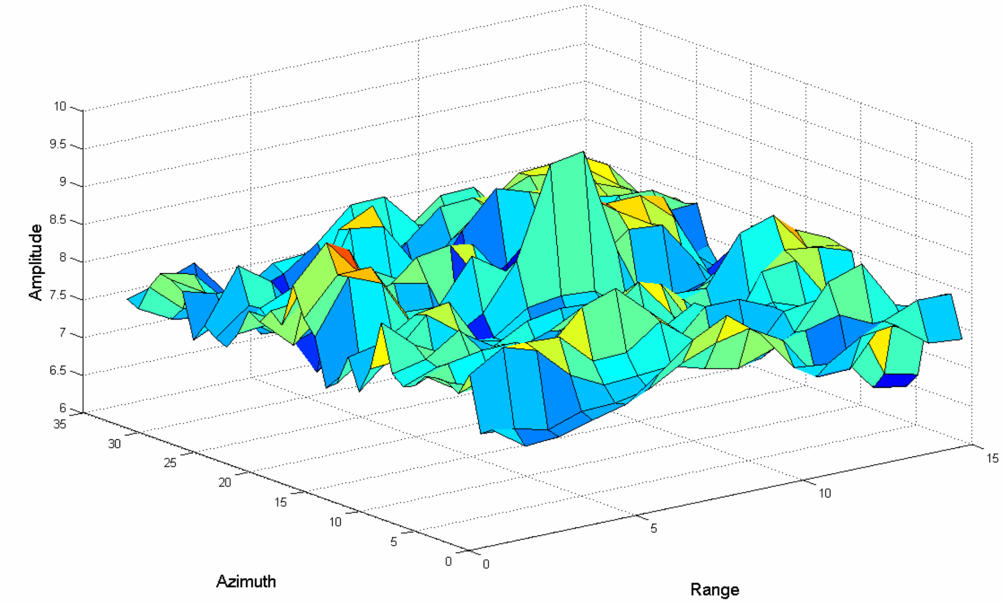

Fig.3.11 3D amplitude image of the simulated shrubs scene

3.5.3 RESULTS

To assess the validity of the estimation algorithm, different backgrounds are generated to simulate some possible application scenarios.

To obtain a significant statistics and to verify the stability of the estimation we chose four velocity vectors, varied the range and azimuth velocities within a small interval and calculated the mean value of the estimation error and the standard deviation of the single velocity component, by varying the other.

The four velocity vectors are the following:

TAB. 3.3

Used velocity vectors

Vector Number	**Range velocity**	**Azimuth velocity**
1	5.1 m/s	8.2 m/s
2	10.2 m/s	16.5 m/s
3	15.4 m/s	24.7 m/s
4	20.7 m/s	33 m/s

The algorithm is tested on the different background; the first scenario is the ideal scenario, with constant backscattering intensity and SCR of 30 dB.

The second scenario is a sea scene, with a mean SCR of 18 dB.

Finally, a shrubs scenario is simulated to study the behaviour of the algorithm in vehicle traffic monitoring, with a mean SCR of 9.0 dB.

The results are presented in TAB 3.4, TAB 3.5 and TAB 3.6.

TAB. 3.4

Result for the background with constant backscattering

Vector number	**Range error mean (%)**	**Azimuth error mean (%)**	**Range standard deviation (m/s)**	**Azimuth standard deviation (m/s)**
1	7.1	18.4	0.1	0.9
2	6.3	2.7	0.1	1.5
3	6.8	7.7	0.1	2.5
4	6	12.3	0.1	4.1

TAB. 3.5

Result for the sea background

Vector number	**Range error mean (%)**	**Azimuth error mean (%)**	**Range standard deviation (m/s)**	**Azimuth Standard deviation (m/s)**
1	13.5	9.7	0.3	3.2
2	23.4	13.8	0.6	3.5
3	24.8	19.6	0.3	2.9
4	26	6.3	0.1	3.6

TAB. 3.6

Result for the shrubs background

Vector number	**Range error mean (%)**	**Azimuth error mean (%)**	**Range standard deviation (m/s)**	**Azimuth standard deviation (m/s)**
1	61.9	30.7	0.4	8.3
2	14.8	20.9	1	2.7
3	29	20	0.4	8.6
4	34.5	28.5	10.2	8.8

From the tables showed, it results that the estimation of the azimuth component is more affected by the range velocity, while the estimation of this latter is rather stable.

The last case (TAB 3.6) points out the difficulty of the estimation, given the low SCR and the background complexity. Indeed, a low SCR is detrimental to the estimation of the interferometric phase (in agreement with that of [22]), hence to the reconstruction of the azimuth profile of the target image, resulting in a high estimation error.

Finally a comparison with results obtained by the retrieval algorithm and the separated application of the estimation methods for the two components is presented in TAB. 3.7, 3.8 and 3.9.

TAB. 3.7

Estimation comparison for the background with constant backscattering

Real velocity vector		**Estimate error with algorithm**		**Estimate error without algorithm**	
Range	*Azimuth*	*Range*	*Azimuth*	*Range*	*Azimuth*
5.1 m/s	8.2 m/s	-8.8%	20%	13.7%	35%
10.2 m/s	16.5 m/s	-4%	-5.5%	9.7%	5%
15.4 m/s	24.7 m/s	4.3%	-5%	15.3%	5%
20.7 m/s	33 m/s	-4.7%	-2.5%	6.1%	8.7%

TAB. 3.8

Estimation comparison for the sea background

Real velocity vector		**Estimate error with algorithm**		**Estimate error without algorithm**	
Range	*Azimuth*	*Range*	*Azimuth*	*Range*	*Azimuth*
5.1 m/s	8.2 m/s	-7.3%	14%	-9.2%	35%
10.2 m/s	16.5 m/s	-23.9%	3.5%	9.7%	5%
15.4 m/s	24.7 m/s	4.8%	0%	15.3%	5%
20.7 m/s	33 m/s	-4%	-6.3%	6.1%	8.7%

TAB. 3.9

Estimation comparison for the shrubs background

Real velocity vector		**Estimate error with algorithm**		**Estimate error without algorithm**	
Range	*Azimuth*	*Range*	*Azimuth*	*Range*	*Azimuth*
5.1 m/s	8.2 m/s	-38.8%	-10%	-49.8%	20%
10.2 m/s	16.5 m/s	-6.5%	12.5%	-73.4%	27.5%
15.4 m/s	24.7 m/s	-23.1%	-16%	-73.3%	-10%
20.7 m/s	33 m/s	-3.2%	-25%	100%	-40%

3.6 CONCLUSIONS

Several methods have been developed to measure the velocity components of moving targets imaged by SAR. The algorithm described in this contribution estimates the velocity vector without *a-priori* information by coupled processing of range and azimuth responses towards improved accuracy. As expected, the performance of the retrieval scheme degrades with decreasing SCR, especially when the target moves against a complex background.

We must do some consideration about the obtained results.

The retrieval algorithm could be used also with a single SAR, where one can use a sub-aperture mode to focus two images separated in azimuth of a temporal baseline; this give the possibility of an extension use of the algorithm also with the present SAR systems. In this point of view, we simulated the parameters characteristic of the ERS system with the intent to apply the algorithm on single channel. The algorithm starts from a disadvantageous situation: the MTI applications require high resolution and high SCR, while the performance of ERS is not fit for this aim; moreover, the ATI suffers low SCR.

The validation of the algorithm with dual-channel SAR is expected to provide valuable data to test the method in real environments.

In the next chapter we propose the extension for a single-antenna SAR in a split-aperture mode.

REFERENCES

[1] E.Chapin, C.W.Chen, “Preliminary Results from an Airborne Experiment Using Along-Track Interferometry for GMTI”, Radar Conference, 2005 IEEE International, Pag.343-347, 9-12 May 2005.

[2] J. H. G. Ender, P. Berens, A. R. Brenner, L. Rossing, U. Skupin, “Multi-channel SAR/MTI system development at FGAN: from AER to PAMIR”, Proceedings of the IEEE Int. Geoscience Remote Sensing Symposium, IGARSS, 24-28 June 2002

[3] S. Ochs, W. Pitz, “The TerraSAR-X and TanDEM-X Satellites”, Recent Advances in Space Technologies, 3rd International Conference on, RAST, pp. 294-298, 14-16 June 2007.

[4] M Gabele, I. Sikaneta, “A new method to create a virtual third antenna from a two channel SAR-GMTI system”, Waveform Diversity and Design Conference, International Conference on, pp. 433-437, 4-8 June 2007.

[5] J.J.Sharma, C.H.Gierull, M.J.Collins, “The influence of Target Acceleration on Velocity Estimation in Dual-Channel SAR-GMTI”, IEEE Transactions on Geoscience and Remote Sensing, Vol. 44 , N. 1, pp. 134–147, Jan 2006.

[6] A. Radius, D. Solimini, “A velocity vector estimation algorithm tested on simulated SAR raw data”, Proceedings of the IEEE Int. Geoscience Remote Sensing Symposium, IGARSS, 23-27 July 2007.

[7] S.Hinz, F.Meyer, A.Laika, R.Bamler, “Spaceborne traffic monitoring with Dual Channel Synthetic Aperture Radar – Theory and Experiments”, Proceedings of the IEEE, Computer Society Conference on, CVPR 2005, Vol.3, pp. 7-7, 20-26 June 2005.

[8] J.J.Sharma, C.H.Gierull, M.J.Collins, “The influence of Target Acceleration on Velocity Estimation in Dual-Channel SAR-GMTI”, IEEE Transactions on Geoscience and Remote Sensing, Vol. 44 , N. 1, pp. 134–147, Jan 2006.

[9] J. H.G. Ender, “Space-Time Adaptive Processing for Synthetic Aperture Radar”, IEE Colloquium on Space-Time Adaptive Processing (Ref. No. 1998/241), pp. 6/1-618, April 1998.

[10] M. Kirscht, “Detection and velocity estimation of moving objects in a sequence of single-look SAR images”, Proceedings of the IEEE Int. Geoscience Remote Sensing Symposium, IGARSS, Vol. 1, pp. 333-335, 27-31 May 1996.

[11] M. Kirscht, “Detection and imaging of arbitrarily moving targets with single-channel SAR”, Proceedings of the IEE Radar, Sonar and Navigation, Vol. 150, Issue 1, pp. 7-11, February 2003.

[12] J. M. B. Dias, P. A. C. Marques, “Multiple moving target detection and trajectory estimation using a single SAR sensor”, IEEE Transactions on Aerospace and Electronic Systems, Vol. 39, Issue 2, pp. 604–624, April 2003.

[13] P. A. C. Marques, J. M. B. Dias, “Velocity estimation of fast moving targets using a single SAR sensor”, IEEE Transactions on Aerospace and Electronic Systems, Vol. 41, Issue 1, pp. 75–89, January 2005.

[14] S.Barbarossa, A.Farina, “Detection and imaging of moving objects with synthetic aperture radar. 2. Joint time-frequency analysis by Wigner-Ville distribution”, Proceedings of the IEE Radar and Signal Processing, Vol. 139, Issue 1, pp. 89-97, Feb. 1992.

[15] R. Bamler, P. Hartl, “Synthetic Aperture Radar Interferometry”, DLR, Issue 4, pp. R1-R54, August 1998.

[16] C.H.Gierull, “Ground Moving Target parameter estimation for two-channel SAR”, Proceedings of the IEE Radar, Sonar and Navigation, Vol. 153, Issue 3, pp. 224-233, June 2006

[17] S.Chiu, C.H.Gierull, A.Durak, “Clutter effects on ground moving targets' interferometric phase”, Proceedings of the IEEE Int. Geoscience Remote Sensing Symposium, IGARSS, Vol.2, Pag. 2928-2931, 25-29 July 2005.

[18] A.K. Fung, K.K. Lee., “A semi-empirical sea-spectrum model for scattering coefficient estimation”, IEEE Journal of Oceanic Engineering, Vol. OE-7, NO. 4, pp. 166 – 176, October 1982.

[19] C.J. Oliver, “Representation of radar sea clutter”, Proceedings of the IEE Radar and Signal Processing, Vol. 135, Issue 6, pp. 497-500, December 1988.

[20] F.T. Ullaby, M.C..Dobson, “Handbook of Radar Scattering Statistics for Terrain”, Artech House 1989.

[21] G.Palubinskas, H. Runge, P. Reinartz, “Radar signatures of road vehicles”, Proceedings of the IEEE Int. Geoscience Remote Sensing Symposium, IGARSS, Vol.2, Pag. 1498-1501, 20-24 September 2004.

CHAPTER 4

FROM TWO CHANNELS TO SINGLE CHANNEL SAR

4.1 INTRODUCTION

Although in the last years many techniques for moving target indication (MTI) were developed for multi-channel SAR systems, there are only a very small number of platforms with multi-channel capability. Furthermore, for civil applications only single channel data is typically made available.

It is well known that the velocity estimation with a single channel is a challenging problem having several limitations. To take the most out of this kind of data it is necessary to use all of its informative content.

This chapter proposes a sub-aperture processing and analyzes the information about the radial velocity of a target obtained from two channel synthesized by splitting the synthetic aperture of a single channel SAR.

The velocity estimation methodology considers the possibility to apply the ATI techniques to symmetrical looks. The interpretation key is, similar to that of [1], that each sub-aperture has a different time center, so each generated image will have a different reference time.

4.2 SYMMETRICAL SUB-APERTURE TECHNIQUE TO GENERATE LOOKS IN ATI MODE

As shown in Chapter 3, the radial velocity is obtained using the ATI technique with a two-channel SAR system, formed from two antennas in the flight direction separated from a spatial baseline. The 2-channel SAR system generates two images $I_F(\eta, R)$ (*fore-looking*) and $I_A(\eta, R)$ (*aft-looking*). The interferometric phase is related to the radial velocity.

To obtained better results without ambiguity it is possibile to use multi-channel ATI-SAR with more of two antennas. The problem is that there are very few SAR systems with more than a single antenna because of the complexity and the immense data rates produced by a multi-channel system; the few existing are almost all military systems, that use velocity estimation algorithm know as STAP (Space Time Adaptive Processing) [2]. For this reason, it is important to work on single-channel SAR data.

We try to apply the ATI technique to symmetrical sub-apertures images obtained splitting the synthetic aperture. Operating with the TDC algorithm, it is possible to simulate two antennas along the flight track.

For each look a dedicated processing is operated: the sub-aperture images are obtained with the azimuth compression in the time domain of partially overlapped synthetic aperture parts of the integration time, as shown in Fig.4.1.

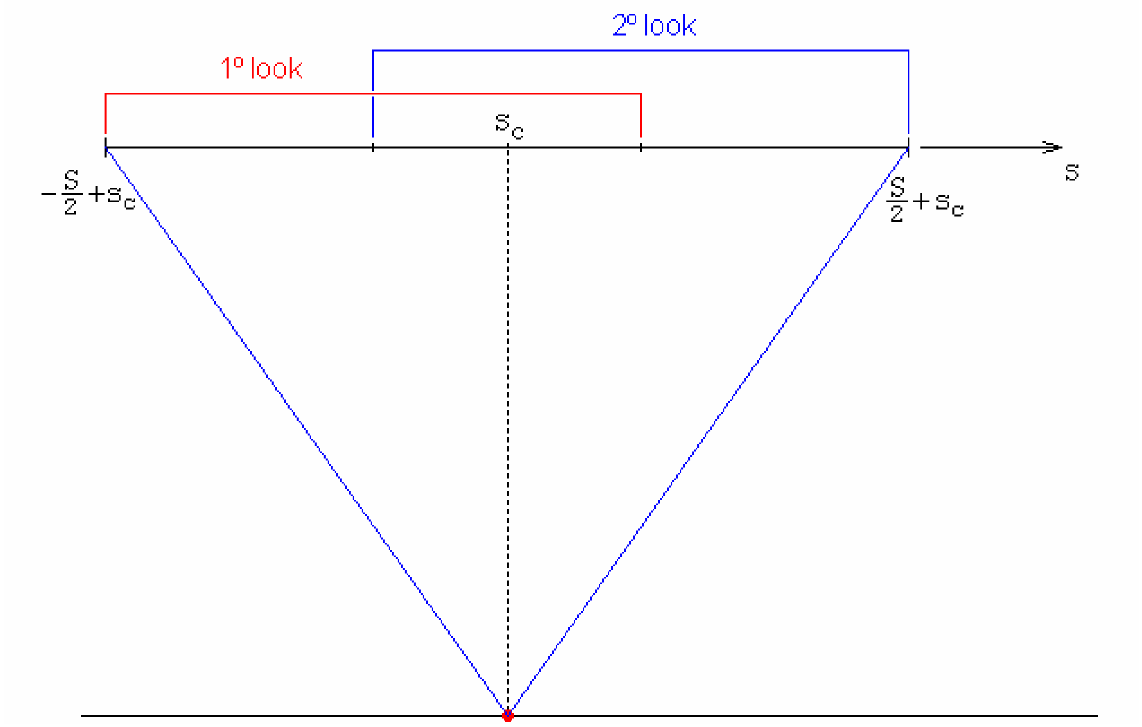

Fig.4.1 Sub-aperture method to split the full aperture in two looks in ATI mode.

If the two looks are formed with the same matching filter, it is necessary to consider an opportune corrective factor during the azimuth compression, to take in account the delay time between the images [3].

As an alternative, each aperture is multiplied for the phase factor in the frequency domain [4]:

$$\exp\left(j\pi \frac{f_{Dc}(f_{Dci}-f_{Dc})}{f_R} \right), \tag{4.1}$$

where f_{Dci} is the Doppler centroid of the i th look.

We chosen to operate the splitted processing of the two images using two matched filter *ad hoc* for each.

Before to operate the azimuth compression, we pre-filter the range compressed data in the time domain using a FIR filter [4].

This pre-processing phase is necessary because the received signal from the backscattering of a transmitted pulse is formed by all contributes inside of the antenna footprint: the filtering isolates the components backscattered only inside the antenna footprint of the sub-aperture.

In the following, the phases of the sub-aperture processing are shown..

4.2.1 PRE-FILTERING

A method to design a FIR filter is the known "window method", in which the impulse response of the filter is obtained ending the ideal impulse response with infinite length of time.

The ideal Band pass filter is a rectangular window in the frequency domain; applying the window method, the coefficients of a FIR filter with length N are [5]:

$$\begin{cases} h(n) = \dfrac{\omega_c}{\pi f_s}, & n = 0 \\ h(n) = \dfrac{1}{\pi n}\mathrm{sen}\left(\dfrac{\mathrm{n}\omega_c}{f_s}\right), & n \neq 0 \end{cases}, \quad -\frac{N-1}{2} \leq n \leq \frac{N-1}{2}, \tag{4.2}$$

where ω_c is the cut-off frequency and f_s the sampling frequency.

Remembering the relation

$$\omega_c = 2\pi f_c, \tag{4.3}$$

the coefficients are:

$$h(n) = \frac{1}{\pi n}\mathrm{sen}\left(\frac{\mathrm{n}\omega_c}{f_s}\right) = \frac{1}{\pi n}\mathrm{sen}\left(\frac{\mathrm{n}2\pi f_c}{f_s}\right)\cdot\frac{2f_c/f_s}{2f_c/f_s} = \frac{2f_c}{f_s}\cdot\mathrm{sinc}\left(\frac{\pi n\cdot 2f_c}{f_s}\right). \tag{4.4}$$

Because $2f_c = B$ is the filter passing band, (4.4) results:

$$h(n) = \frac{B}{f_s}\cdot\mathrm{sinc}\left(\frac{\pi n\cdot B}{f_s}\right). \tag{4.5}$$

To reduce the Gibbs phenomenon and to avoid discontinuity at the extreme of the filter, a weigh function is used:

$$w(n) = 0{,}54 - 0{,}46 \cdot \cos\left(\frac{\pi n}{N_{centro}}\right), \tag{4.6}$$

where $N_{centro} = {}^{N-1}\!/_{2}$.

Finally, to take in account that the filter is centered on a non zero frequency f_0, a phase term must be considered:

$$\exp\left[j2\pi f_0\left(\frac{n}{f_s}\right)\right]. \tag{4.7}$$

The expression of a band pass FIR filter in the time domain wit rectangular window with band B, sampling frequency f_s and central frequency f_0 is:

$$h_D(n) = \frac{B}{f_s} \cdot \mathrm{sinc}\left(\frac{\pi n \cdot B}{f_s}\right) \cdot \left[0{,}54 - 0{,}46 \cdot \cos\left(\frac{\pi n}{N_{centro}}\right)\right] \cdot \exp\left[j2\pi f_0\left(\frac{n}{f_s}\right)\right]. \tag{4.8}$$

To operate the filtering in the time domain, the azimuth convolution between filter and range compressed data is computed. Being the signal sampled in azimuth with the frequency PRF and having the looks a Doppler band B_{D_look} (that is a fraction of the total band), the filter are:

$$\begin{gathered} h_D(n) = \frac{B_{D\_look}}{PRF} \cdot \mathrm{sinc}\left(\frac{\pi n \cdot B_{D\_look}}{PRF}\right) \cdot \\ \cdot \left[0{,}54 - 0{,}46 \cdot \cos\left(\frac{\pi n}{N_{centro}}\right)\right] \cdot \exp\left[j2\pi f_{Dci}\left(\frac{n}{PRF}\right)\right] \end{gathered}, \text{ i=1,2.} \tag{4.9}$$

4.2.2 AZIMUTH COMPRESSION OF THE SUB-APERTURES

Remembering that the azimuth SAR signal is a chirp signal frequency-moduled, the relation time-frequency is:

$$\eta - \eta_c = \frac{1}{f_R} f_D, \tag{4.10}$$

The Doppler frequency is:

$$f_D = f_R(\eta - \eta_c). \tag{4.11}$$

In the zero-Doppler processing, the Doppler centroid of the full synthetic aperture is zero, but the Doppler centroid of the two sub-apertures is different from zero, as shown in Fig.4.2.

The Doppler rate f_R is the same for each look, because the processed Doppler band does not change.

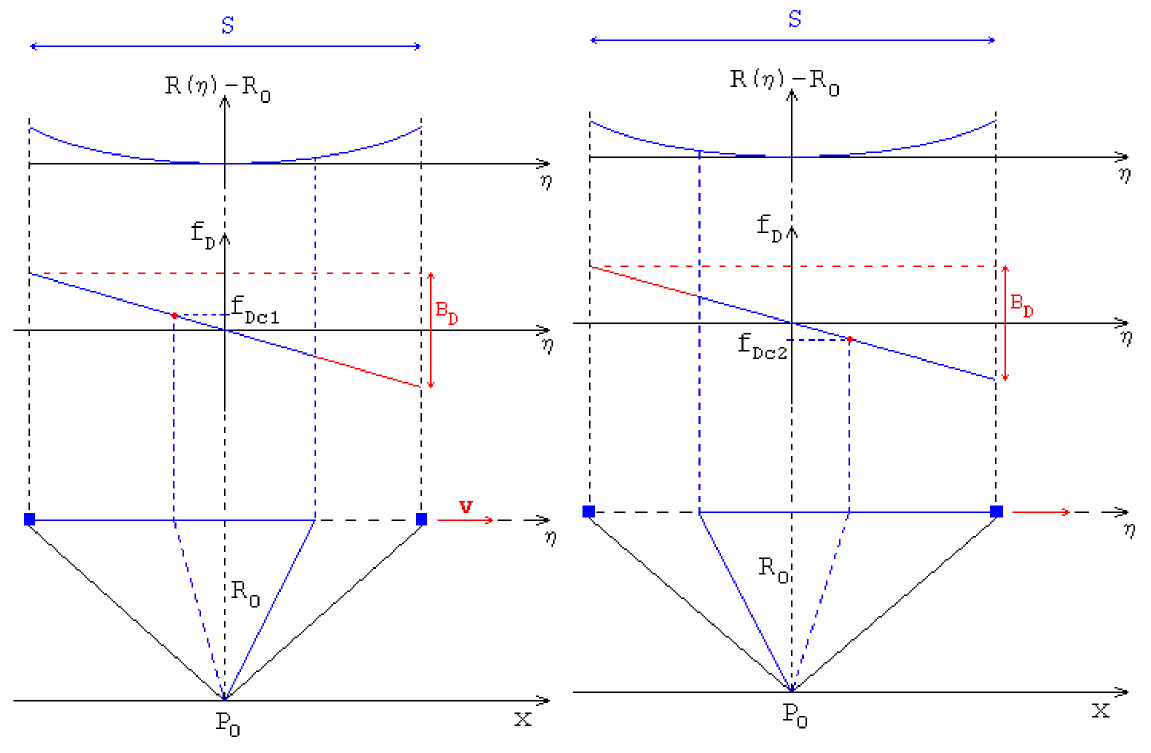

Fig.4.2 Range migration and Doppler centroid for the sub-apertures.

With reference to Fig. 4.2, the Doppler centroid is obtained as following. For the bounds the time-frequency relation results:

$$\pm\frac{S}{2} = \mp\frac{1}{f_R}\cdot\frac{B_D}{2} \quad \text{for} \quad \eta = \pm\frac{S}{2} + \eta_c . \tag{4.12}$$

Generally, remembering the relation

$$f_D = f_R(\eta - \eta_c). \tag{4.13}$$

The Doppler centroid for the sub-apertures results:

$$\begin{cases} f_{Dc1} = f_R \cdot \left(\dfrac{\eta_{ap}}{2}\cdot S - \dfrac{S}{2}\right) \\ f_{Dc2} = -f_R \cdot \left(\dfrac{\eta_{ap}}{2}\cdot S - \dfrac{S}{2}\right) = -f_{Dc1} \end{cases}, \tag{4.14}$$

where $0 < \eta_{ap} < 1$ represented the global aperture fraction used to synthesize the looks.

The azimuth compression is obtained, correlating the filtering range compressed data of the two sub-apertures with the azimuth reference function matched to the two looks:

$$h_{az_i}^{-1}\left(\eta|\eta_c,R_c\right)=\exp\left\{-j2\pi\left[f_{Dci}\eta+\frac{f_R\eta^2}{2}\right]\right\}, \tag{4.15}$$

where i indicates the number of look (i=1,2).

Choosing the dedicate matched filters for the sub-apertures, the correlation peak after the azimuth compression is localized at the time η_c, and the images are co-registered.

4.2.3 BASELINE SELECTION

The selection of the baseline is not easy: in fact, we must take in account the physical tie-up on the parameter; a very little value makes the Doppler estimate very sensitive to the clutter, a very big value makes the coherence coefficient of the images very low [6].

In [7] the typical values of the temporal distance $\Delta\eta=\frac{B_{ATI}}{V_{sat}}$ are proposed; these values are in the interval [10, 100 ms].

The application selection imposes other bonds, because the non-ambiguity interval increases when the baseline decreases, as shown in the following.

Remembering that radial velocity is related with the ATI phase from the expression:

$$V_R=\left(\frac{\lambda}{4\pi}\right)\cdot\frac{\Phi}{\Delta\eta}, \tag{4.16}$$

the non-ambiguous maximum velocity is:

$$V_R=\left(\frac{\lambda}{4\pi}\right)\cdot\frac{2\pi}{\Delta\eta}=\frac{\lambda}{2}\cdot\frac{1}{\Delta\eta}. \tag{4.17}$$

Note that the (4.16) is obtained from the first term of (3.2), neglecting the error terms.

As shown in (4.17), the non-ambiguous maximum velocity is function of the SAR frequency and of the temporal baseline.

4.3 INVESTIGATION ON THE CAPABILITY OF SYMMETRICAL SUB-APERTURE IMAGES TO ESTIMATE THE RADIAL VELOCITY

We defined the methodology to split in two symmetric sub-aperture images the full synthetic aperture. It is necessary analyze the possibility to apply the ATI technique to the two looks for radial velocity estimation.

This analysis is presented in the following paragraphs [8], developing from the mathematical point of view the effects of the target motion on the SAR compressed response function in phase and amplitude.

4.3.1 BASIC SAR PROCESSING

The most popular SAR processing algorithms are based on the matched filtering theory [5]. Tipically, there are two approaches: i) in the time domain, ii) in the frequency domain.

As in the chapter 1 we consider the first approach, using the so-called Time Domain Correlation algorithm [5].

This algorithm compresses the SAR raw data operating two separated correlations, in range and in azimuth, in the time domain. We resume shortly the basic SAR processing from the mathematical point of view.

The algorithm is divided into 3 major steps:

1) Range compression;
2) Range migration compensation;
3) Azimuth compression for every pixel in the time domain.

Let *s* be the azimuth time and s_c the temporal azimuth center of the synthetic aperture of a stationary point scatterer; *t* is the slant range time and t_c the slant range time relative to s_c. The range compressed data expression of a stationary scatterer in temporal coordinates is described in the bi-dimensional temporal plane by [4]:

$$\hat{g}(s,t) = B\exp\left(-j4\pi\frac{R(s)}{\lambda}\right)\cdot\text{sinc}\left\{\pi B\left[t\text{-}2\frac{R(s)}{\text{c}}\right]\right\}, \tag{4.18}$$

with $|s-s_c| \le \frac{S}{2}$, where *S* is the integration time.

If the synthetic aperture is small enough, when compared with the distance to the target, we can expand R(s) in Taylor series around s_c [4]:

$$R(s) = R_c - \lambda\frac{f_{Dc}}{2}(s-s_c) - \lambda\frac{f_R}{2}\frac{(s-s_c)^2}{2}, \tag{4.19}$$

where the Doppler parameters are space-variant, depending on s_c and R_c.

The relation between time and frequency is illustrated in Fig. 4.3, where at the top there is the graphic representation of the slant range and at the bottom there is the corresponding Doppler frequency. Note that at the center of the synthetic aperture the Doppler frequency is not zero because of the Earth rotation, the orbit ellipticity and the squint angle of the antenna, so the parabola is not symmetrical with the respect to s_c.

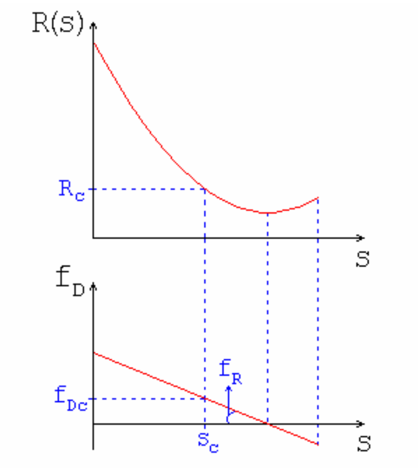

Fig. 4.3 Relation between the slant range and the Doppler parameters

The range compressed data becomes:

$$\hat{g}(s,t) = Bz_c \exp\left\{ j2\pi \left[f_{Dc}(s-s_c) + f_R \frac{(s-s_c)^2}{2} \right] \right\} \cdot$$
$$\cdot \text{sinc}\left\{ \pi B \left[t\text{-}\frac{2}{\text{c}} \left(R_c - \lambda \frac{f_{Dc}}{2}(s-s_c) - \lambda \frac{f_R}{2} \frac{(s-s_c)^2}{2} \right) \right] \right\}, \quad (4.20)$$

where

$$z_c = \exp\left(-j \frac{4\pi R_c}{\lambda} \right). \quad (4.21)$$

The slant range time is function of the azimuth time and of the generic slant range $R_c^{'}$:

$$t(s,R_c^{'}) = \frac{2R(s)}{c} = \frac{2}{c}\left(R_c^{'} - \lambda \frac{f_{Dc}}{2}(s-s_c) - \lambda \frac{f_R}{2} \frac{(s-s_c)^2}{2} \right). \quad (4.22)$$

The range migration compensation operation aims at choosing time *t*, starting from the estimation of R(s), to take in account the slant range time dependence. For every target, the range migration compensation generates the mono-dimensional range compressed vector along the target trajectory, because we are interested in analyzing the behaviour of the moving scatterer at the coordinates (s_c, R_c).

For $t = t(s, R_c^{'} = R_c)$ the dependence on the range variable in (4.22) is removed.

The azimuth compression of the pixel with coordinates $(s_c^{'}, R_c)$ is calculated from the correlation:

$$\zeta(s_c'|s_c,R_c)=\int_{s_c-S/2}^{s_c+S/2}\hat{g}(s\,|\,s_c,R_c)\cdot h_{az}^{-1}(s-s_c'\,|\,s_c,R_c)ds\,, \tag{4.23}$$

where the reference function is

$$\begin{aligned}h_{az}^{-1}\left(s-s_c^{'}\,|s_c,R_c\right)&=\exp\left\{j\frac{4\pi}{\lambda}\left[R(s)-R_c\right]\right\}=\\&=\exp\left\{-j2\pi\left[f_{Dc}(s-s_c^{'})+f_R\frac{(s-s_c^{'})^2}{2}\right]\right\}\end{aligned}. \tag{4.24}$$

For $t=t(s,R_c^{'}=R_c)$ eq. (4.23) results:

$$\begin{aligned}\zeta(s_c'|s_c,R_c)=&\int_{s_c-S/2}^{s_c+S/2}Bz_c\cdot\exp\left\{j2\pi\left[f_{Dc}(s-s_c)+f_R\frac{(s-s_c)^2}{2}\right]\right\}\cdot\\&\cdot\exp\left\{-j2\pi\left[f_{Dc}(s-s_c')+f_R\frac{(s-s_c')^2}{2}\right]\right\}ds\end{aligned}. \tag{4.25}$$

If the target moves in the range direction, this generates an additional linear phase term, depending on the slant range velocity $v_{sr}=v_{rg}\cdot sen(\vartheta)$, and the effect is that the Doppler history changes in the azimuth time:

$$R_{mov}(s)=R_c-\lambda\frac{(f_{Dc}-v_{sr})}{2}(s-s_c)-\lambda\frac{f_R}{2}\frac{(s-s_c)^2}{2}\,. \tag{4.26}$$

In fact, the range velocity causes a small mismatching of the quadratic term of the history Doppler [9]. Herein we do not consider it since the effect is negligible.
Starting from range compressed data

$$\hat{g}(s,t)=B\exp\left(-j4\pi\frac{R_{mov}(s)}{\lambda}\right)\cdot\mathrm{sinc}\left\{\pi B\left[t\text{-}2\frac{R_{mov}(s)}{\mathrm{c}}\right]\right\}, \tag{4.27}$$

after the range migration compensation computed for a stationary target, we obtain:

$$\begin{aligned}\hat{g}(s|R_c)&=B\exp\left(-j4\pi\frac{R_{mov}(s)}{\lambda}\right)\cdot\mathrm{sinc}\left\{\frac{2\pi B}{c}\left[R(s)\text{-}R_{mov}(s)\right]\right\}=\\&=Bz_c\exp\left\{j2\pi\left[(f_{Dc}-v_{sr})(s-s_c)+f_R\frac{(s-s_c)^2}{2}\right]\right\}\mathrm{sinc}\left\{\frac{2\pi B}{c}\left[-\frac{\lambda v_{sr}}{2}(s-s_c)\right]\right\}\end{aligned}, \tag{4.28}$$

and eq. (4.23) becomes:

$$\begin{aligned}\zeta(s_c'|s_c,R_c)=&\int_{s_c-S/2}^{s_c+S/2}B\exp\left(-j\frac{4\pi R_c}{\lambda}\right)\mathrm{sinc}\left\{\frac{2\pi B}{c}\left[-\frac{\lambda v_{sr}}{2}(s-s_c)\right]\right\}\cdot\\ &\cdot\exp\left\{j2\pi\left[(f_{Dc}-v_{sr})(s-s_c)+f_R\frac{(s-s_c)^2}{2}\right]\right\}\cdot\\ &\cdot\exp\left\{-j2\pi\left[f_{Dc}(s-s_c')+f_R\frac{(s-s_c')^2}{2}\right]\right\}ds\end{aligned}\qquad .\qquad (4.29)$$

4.3.2 SINGLE SAR VERSUS MULTI-CHANNEL SYSTEMS

This section compares a two-channel SAR and a single channel SAR splitted in two sub-apertures to obtain 2 channels. The difference is the key to understand the theoretical results proposed in 4.3.3.

1) A two-channel SAR, in ATI configuration, is composed of two antennas separated from a spatial baseline in the flight direction. The antennas acquire two sets of data each with a different time centers s_{ci}.

If the target moves in the range direction, the temporal difference corresponds to a shift of the slant range centers R_{ci}. The co-registration operation of the channels superimposes the images, removing the time difference.

Fig. 4.4 and 4.5 illustrates the aforementioned idea before channel co-registration and after channel co-registration.

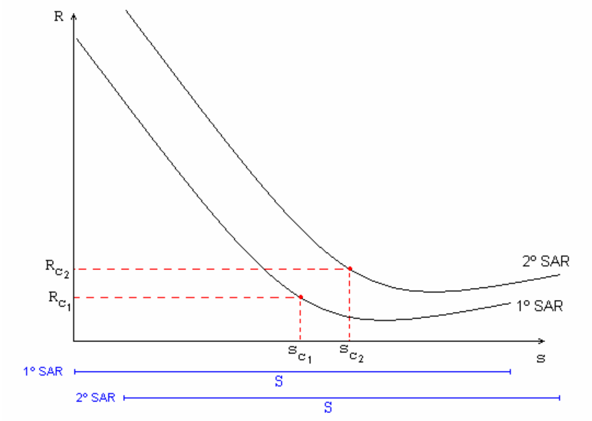

Fig. 4.4 Doppler history of a moving target for a two-channel ATI SAR before the coregistration

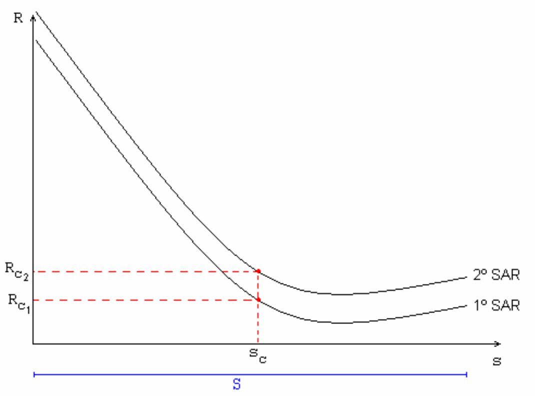

Fig. 4.5 Doppler history of a moving target for a two-channel ATI SAR after the coregistration

2) For a single channel SAR, splitting the antenna in two sub-apertures means to use each look to focus the pixel with coordinates (s_c, R_c). This means to have a temporal baseline. We should stress here that this is the key difference between the two approaches.

It is important to observe that for each sub-aperture the Doppler history does not change. The graphical representation is obtained shifting the partial phases of the aperture at the azimuth temporal center s_c, using the Doppler centroid f_{Dci} of the spectrum center for each look, where i indicates the number of look (i=1,2), as shown in Fig. 4.6 and 4.7.

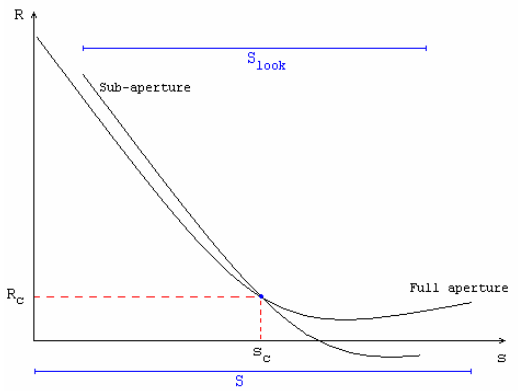

Fig. 4.6 Doppler history of the first look.

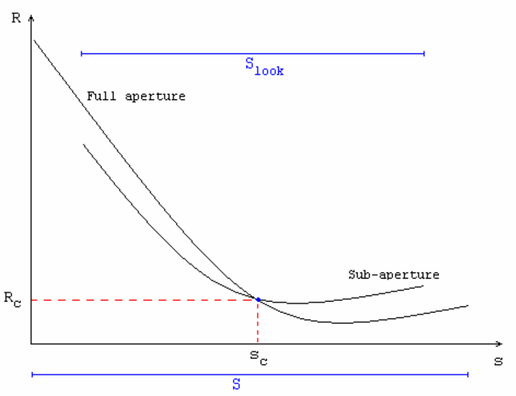

Fig. 4.7 Doppler history of the second look.

Every part of the Doppler history can be derived using the aperture center s_c the integration look time S_i and the Doppler centroid f_{Dci}.

Equivalently, we can choose an approach in the time domain, considering the look center time s_{ci}, the integration look time S_i and the Doppler centroid f_{Dc}. For the mathematical derivation we start from this second point of view. The result shows that we don't obtain a shift of the slant range center R_c between the two sub-apertures, because the Doppler history of the two looks derives from the same data.

Fig. 4.8 shows the difference of the co-registered sub-aperture channel.

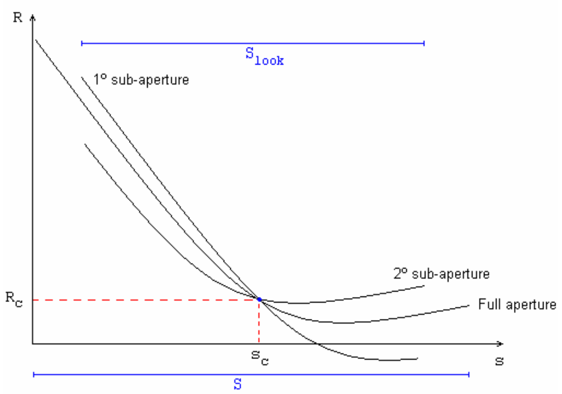

Fig. 4.8 Doppler history for two sub-apertures of a single channel SAR

4.3.3 SUB-APERTURE PROCESSING

We split the synthetic aperture in two symmetrical partially overlapped sub-apertures; the symmetry is chosen to generate two identical receiver channels with the same distance from the phase center.

The integration time of every look is given by $S_i = \eta_{ap} S$.

Before the azimuth compression, it is necessary to pre-filter the range compressed data in azimuth for each look. The filtering in the time domain has the aim of reducing the azimuth footprint of the antenna for each look therefore eliminating the contributions from the pulses outside the look footprint.

Let us consider that the filtered compressed data of the ith look result from the convolution between the data and a FIR filter, that is centered around the Doppler centroid f_{Dci} and has a Doppler band B_{Di} .

The impulse response of the FIR filter is [10]:

$$h_D(s) = \frac{B_{Di}}{PRF} \cdot \mathrm{sinc}\left(\frac{\pi s B_{Di}}{PRF}\right) \exp\left[j2\pi f_{Dci}\left(\frac{s}{PRF}\right)\right]. \tag{4.30}$$

The Doppler centroid of the look is obtained from the relation time-frequency [4]:

$$(f_D - f_{Dc}) = f_R\left(s - s_c\right). \tag{4.31}$$

For the i th look the Doppler centroid and the time centers are, respectively:

$$\begin{cases} f_{Dci} = f_{Dc} \pm \dfrac{S f_R}{2}\left(\eta_{ap} - 1\right) \\ s_{ci} = s_c \mp \dfrac{S}{2}\left(1 - \eta_{ap}\right) \end{cases}. \tag{4.32}$$

The look filtering is computed by the convolution:

$$.\,\hat{g}_{filter}(s,t\,|s_c,R_c) = \int_{-\infty}^{+\infty} \hat{g}(s^{'} \mid s_c, R_c) \cdot h_D(s - s^{'}) ds^{'} . \tag{4.33}$$

The filtered range compressed data of the i th look of a moving target results:

$$\begin{aligned} &\hat{g}_{filter}(s,t\,|s_c,R_c) = q z_c \exp\left\{ j2\pi\left[(f_{Dc} - v_{sr})(s - s_{ci}) + f_R \frac{(s - s_{ci})^2}{2}\right]\right\}\cdot \\ &\cdot \mathrm{sinc}\left\{ \pi B\left[t - \frac{2}{\mathrm{c}}\left(R_c - \lambda \frac{(f_{Dc} - v_{sr})}{2}(s - s_{ci}) - \lambda \frac{f_R}{2}\frac{(s - s_{ci})^2}{2}\right)\right]\right\} \end{aligned}, \tag{4.34}$$

with $\left|s-s_{ci}\right| \leq \frac{S_i}{2}$, where constant q includes the transmitted band and another terms derived to the filter, as B_{Di}/PRF.

For $t = t(s, R_c^{'} = R_c)$ we obtain:

$$\begin{aligned}\zeta(s_c{}'|s_{ci}, R_c) = qz_c \int_{s_{ci}-S_i/2}^{s_{ci}+S_i/2} &\exp\left\{ j2\pi\left[(f_{Dc} - v_{sr})(s - s_{ci}) + f_R \frac{(s-s_{ci})^2}{2} \right]\right\} \cdot \\ \cdot\text{sinc}\left\{ \frac{2\pi B}{c}\left[-\frac{\lambda v_{sr}}{2}(s-s_{ci}) \right]\right\} &\exp\left\{ -j2\pi\left[f_{Dc}(s - s_c{}') + f_R \frac{(s-s_c{}')^2}{2} \right]\right\} ds\end{aligned} \quad . \tag{4.35}$$

Finally, after a lengthy algebraic manipulation, shown in Appendix, we get the compressed impulse response function:

$$\begin{aligned}\zeta(s_c{}'|s_{ci}, R_c) = \frac{qS_i}{2}\text{sinc}\left\{2\pi S_i\left[-v_{sr} + f_R\left(s_c{}' - s_{ci}\right)\right]\right\}\exp\left[-j\left(\frac{4\pi R_c}{\lambda} + \frac{\pi}{2}\right)\right] \cdot \\ \cdot\exp\left\{ j2\pi\left[f_{Dc}\left(s_c{}' - s_{ci}\right) + f_R\left(s_c{}' - s_{ci}\right)s_{ci} + \frac{f_R}{2}\left(s_{ci}^2 - s_c^{'2}\right)\right]\right\}\end{aligned} \quad . \tag{4.36}$$

From (4.36) we obtain the amplitude and the phase of the compressed signal:

$$A_i(s_c{}'|s_{ci}, R_c) = \frac{qS_i}{2}\text{sinc}\left\{2\pi S_i\left[-v_{sr} + f_R\left(s_c{}' - s_{ci}\right)\right]\right\}, \tag{4.37}$$

$$\begin{aligned}\Phi_i(s_c{}'|s_{ci}, R_c) = -\left(\frac{4\pi R_c}{\lambda} + \frac{\pi}{2}\right) + \\ +2\pi\left[f_{Dc}\left(s_c{}' - s_{ci}\right) + f_R\left(s_c{}' - s_{ci}\right)s_{ci} + \frac{f_R}{2}\left(s_{ci}^2 - s_c^{'2}\right)\right]\end{aligned} \quad . \tag{4.38}$$

The expression (4.37) shows that the amplitude does not change with the look, even if it depends on the range velocity. Only the amplitude peak shifts to the position

$$s_c{}' = s_{ci} - \frac{v_{sr}}{f_R} \tag{4.39}$$

as function of the distance between the time centers and the range velocity. From (4.38) is shown that the phase of the looks is not sensitive to the radial velocity. This result is in agreement with that of [10], and demonstrates that the estimate of the radial velocity is not possible using ATI technique on splitted sub-aperture images of a single channel.

4.3.4 SIMULATION RESULTS

To validate the previously derived theory, we simulated the SAR focusing of a moving target using MATLAB.
The simulator works in steps:

1. Generate an azimuth chirp of a moving point-like target using (4.28).
2. Compensate the range migration for a stationary target using eq. (4.22)
3. The range compressed data is filtered to obtain two symmetrical sub-apertures.
4. The filtered range compressed data is correlated with the azimuth reference function to focus the target.
5. Finally the range velocity and the baseline are varied, to demonstrate that the phase and the amplitude level are independent of the velocity.

For illustration purposes only we illustrate the simulation results of the azimuth compression of a stationary target.

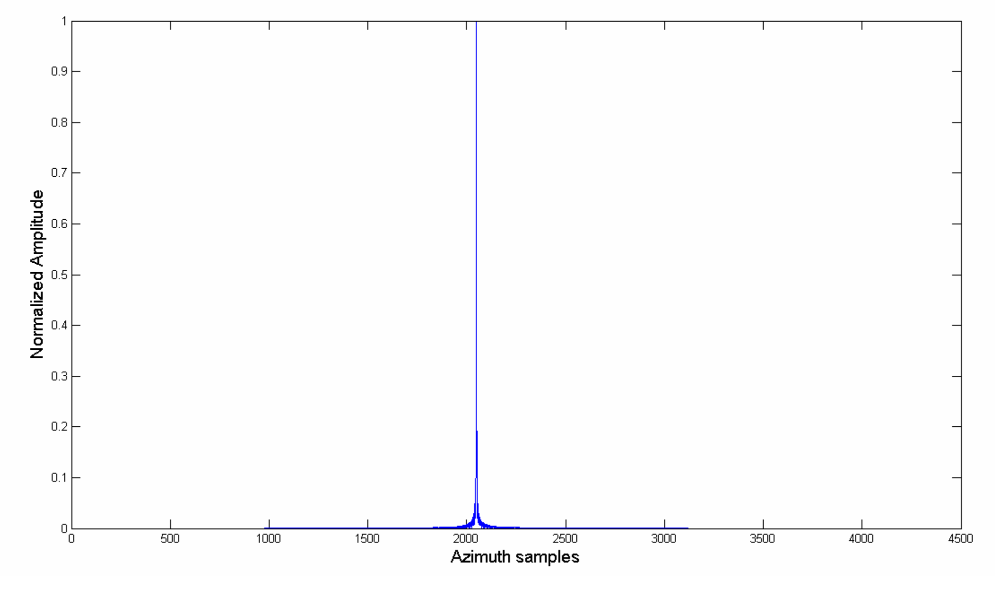

Fig. 4.9 Compression of the target after the azimuth correlation.

The parameters used in the simulations correspond to those of ERS satellites, as shown in Table 1.

TABLE 4.1
Used parameter values and symbols

Parameter	**Symbol**	**Value**
Frequency rate of linear FM waveform	K	0.418 MHz/μs
Frequency carrier	f_c	5,3 GHz
Pulse time	τ	37,12μs
Pulse bandwith	B	15,55 MHz
Pulse Repetition Frequency	PRF	1679.9Hz
Satellite velocity	V_{sat}	7500 m/s
Satellite height	H	790 km
Slant range at the broadside	R_0	827 Km
Elevation angle	θ	23°
Processed Doppler bandwith	B_D	1378 Hz
Doppler centroid	f_{Dc}	260 Hz
Doppler rate	f_R	-2156 Hz/s

To validate the theory we varied the look aperture between the interval [0,6; 0,9] to obtain two sub-apertures partially overlapped. The velocity varies between [0; 20m/s].

To verify the differential informative content we calculated the percentage differential amplitude and the differential phase between the looks as illustrated in Tables 4.2 and 4.3.

TABLE 4.2
Percentage differential amplitude between the sub-apertures

Aperture look (%)	60	70	80	90
Velocity (m/s)				
0	0	0	0	0
5	1.3	0.36	0.03	0
10	2.6	0.69	0	0
15	3.8	0.86	0.03	0
20	5.1	0.79	0	0

TABLE 4.3
Differential phase between the sub-apertures

Aperture look (%)	60	70	80	90
Velocity (m/s)				
0	0	0	0	0
5	π/113	< π/1000	< π/1000	< π/1000
10	π/58	< π/1000	< π/1000	< π/1000
15	π/39	< π/1000	< π/1000	< π/1000
20	π/30	< π/1000	< π/1000	< π/1000

From the obtained results, the phase results independent of the range velocity: this demonstrates that we do not have information about the range velocity from the phase of multi-look SAR images.

From the simulated results we can observe that the amplitude and the phase differential between the two channels shows a negligible increase with the velocity.

Probably this is due to the numerical approximations of the SAR processor and from the simplifications that we considered to derive (4.36).

In fact, we considered

$$\operatorname{sinc}\left\{\frac{2\pi B}{c}\left[-\frac{\lambda v_{sr}}{2}(s-s_{ci})\right]\right\}\approx 1,$$

which is a good approximation but not an exact value.

Moreover, the theory considers a filtering with a FIR filter with infinite length, which corresponds to an ideal filtering in the frequency domain. However, in the implementation we use a FIR filter (with N coefficients), therefore introducing an error.

The results obtained confirm reasonably the derived theory: the phase information obtained by using the ATI technique on sub-apertures is not relevant for velocity estimation but only for moving target detection, which agrees with results from [11].

4.4 CONCLUSION

This chapter presented a complete analysis about the effects of the radial motion on the sub-aperture processing. The work investigates if the presence of the range velocity influences significantly the phase and the amplitude of the two symmetrical sub-apertures, considering the possibility to apply ATI techniques to the two looks.

However, the developed theory and the simulations herein presented rules out this possibility and helps to completely understand the difference between multi-channel SAR and multi-look processing in the velocity estimation.

The only method to estimate the radial velocity from two sub-apertures is to calculate the shift of the amplitude peak of the IRF, by varying the phase center between the two looks.

APPENDIX

This appendix derives the simplification of (4.36).

Considering $C = qz_c$, the azimuth compression of the i $^{\text{th}}$ look results:

$$\zeta(s_c', s_{ci}, R_c) = C \int_{s_{ci}-S_i/2}^{s_{ci}+S_i/2} \exp\left\{ j2\pi \left[(f_{Dc} - v_{sr})(s - s_{ci}) + f_R \frac{(s - s_{ci})^2}{2} \right] \right\} \cdot$$

$$\cdot \text{sinc}\left\{ \frac{2\pi B}{c} \left[-\frac{\lambda v_{sr}}{2}(s - s_{ci}) \right] \right\} \exp\left\{ -j2\pi \left[f_{Dc}(s - s_c') + f_R \frac{(s - s_c')^2}{2} \right] \right\} ds =$$

$$= C \exp\left\{ j2\pi \left[f_{Dc}\left(s_c' - s_{ci}\right) + v_{sr} s_{ci} + \frac{f_R}{2}\left(s_{ci}^2 - s_c'^2\right) \right] \right\} \int_{s_{ci}-S_i/2}^{s_{ci}+S_i/2} \exp\left\{ j2\pi \left[-v_{sr} + f_R \left(s_c' - s_{ci}\right) \right] s \right\} \cdot$$

$$\cdot \text{sinc}\left\{ \frac{2\pi B}{c} \left[-\frac{\lambda v_{sr}}{2}(s - s_{ci}) \right] \right\}$$

To simplify the expression we can expand the sinc function in Taylor series around s_c, considering that:

$$\text{sinc}(x) = \frac{\sin(x)}{x}$$

and that around x=0

$$\sin(x) = \sum_{n=0}^{\infty} \frac{(-1)^n}{(2n+1)!} x^{2n+1} = x - \frac{x^3}{3!} + \ldots$$

Using a first order approximation we can write:

$$\text{sinc}\left\{ \frac{2\pi B}{c} \left[-\frac{\lambda v_{sr}}{2}(s - s_{ci}) \right] \right\} = \frac{\sin\left\{ \frac{2\pi B}{c} \left[-\frac{\lambda v_{sr}}{2}(s - s_{ci}) \right] \right\}}{\frac{2\pi B}{c} \left[-\frac{\lambda v_{sr}}{2}(s - s_{ci}) \right]} \approx \frac{\frac{2\pi B}{c} \left[-\frac{\lambda v_{sr}}{2}(s - s_{ci}) \right]}{\frac{2\pi B}{c} \left[-\frac{\lambda v_{sr}}{2}(s - s_{ci}) \right]} = 1.$$

So the compression becomes:

$$\zeta(s_c', s_{ci}, R_c) = C \exp\left\{ j2\pi \left[f_{Dc}\left(s_c' - s_{ci}\right) + v_{sr} s_{ci} + \frac{f_R}{2}\left(s_{ci}^2 - s_c'^2\right) \right] \right\} \cdot$$

$$\cdot \left. \frac{\exp\left\{ j2\pi \left[-v_{sr} + f_R \left(s_c' - s_{ci}\right) \right] s \right\}}{j2\pi \left[-v_{sr} + f_R \left(s_c' - s_{ci}\right) \right]} \right|_{s_{ci}-S_i/2}^{s_{ci}+S_i/2} =$$

$$= C\exp\left\{ j2\pi\left[f_{Dci}\left(s_c{}'-s_{ci}\right)+v_{sr}s_{ci}+\frac{f_R}{2}\left(s_{ci}^2-s_c^{'2}\right)\right]\right\}\cdot$$

$$\cdot\frac{\exp\left\{j2\pi\left[-v_{sr}+f_R\left(s_c{}'-s_{ci}\right)\right]\left(s_{ci}+S_i/2\right)\right\}-\exp\left\{j2\pi\left[-v_{sr}+f_R\left(s_c{}'-s_{ci}\right)\right]\left(s_{ci}-S_i/2\right)\right\}}{j2\pi\left[-v_{sr}+f_R\left(s_c{}'-s_{ci}\right)\right]}=$$

$$= C\exp\left\{ j2\pi\left[f_{Dc}\left(s_c{}'-s_c\right)+v_{sr}s_{ci}+\frac{f_R}{2}\left(s_c^2-s_c^{'2}\right)\right]\right\}\cdot\exp\left\{j2\pi\left[-v_{sr}+f_R\left(s_c{}'-s_{ci}\right)\right]s_{ci}\right\}\cdot$$

$$\cdot\frac{\exp\left\{j2\pi\left[-v_{sr}+f_R\left(s_c{}'-s_{ci}\right)\right]S_i/2\right\}-\exp\left\{-j2\pi\left[-v_{sr}+f_R\left(s_c{}'-s_{ci}\right)\right]S_i/2\right\}}{j2\pi\left[-v_{sr}+f_R\left(s_c{}'-s_{ci}\right)\right]}=$$

Remembering that $\sin(x)=\dfrac{\exp(jx)-\exp(-jx)}{2j}$, we obtain:

$$= C\exp\left\{ j2\pi\left[f_{Dci}\left(s_c{}'-s_{ci}\right)+v_{sr}s_c+\frac{f_R}{2}\left(s_{ci}^2-s_c^{'2}\right)\right]\right\}\cdot\exp\left\{j2\pi\left[-v_{sr}+f_R\left(s_c{}'-s_{ci}\right)\right]s_{ci}\right\}\cdot$$

$$\cdot\frac{2\sin\left\{2\pi\left[-v_{sr}+f_R\left(s_c{}'-s_{ci}\right)\right]S_i/2\right\}}{2\pi\left[-v_{sr}+f_R\left(s_c{}'-s_{ci}\right)\right]}\cdot\frac{S_i/2}{S_i/2}=$$

$$= C\exp\left\{ j2\pi\left[f_{Dci}\left(s_c{}'-s_{ci}\right)+v_{sr}s_{ci}+\frac{f_R}{2}\left(s_{ci}^2-s_c^{'2}\right)\right]\right\}\cdot\exp\left\{j2\pi\left[-v_{sr}+f_R\left(s_c{}'-s_{ci}\right)\right]s_{ci}\right\}\cdot$$

$$\cdot\frac{2\sin\left\{2\pi\left[-v_{sr}+f_R\left(s_c{}'-s_{ci}\right)\right]S_i/2\right\}}{2\pi\left[-v_{sr}+f_R\left(s_c{}'-s_{ci}\right)\right]}\cdot\frac{S_i/2}{S_i/2}=$$

$$= C\exp\left\{ j2\pi\left[f_{Dc}\left(s_c{}'-s_{ci}\right)+v_{sr}s_{ci}+\frac{f_R}{2}\left(s_{ci}^2-s_c^{'2}\right)\right]\right\}\cdot\exp\left\{j2\pi\left[-v_{sr}+f_R\left(s_c{}'-s_{ci}\right)\right]s_{ci}\right\}\cdot$$

$$\cdot S_i\mathrm{sinc}\left\{2\pi\left[-v_{sr}+f_R\left(s_c{}'-s_{ci}\right)\right]\frac{S_i}{2}\right\}$$

Finally we obtain:

$$\zeta(s_c{}',s_{ci},R_c)=CS_i\mathrm{sinc}\left\{2\pi S_i\left[-v_{sr}+f_R\left(s_c{}'-s_{ci}\right)\right]\right\}\exp\left[-j\left(\frac{4\pi R_c}{\lambda}\right)\right]\cdot$$

$$\cdot\exp\left\{ j2\pi\left[f_{Dc}\left(s_c{}'-s_{ci}\right)+f_R\left(s_c{}'-s_{ci}\right)s_{ci}+\frac{f_R}{2}\left(s_{ci}^2-s_c^{'2}\right)\right]\right\}.$$

REFERENCES

[1] M. Kirscht, “Detection and velocity estimation of moving objects in a sequence of single-look SAR images”, Proceedings of the IEEE Int. Geoscience Remote Sensing Symposium, IGARSS, Vol. 1, pp. 333-335, 27-31 May 1996.

[2] J. H.G. Ender, “Space-Time Adaptive Processing for Synthetic Aperture Radar”, IEE Colloquium on Space-Time Adaptive Processing (Ref. No. 1998/241), pp. 6/1-618, April 1998.

[3] J. H. G. Ender, P. Berens, A. R. Brenner, L. Rossing, U. Skupin, “Multi-channel SAR/MTI system development at FGAN: from AER to PAMIR”, Proceedings of the IEEE Int. Geoscience Remote Sensing Symposium, IGARSS, 24-28 June 2002

[4] J.C. Curlander, R. McDonough, ”Synthetic Aperture Radar, Systems and Signal Processing”, Wiley 1991

[5] B.C. Barber, “Theory of digital imaging from orbital Synthetic Aperture Radar”, Int. Journal of Remote Sensing, Vol. 6, No. 7, pp 1009-1057, 1985.

[6] S.J Frasier, A.J. Camps, “Dual-beam interferometry for ocean surface current vector mapping”, IEEE Transactions on Geoscience and Remote Sensing, Vol. 39 , Issue 2, Feb 2001, Pag. 401–414.

[7] R. Bamler, P. Hartl, “Synthetic Aperture Radar Interferometry”, DLR, Issue 4, Pag. R1-R54, August 1998

[8] A.Radius, D.Solimini, P.A.C.Marques, “Radial Velocity Estimation Limitations from SAR subaperture”, IEEE Aerospace and Electronic Systems Magazine (submitted), 2008.

[9] J.J.Sharma, C.H.Gierull, M.J.Collins, “The influence of Target Acceleration on Velocity Estimation in Dual-Channel SAR-GMTI”, IEEE Transactions on Geoscience and Remote Sensing, Vol. 44 , N. 1, pp. 134–147, Jan 2006.

[10] K. Ouchi, “On the Multilook Images of Moving Targets by Synthetic Aperture Radar”, IEEE Transactions on Antennas and Propagation, Vol.AP-33, N. 8, pp. 823-827 August 1985.

[11] F. Gao, S. Mao, Y. Yuan, Z. Yu, S. Liu, “Approaches of Single Channel SAR Combining ATI for GMTI”, Signal Processing, 8rd International Conference on, Vol. 4, 16-20 2006.

CHAPTER 5
SHIP VELOCITY ESTIMATION ALGORITHM USING AMPLITUDE SAR DATA

5.1 INTRODUCTION

In the past, SAR systems main goals were the study of the interaction between electromagnetic waves and the earth surface.

Quickly the intrinsic capability of this instrument to analyze the dynamic characteristics of the observed objects and the changes of the requirements of the users made the SAR particularly fit for moving target detection in commercial, surveillance and strategic context.

Ship monitoring is an application particularly fit for the SAR capability, due to its global monitoring capability and the strong interaction between SAR signal and this kind of targets; the fundamental phases of ship monitoring are the ship detection and velocity estimation.

The classical ship detection approach is to use the pixel intensity information, applying a Constant False Alarm Rate CFAR method [1].

Other detection metodology require raw data, and are based on a coherence analysis. Considering the motion effects of a moving target on multi-look processing [2], an alternative approach for ship detection is to compute the cross-correlation between split-look SAR images, considering that the ship has a coherent behaviour during the integration time, on the contrary of the sea; the key for detection is that the ship has an high correlation, while the sea a low correlation between the split-look images [3], [4].

Another proposed method uses the phase information instead of intensity between not overlapped sub-apertures, because the view angle changes affect much more the phase of a pixel than its intensity value. The pixel of the ship has a phase coherent behaviour during the integration time, while the sea has a strongly incoherent behaviour [5].

For the velocity estimation, some techniques were proposed. The fundamental key to derive the ship velocity is the spatial shift of a target, when it moves in radial direction.

In [6] and [7] the direction and the speed of a ship is derived analyzing the wake structure; the radial velocity is derived from the azimuth shift, and the absolute value of the velocity is derived from the estimation of the internal wave speed or from the determination of the internal wake opening angle. The method runs only when the wake is particularly visible.

In [8] a scan method is proposed to detect the ship wake and its direction, deriving the range velocity from the azimuth shift.

Another methods uses the Radon transform to detect the wake orientation and to derive the radial velocity of the moving object from the spatial shift ([7], [9], [10]).

More complex processors for moving target analysis need of *a priori* information, like a ship data set [11] for ship monitoring or a road data base [12] for a road traffic monitoring.

As shown, the development of the detection and velocity estimation techniques and their utility is correlated to the data type available on the market: in this point of view we focus our attention on ship monitoring from multilook images, which are easily available. Typical limitations of recently proposed techniques are the incapability to estimate the complete velocity vector of the ships without a priori knowledge and presuppositions that limit much their applicability in real context.

Herein we propose a simple, yet efficient and fast algorithm to detect the ships and estimate their full velocity without using any a priori knowledge. The algorithm is based on the Radon transform, which is introduced in the next paragraph.

5.2 THE RADON TRANSFORM

The Radon transform is a powerful mathematical instrument for line parameter extraction in images even in presence of noise. The advantage of the Radon transform is that it transforms a bi-dimensional problem into a mono-dimensional one.

Given an image *g* in the coordinate system (x,y), the Radon transform is defined as [13]:

$$\hat{g}(\rho,\theta) = \int_{-\infty}^{+\infty}\int_{-\infty}^{+\infty} g(x,y)\delta(\rho - x\cos\theta - y\sin\theta)dxdy\,, \tag{5.1}$$

where δ is the Dirac delta function; the integral line through the image g(x,y) is defined by the coordinate θ and ρ, that correspond respectively to the orientation and to the smallest distance to the origin of the coordinate system, as it shown in the fig.5.1.

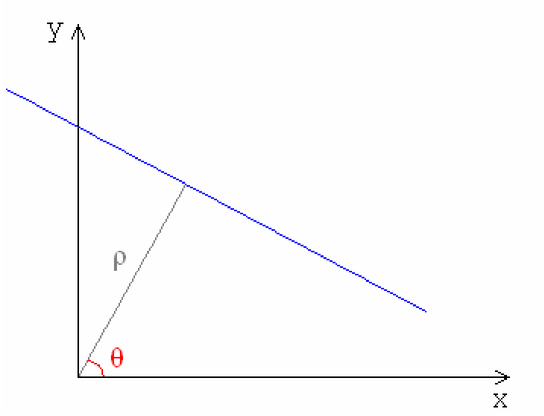

Fig.5.1 Coordinate system in the Radon domain

An equivalent form to represent the Radon transform is the following:

$$\hat{g}(\rho,\theta)=\int_{-\infty}^{+\infty} g(\rho\cos\theta - s\sin\theta, \rho\cos\theta - s\sin\theta)ds\,, \tag{5.2}$$

where the s-axis lies along the line.

So the Radon transform computes the projection of an image along the direction given by (ρ,θ), calculating the line integrals of the image along this direction.

It is important note that it results:

$$\begin{cases} 0 \le \theta < \pi \\ -\rho_{\max} \le \rho < \rho_{\max} \end{cases}. \tag{5.3}$$

The Radon transform is therefore interesting when in the image are present strong points and linear structures.

In the next paragraphs we will show as the point and the line become in the Radon domain, with the intent to apply this technique to the ship detection and velocity estimation.

5.2.1 THE RADON TRANSFORM OF A POINT SOURCE

A point source with coordinates $\left(x^*, y^*\right)$ is modelled as a product of two delta functions:

$$g(x,y)=\delta\left(x-x^*\right)\delta\left(y-y^*\right). \tag{5.4}$$

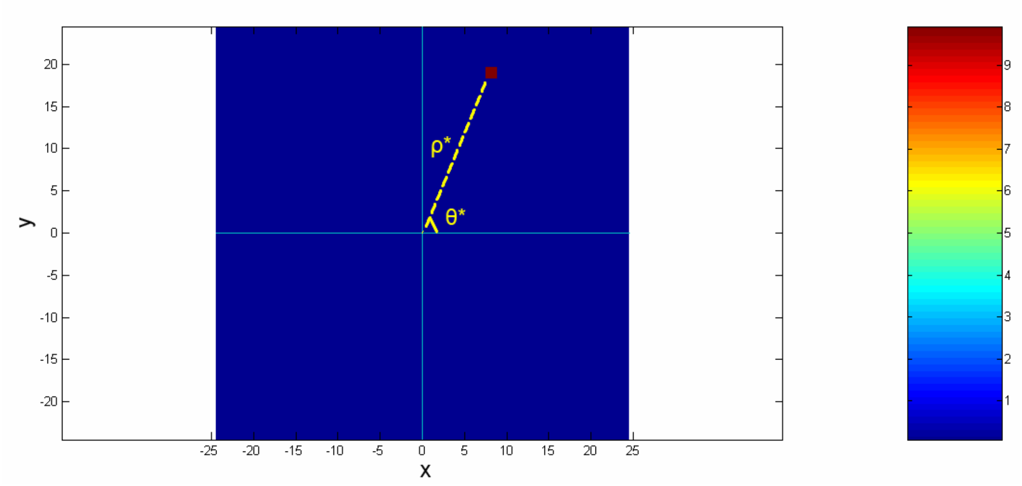

Fig.5.2 Radon transform of a point source in the (x,y) coordinates

So the Radon transform of this point is the following:

$$\begin{aligned}\hat{g}(\rho,\theta) &= \int_{-\infty}^{+\infty}\int_{-\infty}^{+\infty}\delta\left(x-x^*\right)\delta\left(y-y^*\right)\delta(\rho-x\cos\theta-y\sin\theta)dxdy = \\ &= \delta\left(\rho-x^*\cos\theta-y^*\sin\theta\right)\end{aligned} \quad . \tag{5.5}$$

The consequence is that a point source is transformed into a sinusoid function, and it is confined in the Radon domain:

$$\hat{g}(\rho,\theta)=0 \quad \text{for } \left|\rho\right|>\rho_{\max} . \tag{5.6}$$

We must take into account that the non ambiguity interval is $0 \le \theta < \pi$.

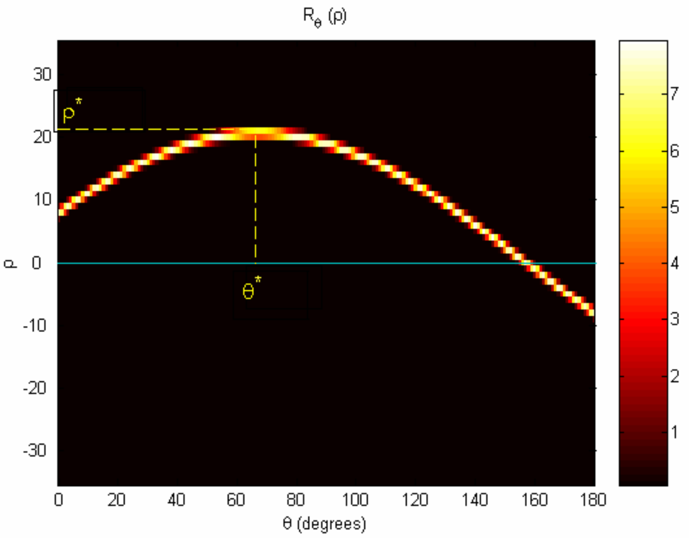

Fig.5.3 Radon transform of a point source in the (ρ,θ) coordinates

Figures 5.2 and 5.3 explain the relation between the coordinates $\left(\rho^*,\theta^*\right)$ in the spatial domain and in the Radon domain: the point is transformed in a sinusoidal function and the polar coordinates of the point correspond to the coordinate of the maximum of the curve.

5.2.2 THE RADON TRANSFORM OF A LINE

A line of parameters $\left(\rho^*,\theta^*\right)$ (Fig.5.4) is modelled with the delta function:

$$g(x,y)=\delta\left(\rho^*-x\cos\theta^*-y\sin\theta^*\right). \tag{5.7}$$

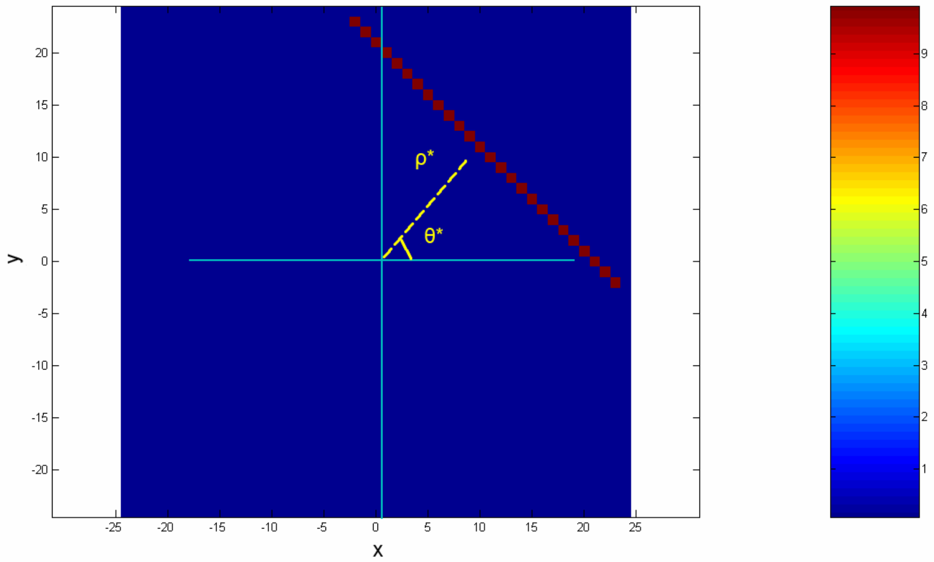

Fig.5.4 Radon transform of a line in the (x,y) coordinates

Considering that

$$\begin{cases} x=\rho\cos\theta-s\sin\theta \\ y=\rho\sin\theta+s\cos\theta \end{cases}, \tag{5.8}$$

the Radon transform results:

$$\hat{g}(\rho,\theta)=\int_{-\infty}^{+\infty}\delta\left(\rho^*-\rho\cos(\theta-\theta^*)+s\sin(\theta-\theta^*)\right)ds=$$

$$=\int_{-\infty}^{+\infty}\frac{1}{\left|\sin(\theta-\theta^*)\right|}\delta\left(\frac{\rho^*-\rho\cos(\theta-\theta^*)}{\sin(\theta-\theta^*)}+s\right)ds=\frac{1}{\left|\sin(\theta-\theta^*)\right|}, \tag{5.9}$$

for $\sin(\theta-\theta^*)\neq 0$.

If $\theta=\theta^*$ it results:

$$\hat{g}(\rho,\theta)=\int_{-\infty}^{+\infty}\delta\left(\rho^*-\rho\right)ds=\begin{cases} 0, & \rho^*\neq\rho \\ \int_{-\infty}^{+\infty}\delta(0)ds, & \rho^*=\rho \end{cases}. \tag{5.10}$$

So, when $\theta = \theta^*$ and $\rho = \rho^*$ we have an intensity peak, as showed in fig.5.5.

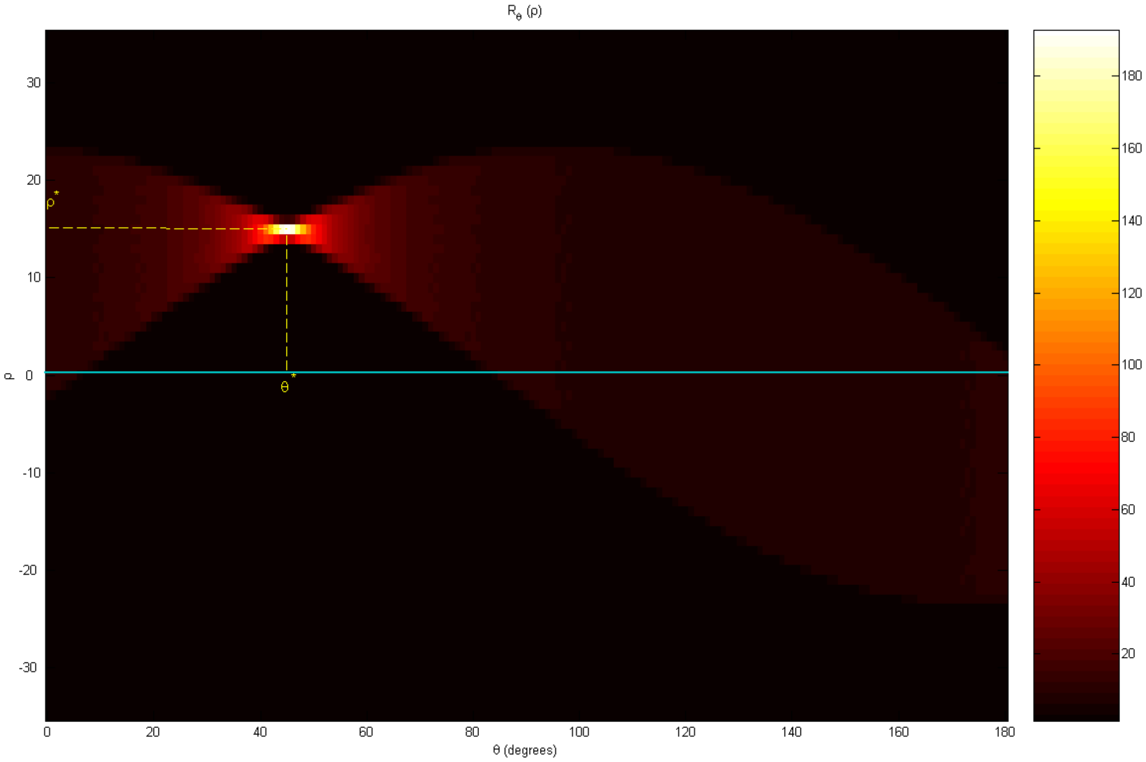

Fig.5.5 Radon transform of a line in the (ρ,θ) coordinates

5.3 SHIP DETECTION AND VELOCITY VECTOR ESTIMATION ALGORITHM

In this chapter we propose a novel methodology for ship detection and their full velocity vector extraction from SAR data, using only the amplitude information [14]. The algorithm uses the Radon transform to detect the ships and derive the two components of the velocity vector at the same time, from the wake orientation and the azimuth displacement. The main advantages are that the algorithm does not need any *a priori* information and it is very light from the computational point of view.

For the velocity estimation we propose 2 methods based on the Radon transform.

The method is structured in four steps, which allow to detect the ships present in the scene and to estimate their full velocity vector.

1. ANALYSIS: The histogram of the digital number of the pixels is derived from the image; the probability distribution that fits better the histogram is selected, choosing the threshold that contains the 99,9% of the values. The threshold is used in the second step for ship detection.
2. SHIP DETECTION: The ship number present on the scene is estimated using a CFAR (Constant False Alarm Rate) method. The ship map is generated and for every ship the algorithm gives the length and the coordinates. The Radon transform is used to verify the obtained results.
3. FOCUSING OF EVERY SHIP: Every ship is focused at the center of a scene, selecting an opportune window.
4. VELOCITY ESTIMATION: Two methods to estimate the velocity vector are proposed:
    - Estimate the wake orientation and the azimuth shift with the radon transform applied on the selected scene.
    - Estimate the ship orientation with the Radon transform and application of Radon transform for the estimated angle to calculate the azimuth shift.

5.3.1 ANALISYS

A sea scene is considered, masking the land. The histogram of the image is generated, with the intent to select a threshold that divides the sea values and the ship values.

Then we select the probability distribution that fits better the histogram obtained.

The threshold of the cumulative distribution function $F(x) = P(X \leq x)$ is evaluated, such that the stochastic variable X is inferior of the threshold x. The threshold is used for ship detection.

5.3.2 SHIP DETECTION

The ship detection technique used in the algorithm is a CFAR method [1], which is based on the selection of a threshold estimated in the analysis phase: only the pixels that have higher value than the threshold are classified as ship. The generated ship map is composed by pixels with a binary value 1 if the pixel is classified as ship, 0 otherwise.

A ship is a complex object, in that some strong scatterers are distributed; if the distribution is not homogeneous, the ship appears like a different target. To avoid this phenomenon, for every pixel classified like ship the algorithm sets to 1 the adjacent pixels.

From the ship map the algorithm finds the ships, their coordinate and the length, scanning for rows and columns.

The estimated number of ship is verified using the Radon transform.

The Radon transform is applied on the image, where every ship is seen as a source point: as we showed in subsection 5.2.1, the ships are mapped into sinusoidal functions in the Radon domain.

Because the Radon transform concentrates the energy into a sinusoidal function, every ship corresponds to an energy peak. To estimate the number of ships we analyze a profile of the Radon transform for a constant angle; the peaks correspond to the strong scatterers.

5.3.3 FOCUSING OF THE SHIPS

The algorithm isolates the target from the context and focuses the single ship at the center of the scene. Every sub-image is passed to the velocity estimation block. The window dimensions must be large enough, to contain the ship wake.

5.3.4 VELOCITY ESTIMATION ALGORITHM

The algorithms are based on the wake detection, estimating the range velocity component from the azimuth shift between the ship and the wake; the azimuth velocity is derived from the range velocity and the wake angle.

The algorithms propose two velocity estimation methods, based on the Radon transform.

The first derives the motion parameters from wake orientation estimation; we named this algorithm as WOVE, acronym formed from Wake Orientation to Velocity Estimation.

The second derives the velocity components from ship orientation estimation; we named this algorithm as SOVE, acronym formed from Ship Orientation to Velocity Estimation.

The analysis and comparison between them is proposed in the following chapters.

Note that the second method has a pre-processing phase.

5.3.4.1 PRE-PROCESSING

Firstly, the ship is masked to improve the wake sensitivity of the Radon transform, because a strong scatterer can interfere with the estimation.

Secondly, a high pass filter is applied in the spatial domain, to stress the wake with respect to the sea.

To stress the low values and to saturate the high levels the logarithm of the image is computed.

Finally, the values on the matrix are inverted linearly, to obtain that the low values (so the wake too) become high (image negative). This step is explained, considering that the Radon transform is more sensitive to find the maximum value (that corresponds to a bright line) than to find a minimum value (that correspond to a dark line).

5.3.4.2 METHOD WOVE

The facility of the Radon transform is used to detect the lines on an image, considering the wake as linear structure. The key idea of the algorithm is to focus the ship at the center of the scene and to apply the Radon transform, which determines the orientation of the wake and its distance from the center of the image.

Fig. 5.6 shows an example, in that $\underline{V}$ is the velocity vector and δ is the distance between ship and wake.

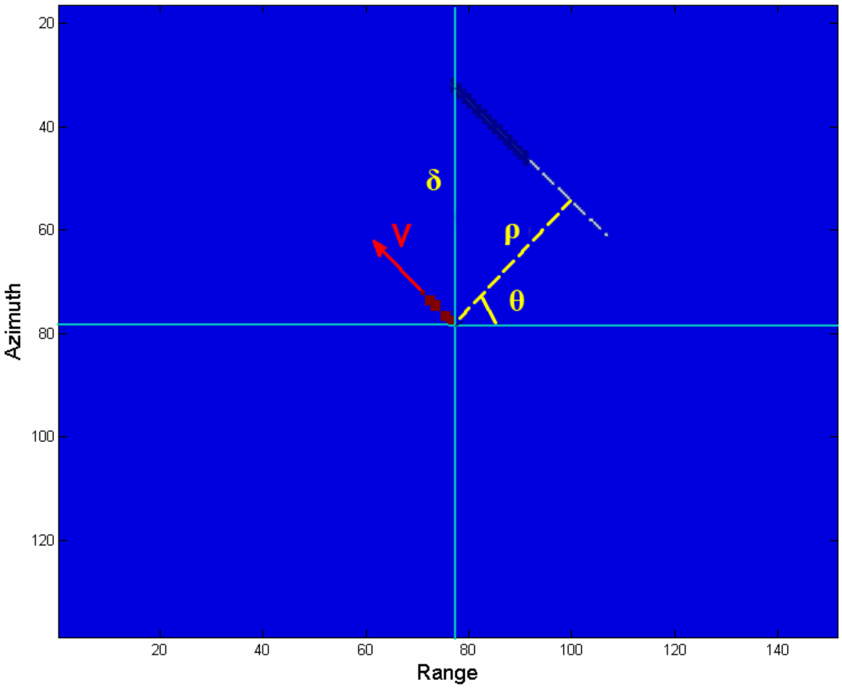

Fig.5.6 Simulated SAR image geometry of a ship and its wake

Because the ship is on the center, the Radon transform estimates at the same time the angle of the wake orientation and the azimuth shift between ship and wake, which is related to the range velocity.

The azimuth velocity is obtained from the wake orientation: the vector resulting lies on the straight line of the wake.

The Radon transform determines the couple (ρ,θ): these parameters are related to the azimuth shift from the following:

$$\rho = \delta \sin\theta \Rightarrow \delta = \frac{\rho}{\sin\theta}. \tag{5.11}$$

The couple (ρ,θ) allows to derive the range and azimuth velocity. In fact, the azimuth temporal shift of the moving target along the slant range is:

$$\eta_{shift} = \frac{2v_{sr}}{\lambda \cdot f_R}, \tag{5.12}$$

where v_{sr} is the slant range velocity and f_R the Doppler rate.

The spatial azimuth shift results:

$$\delta = v_B \cdot \eta_{shift}, \tag{5.13}$$

where v_B is the ground beam velocity.

The ground range velocity is so related to the azimuth shift:

$$v_{gr} = \frac{\lambda f_R \delta}{2v_B} \cdot \frac{1}{\sin\phi}, \tag{5.14}$$

where Φ is the incidence angle of the SAR.

The azimuth velocity is obtained from the expression (5.14):

$$v_{az} = v_{gr} \tan\theta. \tag{5.15}$$

5.3.4.3 METHOD SOVE

The ship wake is not always visible on the SAR images, depending on the sea state, the wind sea, the ship size and the ship velocity. When the difference between wake and surround sea is small, the presented method can fail.

A robust method is proposed, to run with a small wake-to-sea ratio.

In this method we obtain the orientation of the wake estimating the ship orientation.

Firstly the ship is focused at a known azimuth distance from the center.

Because the ship has an extended form, it is like a line. With Radon transform we estimate the orientation θ, taking the maximum of the image in the Radon domain. Note that the orientation is ambiguous of π.

Finally the ship is focused at the center of the scene and the Radon transform is applied to the image for the angle θ, to scan the space in the right direction; the distance from the ship is derived taking the maximum value of the vector generated from the transform. To resolve the ambiguity of the orientation estimate we scan all the space separately in the interval [0,π] and [π,2π].

The velocity components are estimated in the same mode of the method 1.

5.3.4.4 COMPARISON BETWEEN THE METHODS

The first method is very accurate when the wake values are much lower than the sea values. This means that the wake must be well visible. Unfortunately often the wake is not well visible and the first method fails as showed in the obtained results (Ch. 5.4)

The second method is less accurate, because the ship is considered as a line: the quality of this approximation depends on the lenght-width ratio and the noise. The method fails when the ship is too little or when the backscattering fluttuations don't allow to have a preferential direction. It is very important that the method does not require a very good wake visibility: the method is very robust.

Summarizing, the first method is very accurate but not very robust; also it fails if the wake is not much visible.

The second method is more robust but generally less precise in the velocity estimation than the first, because depends on the ship lenght and the backscattered energy; it fails if the ship doesn't present a preferential direction or appear as a point.

5.4 RESULTS

A comparison between the two methodologies is proposed, to stress the working modality difference.

The algorithms are tested with simulated and real data to characterize completely their advantages and disadvantages.

5.4.1 SIMULATION RESULTS

To test the two velocity estimation algorithm we simulated a scene in that is present a ship and its shifted wake.
Tab.5.1 shows the technical characteristics used to simulate the SAR scenario.

Tab.5.1

Parameter	**Symbol**	**Value**
Carrier frequency	f_c	5,3 GHz
Dimension of azimuth pixel	Δrg	12,5 m
Dimension of range pixel	Δaz	12,5 m
Bit per pixel	N	12
Doppler rate	f_R	-2156 Hz/s
Signal to clutter ratio	SCR	23 dB

The characteristics of the ships estimated by the algorithm are the lenght, the orientation, the range and azimuth velocity. Tab.5.2 shows the values used in the simulation.

Tab.5.2

Parameter	**Symbol**	**Value**
Ship lenght	L	124 m
Orientation ship	θ	135°
Range velocity	v_{rg}	-5,8 m/s
Azimuth velocity	v_{az}	-5,8 m/s

Firstly, we have considered a constant background and a wake-background ratio of -3 dB; both algorithms gave the same results.

Tab.5.3

L	**θ**	v_{rg}	v_{az}	**Error** v_{rg}	**Error** v_{az}
124 m	135°	-6,1 m/s	-6,1 m/s	5%	5%

To simulate a more realistic scenario it is necessary to add the noise into the image.
To model the sea we used the gamma distribution function, which fits very well the sea backscattering ([15], [16]).
The gamma distribution is defined as:

$$f(x|\mathrm{a,b})=\frac{1}{\mathrm{b^a}\Gamma(\mathrm{a})}\cdot x^{a-1}\exp\left(-\frac{x}{b}\right),\qquad \mathrm{x,a,b}>0 \tag{5.16}$$

$$\Gamma(a) = \int_0^\infty \exp(-t) \cdot t^{a-1} dt . \tag{5.17}$$

The mean value and the variance result:

$$\begin{cases} \mu = ab \\ \sigma = ab^2 \end{cases} . \tag{5.18}$$

To consider the speckle effect, we vary the variance of the gamma function; to analyze the sensitivity of the methodology to the wake visibility we vary the ratio between background mean level and the wake level (Wake-Sea Ratio, WSR).

Considering the tipical values in a real scenario, the variance is varied between the interval [1000, 10000], and the WSR between [-5 dB, -1 dB].

A graphical presentation of the results is presented in Fig. 5.7, 5.8, 5.9, 5.10, where the velocity vector error for the estimation algorithms are plotted on the variance-WSR plane, where the values of WSR are negative. The numerical results are shown in appendix.

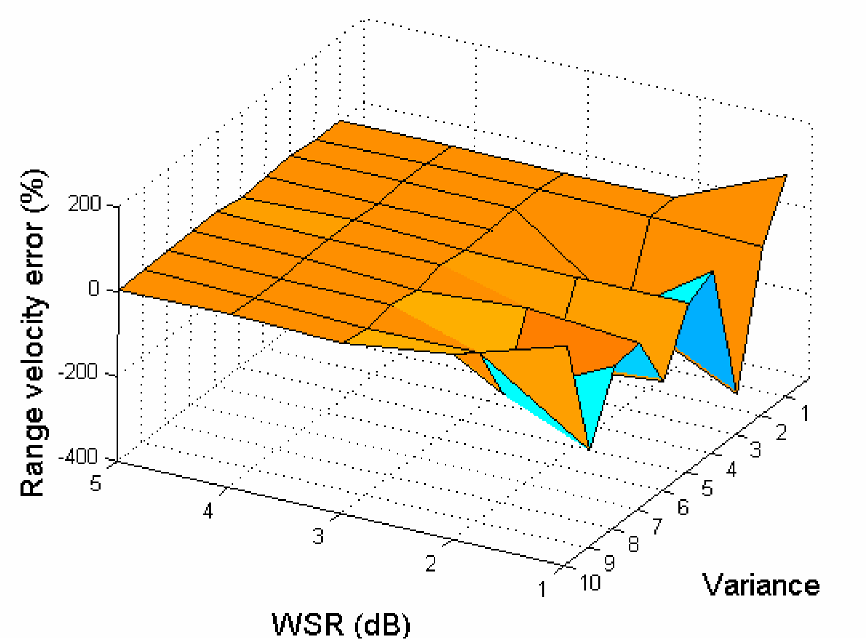

Fig.5.7 Range velocity error (first algorithm)

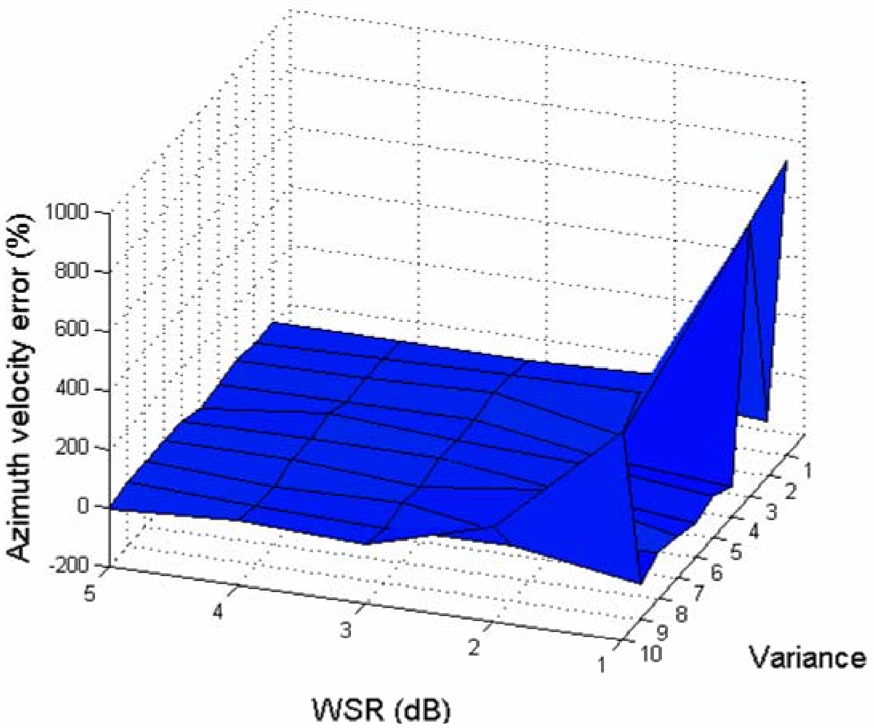

Fig.5.8 Azimuth velocity error (first algorithm)

Note that the first algorithm results accurate for a WSR higher than -2 dB.
The second algorithm results more robust, producing good results for a WSR higher than -1 dB, as shown in Fig 5.9 and 5.10.

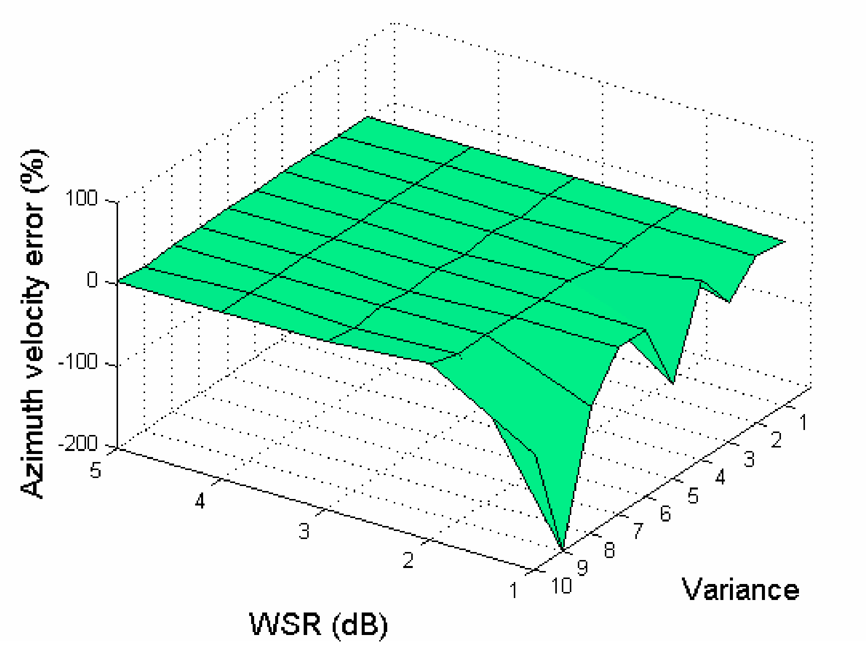

Fig.5.9 Range velocity error (second algorithm)

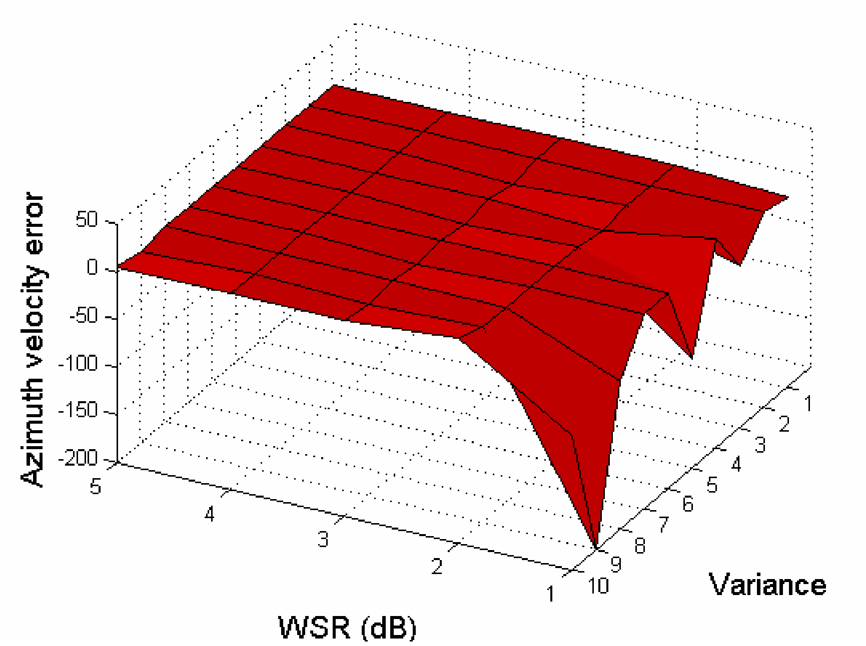

Fig.5.10 Azimuth velocity error (second algorithm)

Tab.5.6 shows the mean and the variance of the error vector for the range and azimuth velocity. The performance of the SOVE algorithm is clearly visible, with a mean error and a variance lower than in the WOVE algorithm.

Tab.5.4

	Mean error v_{rg} (%)	Variance error v_{az}	Mean error v_{az} (%)	Variance error v_{az}
Estimation Algorithm				
1	-14.7	73.3	36.3	168.7
2	-4.1	33	-4.1	33

Fig. 5.11, 5.12 and 5.13 show an example of the simulated SAR images.

As shown, with a WSR of -1 dB and a big variance (10000), corresponding to the last case, the wake is not visible. These values represent the physical limits, which make very hard the velocity estimation.

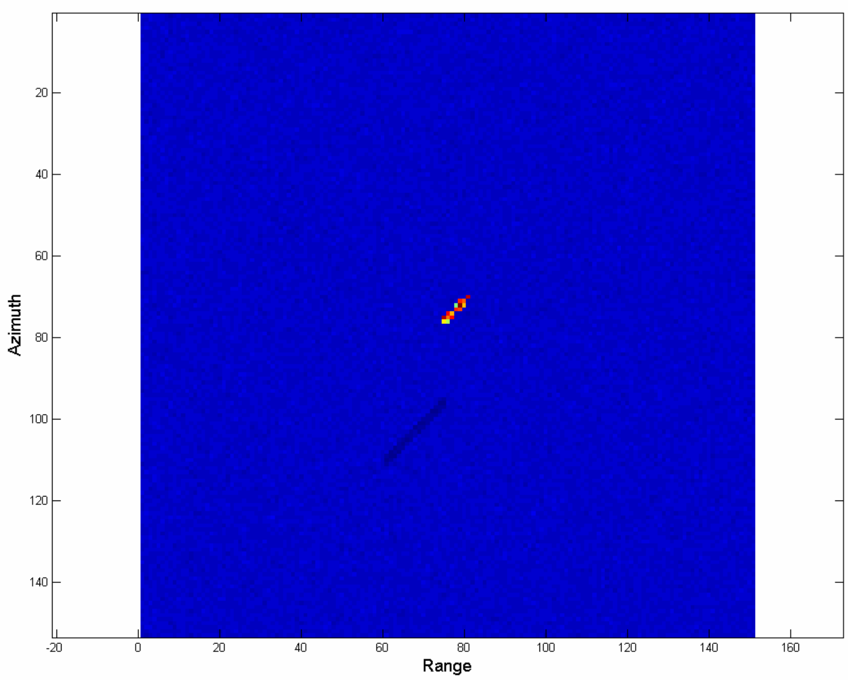

Fig.5.11 Simulated SAR image with a wake to sea ratio of -5 dB and a variance of 1000.

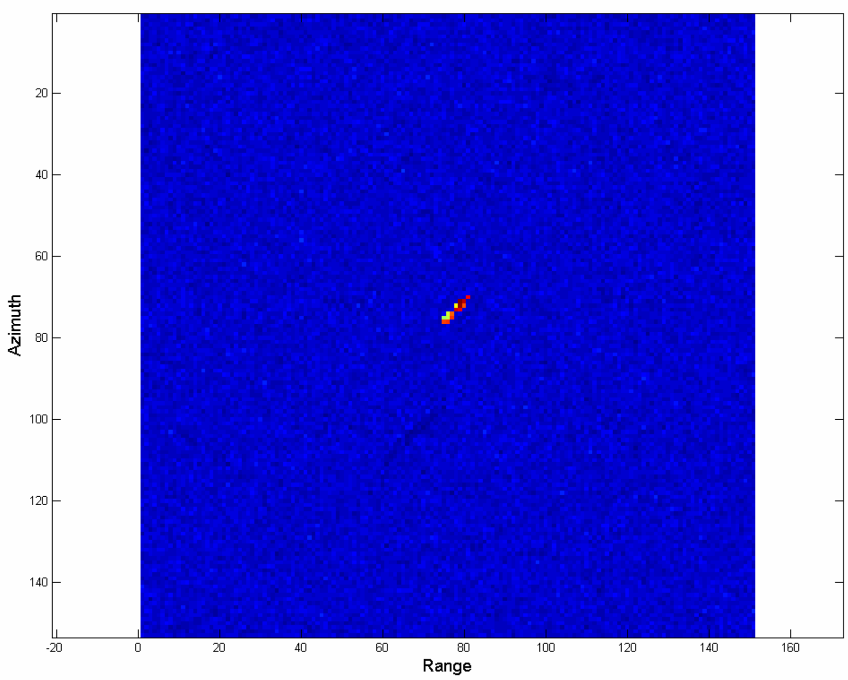

Fig.5.12 Simulated SAR image with a wake to sea ratio of -3 dB and a variance of 5000.

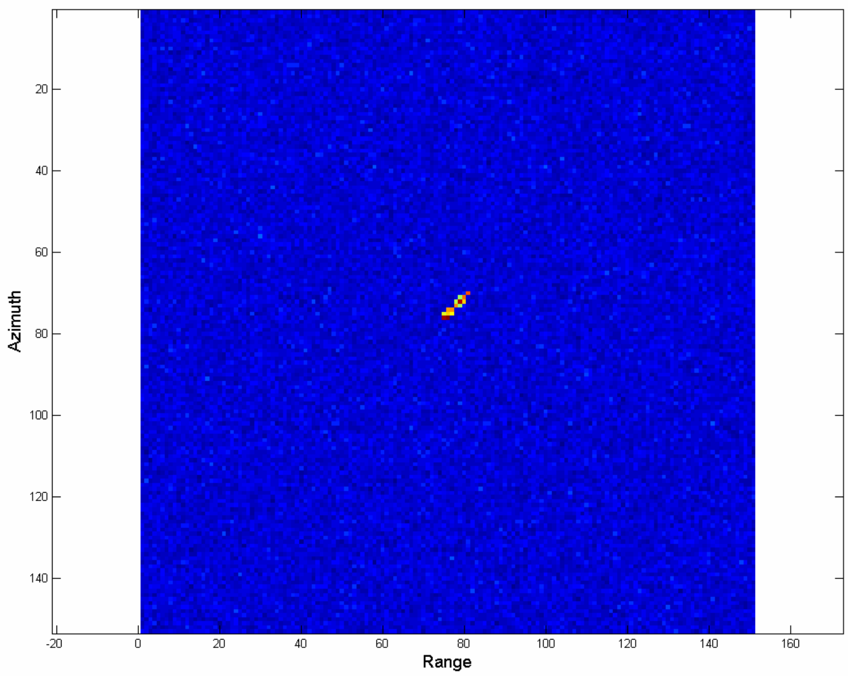

Fig.5.13 Simulated SAR image with a wake to sea ratio of -1 dB and a variance of 10000.

The obtained results show that the first algorithm is very sensitive to the wake to sea ratio, and when the clutter covers partially the dark wake, it doesn't work well. The second algorithm is very accurate and robust, and it failed only in very strong conditions.

The motivations of these results are that we considered a ship regular form: this allows to estimate with high precision the ship orientation. This gives a big advantage to the second method, which is able to estimate accurately the orientation of the ship.

Note that in the second algorithm the range velocity error is the same of the azimuth velocity error. The motivation is that the algorithm estimates correctly the wake angle, and the azimuth velocity is related to the range velocity and the wake orientation: for the symmetry of the scene (the azimuth component is the same of the range component), the error of the range velocity is propagated on the azimuth velocity.

To consider all the possible parameters we apply the estimation algorithms on real data.

Note that for every simulation the noise is random. It can be that the wake is partially masked or that the random distribution generates some pseudolinear structures, and this produces estimation errors, especially in the first method.

5.4.2 REAL DATA RESULTS

The real data used to validate the algorithm are the scene of ERS2 (frame 16466, orbit 2763), kindly provided to us by ESA, centered on Anzio city. In the images there are two ships, which have respectively a SCR (Signal to Clutter Ratio) of 26.4 dB and 30 dB.

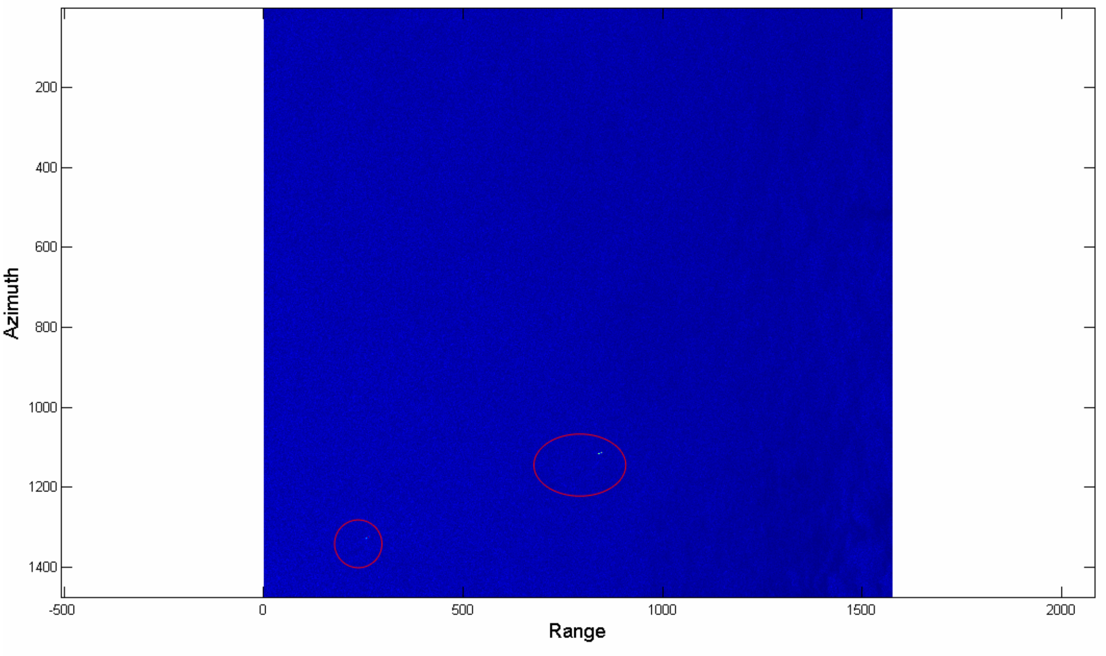

Fig.5.14 Amplitude image of the considered sea scene.

ANALYSIS

The image values are analyzed to derive the histogram of the image. Note that the amplitude image is coded with N=16 bit and the maximum value is 6200.

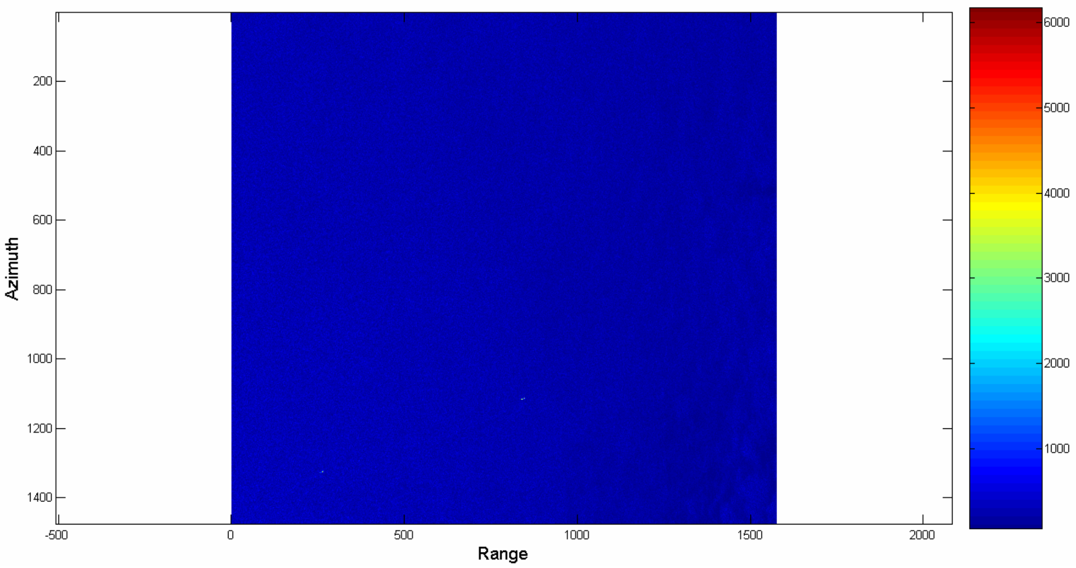

Fig.5.15 Amplitude image using to derive the histogram.

The histogram is obtained with the statistics Toolbox of MATLAB: the command *difittool* generates the histogram of the value of the image, as shown in Fig. 5.16.

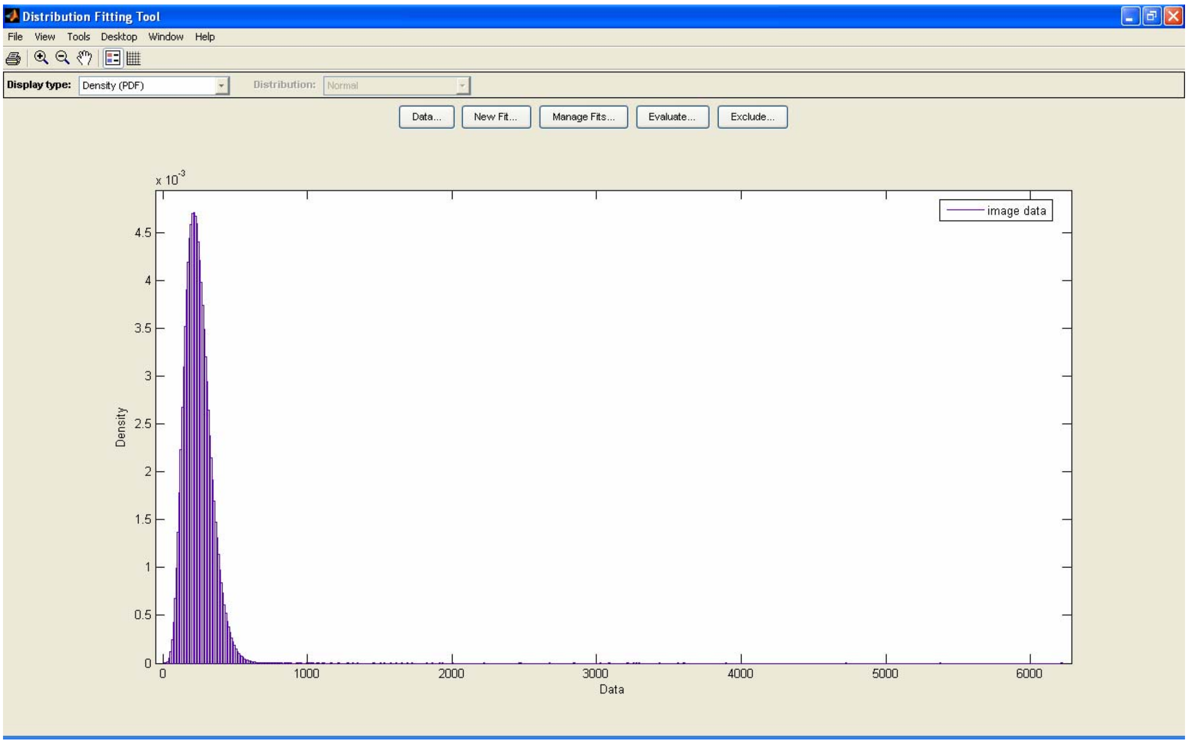

Display type: Density (PDF)
Distribution: Normal

Fig.5.16 Histogram of the sea image.

We select the probability distribution that fits better the histogram obtained. For the sea the Gamma distribution fits very well the histogram.

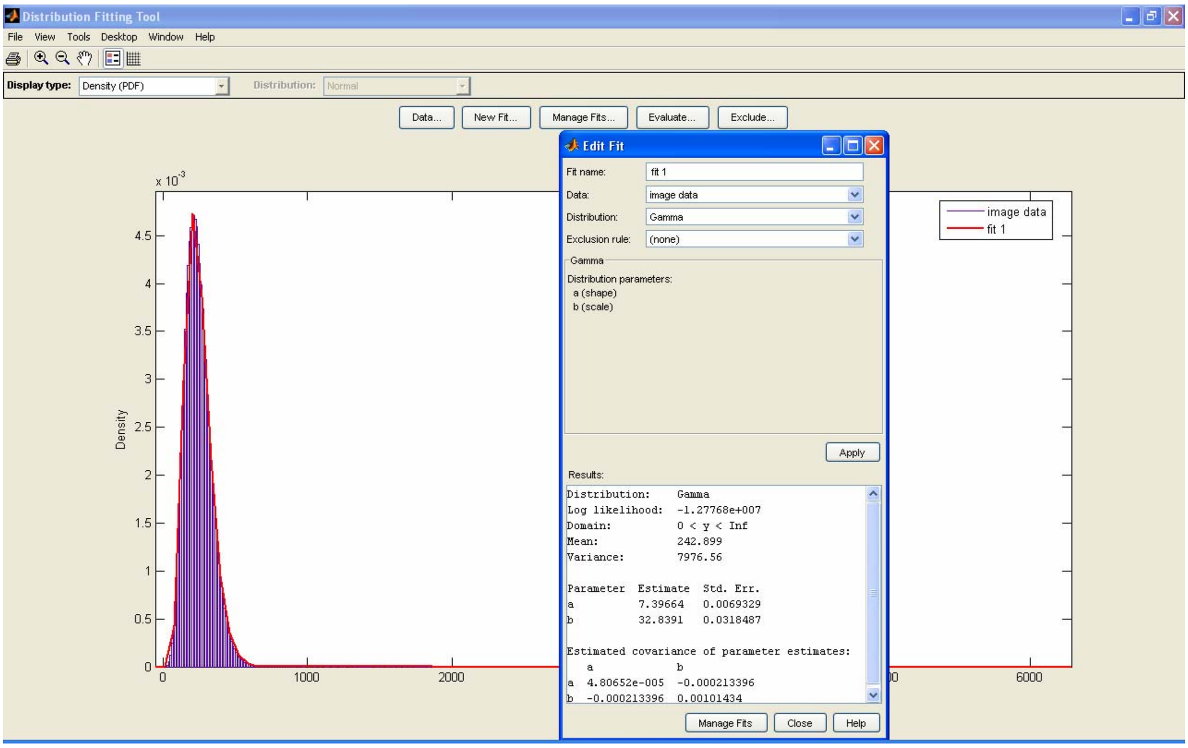

Display type: Density (PDF)
Distribution: Normal

Fit name: fit 1
Data: image data
Distribution: Gamma
Exclusion rule: (none)

Gamma
Distribution parameters:
a (shape)
b (scale)

Results:

```
Distribution:    Gamma
Log likelihood:  -1.27768e+007
Domain:          0 < y < Inf
Mean:            242.899
Variance:        7976.56

Parameter  Estimate  Std. Err.
a          7.39664   0.0069329
b          32.8391   0.0318487

Estimated covariance of parameter estimates:
   a             b
a  4.80652e-005  -0.000213396
b  -0.000213396  0.00101434
```

Fig.5.17 Fitting of the histogram with a gamma distribution.

We evaluate the threshold of the cumulative distribution function $F(x) = P(X \leq x)$, such that the aleatory variable X is inferior to the threshold x. The first value of x for that the cumulative distribution function is the 100% is chosen.

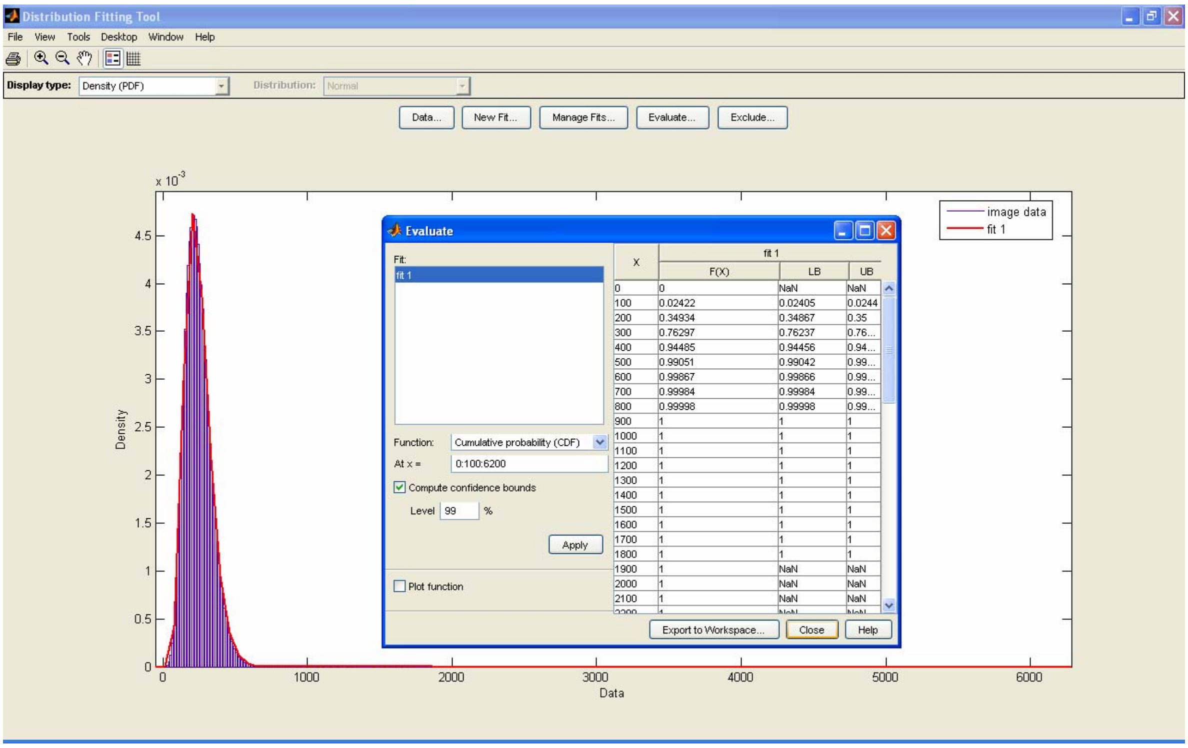

Fit: fit 1

Function: Cumulative probability (CDF)

At x = 0:100:6200

☑ Compute confidence bounds

Level 99 %

Apply

☐ Plot function

X	fit 1		
	F(X)	LB	UB
0	0	NaN	NaN
100	0.02422	0.02405	0.0244
200	0.34934	0.34867	0.35
300	0.76297	0.76237	0.76...
400	0.94485	0.94456	0.94...
500	0.99051	0.99042	0.99...
600	0.99867	0.99866	0.99...
700	0.99984	0.99984	0.99...
800	0.99998	0.99998	0.99...
900	1	1	1
1000	1	1	1
1100	1	1	1
1200	1	1	1
1300	1	1	1
1400	1	1	1
1500	1	1	1
1600	1	1	1
1700	1	1	1
1800	1	1	1
1900	1	NaN	NaN
2000	1	NaN	NaN
2100	1	NaN	NaN

Fig.5.18 Selection of the threshold to apply to the CFAR method.

The threshold value results 900, and is used in the CFAR method to detect the ships.

SHIP DETECTION

The CFAR method is used with the derived threshold. Remembering that a ship is a complex object, often the ship appears like different target. To avoid this phenomenon, for every pixel classified like ship the algorithm sets to 1 the adjacent pixels.

The ship map obtained with the CFAR method is shown in Fig.5.19.

To confirm the number of found ships, we use the Radon transform: every ship is mapped into a sinusoidal function in the Radon domain (Fig. 5.20).

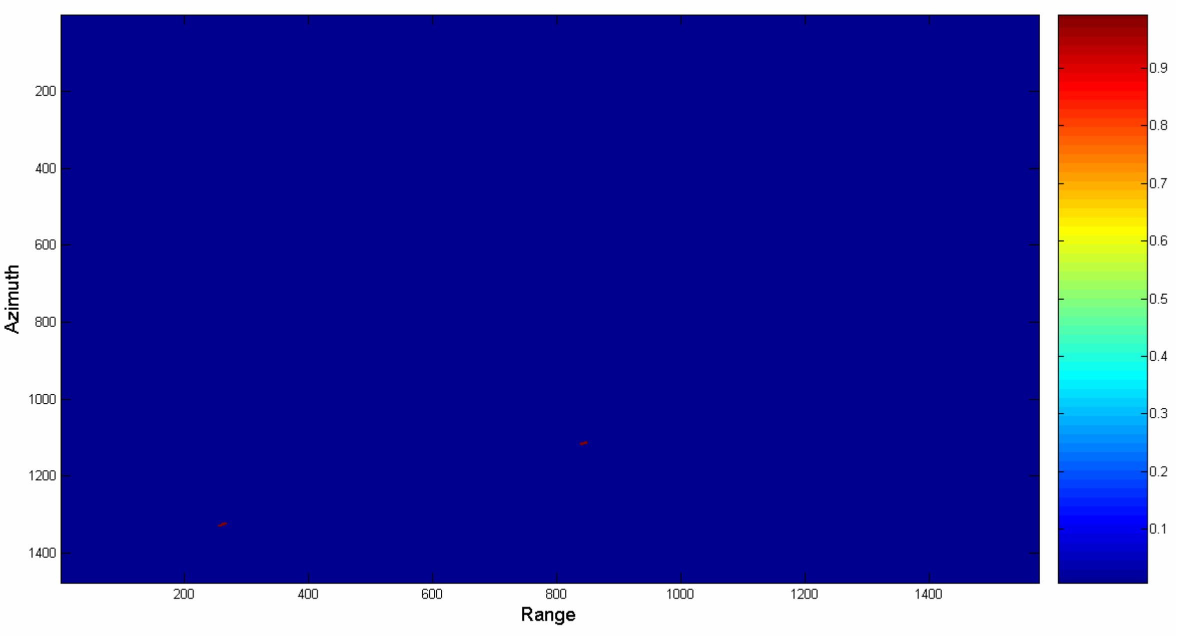

Fig.5.19 Ship map obtained with CFAR method.

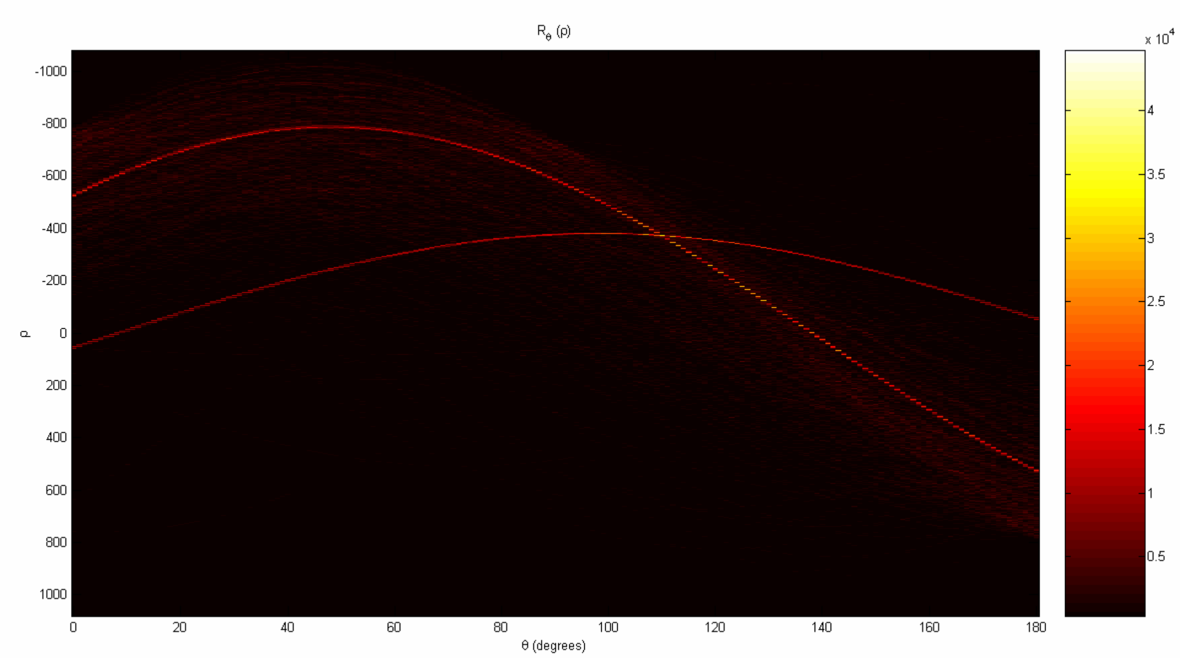

Fig.5.20 Radon transform of the sea scene.

Selecting a determinated angle θ, every ship appears like a peak in the Radon domain, as shown in Fig.5.21: the Radon transform confirms the right number of ships.

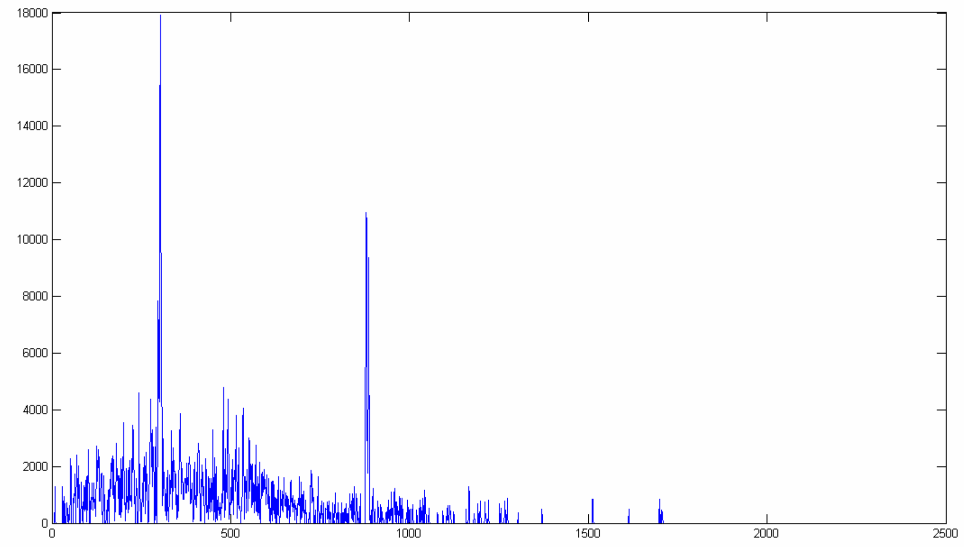

Fig.5.21 Ship number detection in the Radon domain.

FOCUSING AND VELOCITY ESTIMATION

Every ship is analyzed separately; as shown in Fig.5.22 and 5.23, the ship appear as complex objects, and the ships are as two separated targets.

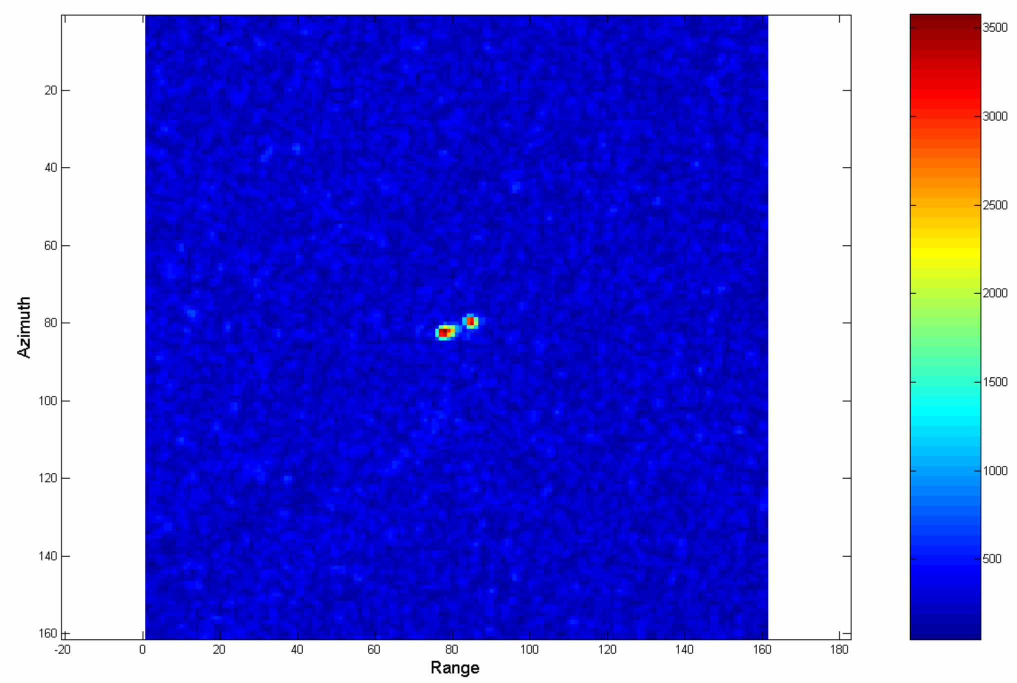

Fig.5.22 First ship found.

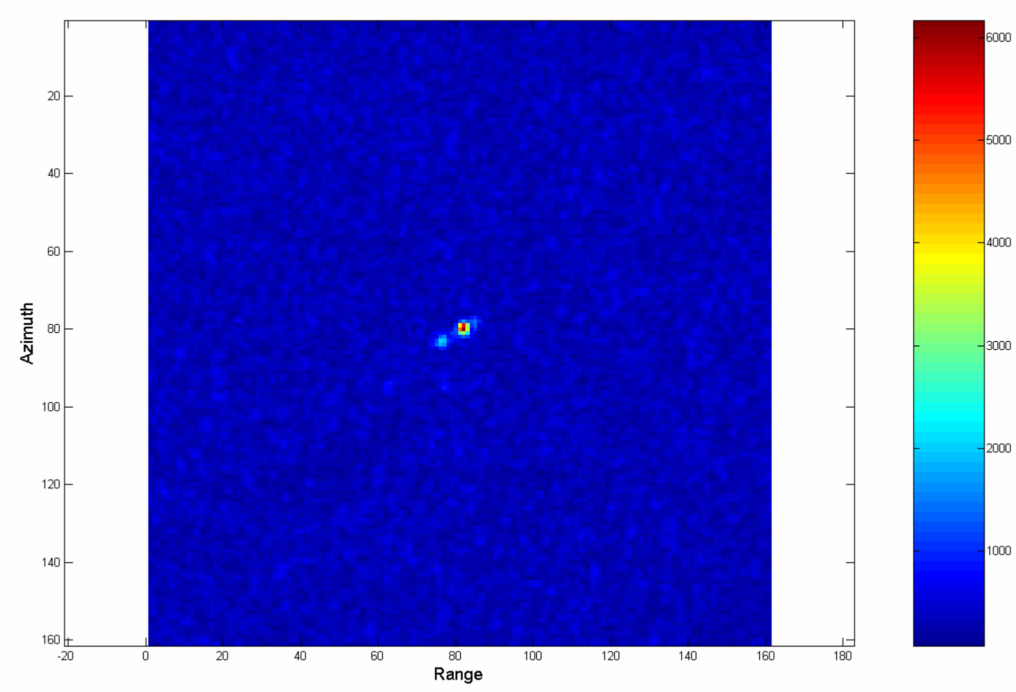

Fig.5.23 Second ship found.

The results of the estimation algorithm are shown in Tab.5.7 and 5.8.

Tab.5.5

Results with the first method

Ship number	Length (m)	Real v_{rg} (m/s)	Real v_{az} (m/s)	Estimated v_{rg} (m/s)	Estimated v_{az} (m/s)	Error v_{rg} (%)	Error v_{az} (%)
1	163	6.7	-3.8	22.8	-3.6	239.1	-5.8
2	188	4.1	-2.7	-21.9	-12.1	-625.7	345.3

Tab.5.6

Results with the second method

Ship number	Length (m)	Real v_{rg} (m/s)	Real v_{az} (m/s)	Estimated v_{rg} (m/s)	Estimated v_{az} (m/s)	Error v_{rg} (%)	Error v_{az} (%)
1	163	6.7	-3.8	9.9	-3.4	47.8	-10.8
2	188	4.1	-2.7	3.8	-2.2	-7.1	-19.6

Note that the wake to sea ratio is very low for the two ships, the ships have a complex form and the velocity is not too high; for these motivations the velocity estimation results difficulty for the algorithm, because the Radon transform can’t identify well the wake as linear structure. In fact, the first method fails in the estimation for the two ships. The second method results more robust: For the first ship the conditions are very difficulty to estimate the velocity, as shown in Tab. 5.8; however in the second method the estimation has a reasonable error.

APPENDIX – NUMERICAL RESULTS OF SIMULATION

The numerical results of the simulations of the first method (Tab.) and second method (Tab.) are shown.

As shown in Tab.5.7, with a wake to sea ratio less than -2 dB the method fails.

Tab.5.7

Simulation results with the first method

WSR (dB)	Variance	θ (°)	v_{rg} (m/s)	v_{az} (m/s)	Error v_{rg} (%)	Error v_{az} (%)
-5	1000	135	-6.1	-6.1	5.0	5.0
-5	2000	135	-6.1	-6.1	5.0	5.0
-5	3000	133	-6.4	-6.9	10.0	18.0
-5	4000	135	-6.1	-6.1	5.0	5.0
-5	5000	138	-5.8	-5.3	0.0	-10.0
-5	6000	133	-6.4	-6.9	10.0	18.0
-5	7000	132	-6.4	-7.1	10.0	22.2
-5	8000	132	-6.4	-7.1	10.0	22.2
-5	9000	132	-6.4	-7.1	10.0	22.2
-5	10000	137	-6.1	-5.7	5.0	-2.1
-4	1000	135	-6.1	-6.1	5.0	5.0
-4	2000	134	-6.4	-6.7	10.0	13.9
-4	3000	133	-6.4	-6.9	10.0	18.0
-4	4000	135	-6.1	-6.1	5.0	5.0
-4	5000	129	-6.4	-7.9	10.0	35.8
-4	6000	133	-6.4	-6.9	10.0	18.0
-4	7000	133	-6.4	-6.9	10.0	18.0
-4	8000	137	-6.1	-5.7	5.0	-2.1
-4	9000	137	-6.1	-5.7	5.0	-2.1
-4	10000	133	-6.4	-6.9	10.0	18.0
-3	1000	137	-6.1	-5.7	5.0	-2.1
-3	2000	133	-6.4	-6.9	10.0	18.0
-3	3000	130	-6.4	-7.7	10.0	31.1
-3	4000	135	-6.1	-6.1	5.0	5.0
-3	5000	134	-5.8	-6.0	0.0	3.6
-3	6000	134	-6.4	-6.7	10.0	13.9
-3	7000	138	-5.5	-5.0	-5.0	-14.5
-3	8000	135	-6.1	-6.1	5.0	5.0
-3	9000	138	-5.5	-5.0	-5.0	-14.5
-3	10000	137	-6.1	-5.7	5.0	-2.1
-2	1000	134	-6.4	-6.7	10.0	13.9
-2	2000	132	-6.4	-7.1	10.0	22.2
-2	3000	30	4.7	-2.7	-180.0	-53.8
-2	4000	36	2.9	-2.1	-150.0	-63.7
-2	5000	140	-5.8	-4.9	0.0	-16.1
-2	6000	45	3.8	-3.8	-165.0	-35.0
-2	7000	130	-6.7	-8.0	15.0	37.1
-2	8000	36	2.6	-1.9	-145.0	-67.3
-2	9000	139	-5.8	-5.1	0.0	-13.1
-2	10000	122	-8.2	-13.1	40.0	124.0
-1	1000	104	-13.1	-52.7	125.0	802.4
-1	2000	139	-5.8	-5.1	0.0	-13.1
-1	3000	76	12.0	-48.0	-305.0	722.2
-1	4000	179	-7.6	-0.1	30.0	-97.7
-1	5000	160	-5.8	-2.1	0.0	-63.6
-1	6000	24	2.3	-1.0	-140.0	-82.2
-1	7000	155	-5.5	-2.6	-5.0	-55.7
-1	8000	147	-5.0	-3.2	-15.0	-44.8
-1	9000	15	4.1	-1.1	-170.0	-81.2
-1	10000	110	-12.9	-35.3	120.0	504.4

The second method is more robust, as shown in Tab. 5.8: only with wake to sea ratio of -1dB and with an important speckle the method fails.

Tab.5.8

Simulation results with the second method

WSR (dB)	Variance	θ (°)	v_{rg} (m/s)	v_{az} (m/s)	Error v_{rg} (%)	Error v_{az} (%)
-5	1000	135	-6.1	-6.1	5.0	5.0
-5	2000	135	-6.1	-6.1	5.0	5.0
-5	3000	135	-6.1	-6.1	5.0	5.0
-5	4000	135	-6.1	-6.1	5.0	5.0
-5	5000	135	-6.1	-6.1	5.0	5.0
-5	6000	135	-6.1	-6.1	5.0	5.0
-5	7000	135	-6.1	-6.1	5.0	5.0
-5	8000	135	-6.1	-6.1	5.0	5.0
-5	9000	135	-5.8	-5.8	0.0	0.0
-5	10000	135	-6.1	-6.1	5.0	5.0
-4	1000	135	-6.1	-6.1	5.0	5.0
-4	2000	135	-6.1	-6.1	5.0	5.0
-4	3000	135	-6.1	-6.1	5.0	5.0
-4	4000	135	-6.1	-6.1	5.0	5.0
-4	5000	135	-6.1	-6.1	5.0	5.0
-4	6000	135	-6.1	-6.1	5.0	5.0
-4	7000	135	-6.1	-6.1	5.0	5.0
-4	8000	135	-6.1	-6.1	5.0	5.0
-4	9000	135	-6.1	-6.1	5.0	5.0
-4	10000	135	-6.1	-6.1	5.0	5.0
-3	1000	135	-6.1	-6.1	5.0	5.0
-3	2000	135	-6.1	-6.1	5.0	5.0
-3	3000	135	-5.8	-5.8	0.0	0.0
-3	4000	135	-6.1	-6.1	5.0	5.0
-3	5000	135	-5.8	-5.8	0.0	0.0
-3	6000	135	-6.1	-6.1	5.0	5.0
-3	7000	135	-5.8	-5.8	0.0	0.0
-3	8000	135	-6.1	-6.1	5.0	5.0
-3	9000	135	-5.8	-5.8	0.0	0.0
-3	10000	135	-6.1	-6.1	5.0	5.0
-2	1000	135	-6.1	-6.1	5.0	5.0
-2	2000	135	-6.1	-6.1	5.0	5.0
-2	3000	135	-6.1	-6.1	5.0	5.0
-2	4000	135	-5.8	-5.8	0.0	0.0
-2	5000	135	-6.1	-6.1	5.0	5.0
-2	6000	135	-6.1	-6.1	5.0	5.0
-2	7000	135	-6.1	-6.1	5.0	5.0
-2	8000	135	-6.1	-6.1	5.0	5.0
-2	9000	135	-6.1	-6.1	5.0	5.0
-2	10000	135	-6.7	-6.7	15.0	15.0
-1	1000	135	-5.8	-5.8	0.0	0.0
-1	2000	135	-6.1	-6.1	5.0	5.0
-1	3000	135	-4.1	-4.1	-30.0	-30.0
-1	4000	135	-7.0	-7.0	20.0	20.0
-1	5000	135	-0.9	-0.9	-85.0	-85.0
-1	6000	135	-6.1	-6.1	5.0	5.0
-1	7000	135	-6.1	-6.1	5.0	5.0
-1	8000	135	-3.2	-3.2	-45.0	-45.0
-1	9000	315	5.8	5.8	-200.0	-200.0
-1	10000	135	-2.3	-2.3	-60.0	-60.0

REFERENCES

[1] P.Lombardo, M.Sciotti, “Segmentation-based technique for ship detection in SAR images”, Proceedings of the IEE Radar, Sonar and Navigation, Vol. 148, Issue 3, pp. 147-159, June 2001.

[2] K. Ouchi, “On the Multilook Images of Moving Targets by Synthetic Aperture Radars”, IEEE Transactions on Antennas and Propagation, Vol. AP-33, N. 8, Pag. 823-827 August 1985.

[3] K.Ouchi, S.Tamaky, H.Yaguchi, M.Lehara, “Ship detection based on coherence images derived from cross correlation of multilook SAR images”, IEEE Geoscience and Remote Sensing Letters, Vol. 1, Issue 3, Pag. 184–187, July 2004.

[4] M.Iehara, K.Ouchi, I.Takami, K.Morimura, S.Kumano, “Detection of ships using cross-correlation of split-look SAR images”, Proceedings of the IEEE Int. Geoscience Remote Sensing Symposium, IGARSS, Pag. 1807-1809, 9-13 July 2001.

[5] A.Arnaud, “Ship Detection by SAR Interferometry”, Proceedings of the IEEE Int. Geoscience Remote Sensing Symposium, IGARSS, Vol.5, Pag.2616-2618, 28 June-2 July 1999.

[6] J.K.E. Tunaley, “The estimation of ship velocity from SAR imagery”, Proceedings of the IEEE Int. Geoscience Remote Sensing Symposium, IGARSS, Vol.1, Pag. 191-193, 21-25 July 2003.

[7] G.Zilman, A.Zapolski, M.Maron, “The Speed and Beam of a Ship From Its Wake’s SAR Images”, IEEE Transactions on Geoscience and Remote Sensing, Vol. 42 , n. 10, Pag. 2335–2343, October 2004.

[8] M.Cusano, J.Lichtenegger, P.Lombardo, A.Petrocchi, D.Zanovello, “A real time operational scheme for ship traffic monitoring using quick look ERS SAR images”, Proceedings of the IEEE Int. Geoscience Remote Sensing Symposium, IGARSS, Vol.7, Pag.2918-2920, 24-28 July 2000.

[9] G.Du, T.S.Yeo, “A novel Radon transform-based method for ship wake detection”, Proceedings of the IEEE Int. Geoscience Remote Sensing Symposium, IGARSS, Pag. 1032-1034, 20-24 September 2004.

[10] http://earth.esa.int/workshops/ers97/papers/lini/, Workshop ESA 1997.

[11] P.W. Vachon, M.Dragosevic, “Adaptive Processing of RADARSAT-1 Fine Mode Data: Ship Parameter Estimation”, Technical memorandum, March 2007.

[12] F.Meyer, S.Hinz, R.Muller, G.Palumbinkas, C.Laux, H.Runge, “Towards Traffic Monitoring with TerraSAR-X”, Research Paper, 2007.

[13] P. Toft, “The Radon Transform: Theory and implementation”, Ph.D Thesis, Department of Mathematical Modelling Section for Digital Signal Processing Technical University of Denmark, 1996.

[14] A.Radius, P.A.C.Marques, “A Novel Methodology for Full Velocity Vector Estimation of Ships Using SAR Data”, Proceedings of the 7th European Conference on Synthetic Aperture Radar, EUSAR’04 (accepted), 2-5 June 2008.

[15] C.J. Oliver, “Representation of radar sea clutter”, Proceedings of the IEE Radar and Signal Processing, Vol. 135, Issue 6, pp. 497-500, December 1988.

[16] F.T.Ullaby, M.C.Dobson, “Handbook of Radar Scattering Statistics for Terrain”, Artech House 1989.

CHAPTER 6
CONCLUSIONS

The capability of SAR to analyze the dynamic characteristics of the observed objects on the Earth surface makes the SAR particularly fit for moving target detection in commercial, surveillance and strategic context. For strategic context the major interest of this activity field is from the military point of view. From the commercial and surveillance contexts, the extensive use of the SAR for road and ship traffic monitoring is an optimal solution due to the global monitoring capability with high resolution and for the sensitivity to the target velocity. The major problem is to extract the informative content in very complex scenarios, where the useful signal of the moving targets is always contaminated with noise.

A lot of moving target processing techniques were recently proposed. Some techniques are fit to specific contexts, and the ideal solution is the convergence toward a general form, which allows to produce good results in different environment and with different data types.

This thesis addresses this problem, proposing some interesting novel elements in the scientific panorama.

The main goal of this thesis was to propose novel techniques in the moving target processing, using SAR raw data. To introduce the argument, the thesis is organized as shown in the following.

Chapter 1 introduced the basic principle of the SAR processing, with attention to the problem of the moving target effects. Chapter 2 explained the working of the SAR raw data simulation, developed to generate synthetic data with the aim to validate the developed algorithm. Chapter 3 introduced the first proposed algorithm, which processes two-channel raw data to generate information about the velocity vector of the moving targets. The algorithm gave good results only in favourable scenarios with low SCR, while in more real context the error is higher; the motivation of this result is for the choice of the SAR system. We selected the parameters of the ERS sensor, for the major availability of the data, starting from a disadvantageous situation; in fact, the MTI applications require high resolution and high SCR, while the performance of ERS is not fit for this aim.

Chapter 4 proposed the effort to adapt the precedent algorithm to single channel raw data, presenting a deep analysis of a sub-aperture processing algorithm. Note that the choice of the ERS parameters to validate the algorithm was due to adapt the two-channel algorithm to a single channel, because of the difficulty to find multi-channel raw data. Chapter 5 analyzed the second developed algorithm, which derives the motion parameters of the ships from processed data, using only the amplitude information.

The algorithm produced very encouraging results, estimating the velocity vector with a reasonable error in very strong conditions and using the minimal informative content of the SAR data.

Bellow we summarize the main introduced contributions and the suggestions for future research directions.

6.1 CONTRIBUTIONS

In this thesis, the contributions are essentially four.

Firstly, we implemented a SAR raw data simulator, which produces synthetic raw data of a stationary scene with moving targets; the simulator is the necessary instrument to validate the algorithms.

As shown, chapter 3 introduced the developed algorithm to derive the motion parameters from two channel raw data. The strong novelties of the technique are that it works without *a-priori* information, and it takes into account the coupling of range and azimuth velocity, proposing an iterative method to retrieve the velocity components.

This is very important, because some algorithms working with SAR processing techniques based on the matched filter de-couple the velocity components, simplifying the procedure but introducing additional errors.

Chapter 4 introduces another important argument. Trying to extend the usability of the algorithm for a single-antenna SAR with a split-aperture processing algorithm, we demonstrate the information type which can be derived from sub-apertures of a single channel.

The second proposed technique analyzed in chapter 5 presents a very strong motivation, which makes the applicability of the algorithm very interesting. It uses the minimal informative content of SAR data, processing only amplitude data, which is more easily available. The algorithm is an optimal instrument to extract the moving target map of a sea-scene, resulting in a very light algorithm from the computational point of view

6.2 FUTURE RESEARCH DIRECTIONS

Taking into account the real context in which the algorithms can be applied, we propose the following strategy for the future research.

For the first proposed algorithm, the used SAR processor is not suitable to process a big quantity of data; it is desirable the adaptation to a more efficient algorithm, from a computational point of view, as Range-Doppler algorithm or ω-k algorithm. Moreover, to make more robust and accurate the technique it is necessary to improve the selection criterion for the estimation of the azimuth velocity, using not only the amplitude information but also the phase.

For the second algorithm, the pre-processing phase must be improved, due to the difficulty to work in a complex and incoherent environment as the sea. This may be achieved by using an alternative filtering mode such as the wavelet transform. The expected result is to realize a technique very robust and accurate, which may be used easily without the necessity of big resources, due to the lightness of the program.